LBNL-45467

Baryon Stopping and Hadronic Spectra in Pb – Pb Collisions at 158 GeV/nucleon

Glenn Elliot Cooper
Ph.D. Dissertation

Department of Physics
University of California, Berkeley

and

Nuclear Science Division
Lawrence Berkeley National Laboratory
University of California
Berkeley, CA 94720

April 2000

This work was supported by the Director, Office of Science, Office of High Energy and Nuclear Physics, Division of Nuclear Physics, of the US Department of Energy under Contract No. DE-AC03-76SF00098.

Abstract

Baryon Stopping and Hadronic Spectra in Pb – Pb Collisions at 158 GeV/nucleon

by

Glenn Elliot Cooper
Ph.D. Dissertation

Physics Department
University of California, Berkeley

and

Nuclear Science Division
Lawrence Berkeley National Laboratory
University of California
Berkeley, CA 94720

April 2000

Baryon stopping and particle production in Pb + Pb collisions at 158 GeV/nucleon are studied as a function of the collision centrality using new proton, $\overline{\mathrm{p}}$, $\mathrm{K}^{\pm}$ and $\pi^{\pm}$ production data measured with the NA49 experiment at the CERN Super Proton Synchrotron (SPS). Stopping, which is measured by the shift in rapidity of net protons or baryons from the initial beam rapidity, increases in more central collisions. This is expected from a geometrical picture of these collisions. The stopping data are quantitatively compared to models incorporating various mechanisms for stopping. In general, microscopic transport calculations which incorporate current theoretical models of baryon stopping or use phenomenological extrapolations from simpler systems overestimate the dependence of stopping on centrality. Approximately, the yield of produced pions scales with the number of nucleons participating in the collision. A small increase in yield beyond this scaling, accompanied by a small suppression in the yield of the fastest pions, reflects the variation in stopping with centrality. Consistent with the observations from central collisions of light and heavy nuclei at the SPS, the transverse momentum distributions of all particles are observed to become harder with increasing centrality. This effect is most pronounced for the heaviest particles. This hardening is discussed in terms of multiple scattering of the incident nucleons of one colliding nucleus as they traverse the other nucleus and in terms of rescattering within the system of produced particles.

Contents

List of Figures

List of Tables

Acknowledgements

The work documented in this dissertation is the result of the efforts of many people. I would like to thank all of my collaborators for their hard work and for allowing me the privilege of working with them. I especially thank my advisors, Peter Jacobs and Herb Steiner for their advice, prodding, patience, and scientific input. I also thank Milton Toy, whose own Ph.D. studies formed the foundation for most of my dissertation research. I thank the Relativistic Nuclear Collisions group at the Lawrence Berkeley National Laboratory for providing financial support and a stimulating environment for scientific research. In remembering my years with RNC, I will particularly value the many friendships developed along the way. I also thank Peter, Herb, and Art Poskanzer for their careful reading of the drafts of my dissertation.

I would also like to thank my parents, Carol and Gerry Cooper, as well as my brother and sisters, for nurturing and encouraging my interest in science and physics and for being good friends. Finally, and most importantly, I would like to thank my partner, Margaret Hawley, who shared in the griefs and joys I encountered during graduate school, helped me overcome my many doubts, encouraged my education and growth in every way, and continues to be my best friend.

Chapter 1

Introduction

1.1 Overview

The mechanism by which relativistic nucleons are decelerated in nuclear matter, generally called stopping, is not well understood. The stopping process depends on the structure of nucleons and their interactions with other nucleons in nuclear matter, which are governed by quantum chromodynamics (QCD). However, the bulk of the relevant interactions occur at small momentum transfer, where rigorous application of QCD is not possible using available theoretical tools.

Nuclear stopping plays an important role in the study of relativistic nuclear collisions, which aims to measure the properties of matter at extreme temperature and pressure. A central goal of the relativistic heavy-ion program is the creation of a phase of matter consisting of deconfined quarks and gluons, commonly called Quark-Gluon Plasma (QGP). Colliding relativistic heavy nuclei is believed to be the best way to produce and study QGP in the laboratory. As a result of such a collision, matter and energy carried initially by the projectiles is transported via the stopping process toward the center of mass. Whether this creates a volume with an energy and baryon density sufficiently high for the creation of QGP depends on the initial beam energy, projectile size, and degree of stopping.

There are extensive data on stopping from proton-proton (p + p), proton-nucleus (p + A), and nucleus-nucleus (A + A) collisions over a wide range of relativistic energies (for reviews see [BL88] and [VH95]). Empirical models, based on ideas from the theory of collisions and QCD, have been used to describe the data with moderate success. However, remaining uncertainties have necessitated measuring the details of the stopping process at each new energy scale and colliding system available to physicists. Recent developments in applying QCD based models of baryons to the question of stopping have resulted in better descriptions of stopping data. Further systematic data available now and in the near future will assist in understanding the structure and interactions of baryons.

As a nucleon is stopped, it becomes excited, slows down, and fragments into new particles. This is a stochastic process which can be characterized by how the conserved quantities energy, charge, and baryon number are redistributed, and how this relates to particle production. For simple systems involving few nucleons, these quantities can be correlated event-by-event. This is a powerful tool for constraining the stopping dynamics. For collisions between nuclei, many nucleons participate and forming such correlations is not possible. Instead, stopping is characterized by semi-inclusive distributions[1] of the conserved quantities, which vary with the collision system and energy, and by how it is reflected in the multiplicity and distributions of produced particles.

[1] Throughout this thesis, distributions will be discussed in terms of the longitudinal variables rapidity (y) and $x_{\rm F}$, and the transverse variables $p_\perp$ and $m_\perp$. These variables and the distinction between exclusive, inclusive, and semi-inclusive distributions are defined in Appendix B.

In A + A collisions, the nature of the produced system depends strongly on the geometry of the collision. A grazing collision between two nuclei at large impact parameter can involve few nucleons and appears similar to interactions between single nucleons. Head-on collisions at zero impact parameter are much more violent, as many nucleons of one nucleus must traverse nearly the full thickness of the other nucleus and suffer increased stopping, which produces a more excited system. As a function of impact parameter, the degree of stopping and the size and excitation of the produced system vary continuously. This can be used to search for the onset of new phenomena within a single sample of collisions.

In this thesis, new results on baryon stopping and hadron production from fixed target Pb+Pb collisions at a beam energy of 158 GeV/nucleon are presented. Specifically, the semi-inclusive spectra of proton, $\overline{\mathrm{p}}$, K^+, K^-, π^+, and π^- produced in collisions will be obtained over a large fraction of the available phase space and as a function of collision centrality and used to study how baryon number and energy are redistributed as a result of the collisions. The measurements were made using the NA49 apparatus, a heavy ion experiment at the CERN Super Proton Synchrotron (SPS) designed to measure charged and strange hadronic particle production over a large portion of phase space. Results from central Pb + Pb collisions have been published in [Ap+99] and [Toy99]. Here, these results are extended to collisions over nearly the full range of collision impact parameter.

The remainder of this chapter discusses the physics issues raised above in some more detail and concludes with an outline and a statement of the objectives of this thesis.

1.2 QCD and the Search for Quark-Gluon Plasma

QCD describes strongly interacting matter in terms of interactions between quarks mediated by the exchange of gluons. It is a non-Abelian gauge theory in which both the matter particles and gauge fields carry color charge. It exhibits several remarkable features. First, the effective coupling strength decreases logarithmically with momentum transfer (or with decreasing distance). At high momentum transfer, quarks appear as nearly free particles (asymptotic freedom). It was because of the asymptotic freedom of non-Abelian gauge theories [tH72, GW73, Pol73], and the experimental evidence from deep inelastic scattering that nucleons are composed of point-like fermions that behaved as nearly free particles [FK72], that QCD was adopted as the theory of strong interactions. Second, at large distances or small momentum transfer, the coupling becomes strong enough to confine color charges within composite, color-singlet hadrons. Free, isolated quarks or gluons have not been observed. An excited hadron does not emit single quarks but instead radiates additional hadrons. Finally, although the theory of QCD exhibits a global chiral flavor symmetry which is only slightly broken by the small quark masses, this symmetry is not reflected in the spectrum of strongly interacting particles. In fact, this symmetry is spontaneously broken and it is the physical vacuum which is not invariant under this symmetry (see [CL84]).

Except in the domain of large momentum transfer where the coupling is weak and perturbative calculations may be employed, understanding and using QCD as a predictive theory has proved extremely difficult. Nonetheless, universal arguments have been used to make qualitative predictions about the phase structure of strongly interacting matter. Because of confinement, the low temperature and low baryon density phase of QCD is appropriately described in terms of interactions among hadrons and the chiral vacuum. On the other hand, at high temperature or baryon density, hadrons must overlap significantly, and because of asymptotic freedom, quarks and gluons become the more appropriate degrees of freedom. Also at high temperature or density the chiral vacuum is evaporated and chiral symmetry is restored. At intermediate temperature and baryon density, a transition between these phases must occur. Determining the number and structure of the quark-gluon phases as a function of temperature and baryon density and the nature of their transitions to the hadronic phase is an active field of theoretical study [Raj99].

Lattice QCD is a computational technique for carrying out non-perturbative QCD calculations. Recent results show that the chiral transition occurs in the temperature range of 140–170 MeV

at zero baryon density [Go+97]. The prediction for the order of this transition depends strongly on assumptions about the light quark masses, but it is now thought that this is not a phase transition but a smooth, rapid crossover. It is also thought that the transition to deconfined matter occurs coincidentally with the chiral transition, but it is not yet clear how to measure confinement in Lattice QCD [Hay99].

Matter is thought to have existed in the excited state of QGP in the early universe, up to a few microseconds after the Big Bang, before it had expanded and cooled enough for hadrons to form [Ree90]. This state may exist in the present universe at the center of dense stars, where gravitational pressure can compress the core to sufficient density, and may cause observable effects in the frequency spectrum of pulsars [GPW97].

An extensive experimental program has been undertaken at several accelerator facilities, with the goal of observing QGP in the laboratory, studying its properties, and observing its transition back to hadronic matter. Because the lifetime of the high density phase created in such collisions is short and because the quarks and gluons become confined in color-neutral objects during the transition back to the hadronic phase, direct observation of the QGP degrees of freedom is not possible. Instead, indirect information must be inferred from the hadrons, leptons, and photons produced from the collision. Hadrons are copiously produced, but interact strongly with each other until well after the transition from QGP back to hadrons and this tends to obscure the information they carry about the system prior to the phase transition. On the other hand, leptons and photons interact weakly with the rest of the system and can better reflect the properties of the system at the time they were produced. But also because they interact weakly, directly produced leptons and photons are rare in comparison to hadrons, and the information they carry can be obscured by the large background of indirectly produced photons and leptons which comes from the decay of hadrons.

Many measurements have been proposed as signatures of the formation of the QGP [HM96, Ba+99]. Examples include enhanced strangeness production [RM82, RM86, Ody98] and suppression of J/ψ production [Ram98]. In general, one looks for differences in single-particle spectra or multi-particle correlations between collisions in which a QGP was formed and collisions in which no QGP was formed (commonly referred to as a *hadronic* scenario). Evaluating whether a transition occurred requires an accurate hadronic scenario as a basis for comparison. This basis is established using:

1. Collisions of lighter nuclei or nucleons.

2. Detailed simulations.

3. Variation of one or more control parameters within a single collision system.

Data to be presented in this work will address primarily item 3, by studying how baryon stopping and the production of charged hadrons vary with system size, where system size is selected using the collision centrality. This has the advantage providing information over a continuously varied parameter, all gathered under identical conditions with the same apparatus, so that experimental biases cancel to the maximum extent.

1.3 Nucleon and Nuclear Collisions

In a laboratory experiment, the colliding system center-of-mass energy and system size may be controlled. System size is determined by the nuclear species and by the configuration of the collision. The configuration of a collision is shown schematically in Figure 1.1. A projectile (A) collides with a target (B) with their centers separated by the impact parameter b. For a relativistic nuclear projectile, only a fraction of its nucleons, given approximately by the geometrical overlap region between the projectile and target, participate in the collision. The non-participating, or spectator, nucleons continue with their original momenta largely unaffected by the collision. While

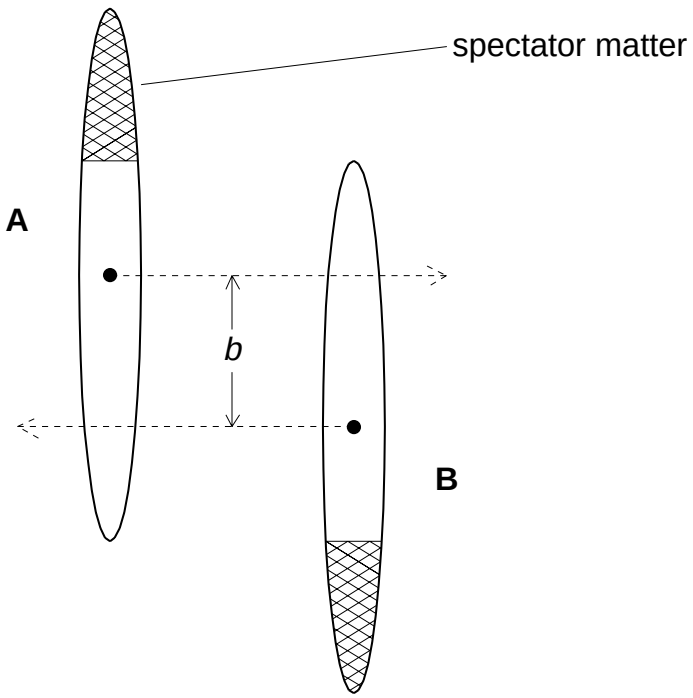

Figure 1.1: Geometrical picture of a relativistic nuclear collision at impact parameter b, as viewed in the center of mass. The nuclei are compressed to discs by Lorentz contraction. Spectator matter, indicated by the hatches, continues forward with its momentum largely unaffected by the collision.

it is not possible to measure the impact parameter directly, related measurements, in particular the energy carried by the spectator nucleons, the produced transverse energy, and the produced particle multiplicity, are found to be well correlated and good indicators of centrality and are used to segregate collisions into samples with different impact parameter ranges.

It is instructive to begin discussion of stopping and particle production in A + A collisions by reviewing the phenomenology of p+p collisions at high energy. These collisions are characterized by leading baryons carrying the conserved baryon number of the target and projectile, and a few produced particles, which are mostly pions and which carry the difference in energy between the incoming protons and the leading baryons. The leading baryons are not necessarily protons, since the collision may have been charge or flavor changing, and may not be the particles with the highest center-of-mass momenta, as a fast pion might be emitted which carries a significant fraction of the momentum of one of the original protons. Also, while additional baryons may be produced in pairs with anti-baryons, it is the fastest baryon that is conventionally associated with the original protons. From this description, one observes that there is only a loose connection between the stopping of baryon number, energy, and charge.

Inclusive *net* distributions, meaning the difference between particle and anti-particle distributions, are used to study stopping. Particle/anti-particle pair production does not contribute to such a distribution. In this work, charged hadron distributions will be measured and used to obtain net proton ($\mathrm{p}-\overline{\mathrm{p}}$) momentum distributions. The $\mathrm{p}-\overline{\mathrm{p}}$ distributions will be extrapolated to net baryon ($\mathrm{B}-\overline{\mathrm{B}}$) distributions using available data and models. A complication with the use of these distributions arises because the measured momenta are those resulting at particle freeze-out, which is when particles cease to interact. In the scenario where significant rescattering among pro-

duced particles occurs, the momentum distributions resulting from the initial stopping can become smeared. However, because the magnitude of the momentum transfer involved in rescattering is small in comparison to the longitudinal momentum scale, rescattering, especially of heavy particles such as protons, has only a small effect on distributions in longitudinal variables such as y. As a result, these distributions can be used reliably to study stopping.

The data from p + p collisions show that the leading proton rapidity distribution falls off from beam rapidity as $e^{\Delta y}$ ($\Delta y = y - y_{beam} < 0$) [AB$^+$91, Ba$^+$91]. More limited data on leading neutron and strange baryons show that the more a baryon is stopped, the larger is the probability that its flavor will be changed [En$^+$75, GH91]. The transverse momentum of particles produced in the collision increases with increasing particle mass and depends weakly on the collision energy [Al$^+$87]. In addition, both the mean transverse momentum and multiplicity of produced particles has been seen to increase in those collisions in which the leading baryon is found to have suffered greater stopping.

In p+A and A+A collisions, a projectile nucleon may interact with several target nucleons, which can result in increased stopping. Indeed, data from p + A collisions for a variety of nuclear targets show that the leading baryon associated with the proton projectile suffers increased rapidity loss relative to p + p collisions, with the median rapidity loss increasing with increasing target A [To$^+$87]. These same data also show that stopping increases at a given target A as the centrality or nuclear thickness traversed by the proton increases.[2] The multiplicity of produced particles in p+A collisions increases strongly with A or centrality, but the bulk of this enhancement occurs in the nuclear target hemisphere and is a reflection of "wounded nucleon" scaling, which refers to the linear dependence of the multiplicity with the number of nucleons participating in the collision [BC74]. In the central rapidity region, the increase in multiplicity with the number of collisions is weaker and seems to saturate at about 3–4 collisions, while the multiplicity in the proton beam fragmentation region is nearly constant [BL88]. In addition, the mean transverse momenta of produced particles increases with increasing nuclear target size or collision centrality.

In A + A collisions at a given impact parameter, the incident nucleons traverse a variety of nuclear thicknesses and therefore suffer differing degrees of stopping. The net baryon distribution is a result of an average over these collision geometries. For symmetric collisions, two extreme possibilities are shown in Figure 1.2. In the case of transparency, the baryons are only shifted a small fraction of the projectile-target rapidity gap, as might be the expectation for light system like p + p or at very high energy. In the case of full stopping, the nuclei are effectively opaque to each other and the baryons pile up at mid-rapidity. As shown in Figure 1.3, central collisions between both light and heavy nuclei at the SPS display significant transparency, with somewhat greater stopping in Pb + Pb compared to S + S.

In spite of the increased stopping, central Pb + Pb and S + S collisions show essentially no difference in the shape of the rapidity distribution of produced particles. On the other hand, there is a slight increase in the yield per pair of participating nucleons in Pb + Pb (negatively charged hadron yields are 3.6 ± 0.2 for S+S and 4.0 ± 0.2 Pb+Pb, where the S+S results have been corrected for the isospin and slight energy differences for comparison to the Pb + Pb results) [Ap$^+$99, Toy99]. This small increase may be a reflection of the correlation observed in p+p collisions of the produced multiplicity with proton stopping or may result from increased rescattering among the produced particles in the larger system.

Data from both the SPS and lower energies show that the $p_\perp$ spectra of hadrons from nuclear collisions become harder with increasing hadron mass, and that this effect becomes stronger with increasing size of the colliding nuclei. As discussed in the next section, this is thought to result

[2] Centrality is estimated in a p + A collision by recording the number of nucleons recoiling from the target nucleus, which is correlated with the number of nucleons in the target which interact with the incident proton. The strength of this correlation depends theoretically on the model of secondary collisions in the nucleus and experimentally on the ability to identify recoil nucleons (usually done simply by momentum cuts). Evidence for the correlation originally came from a comparison of the yield and distribution of particles produced with nuclear targets of differing A but at a fixed number of recoil nucleons. For further discussion, see, for example, [BL88].

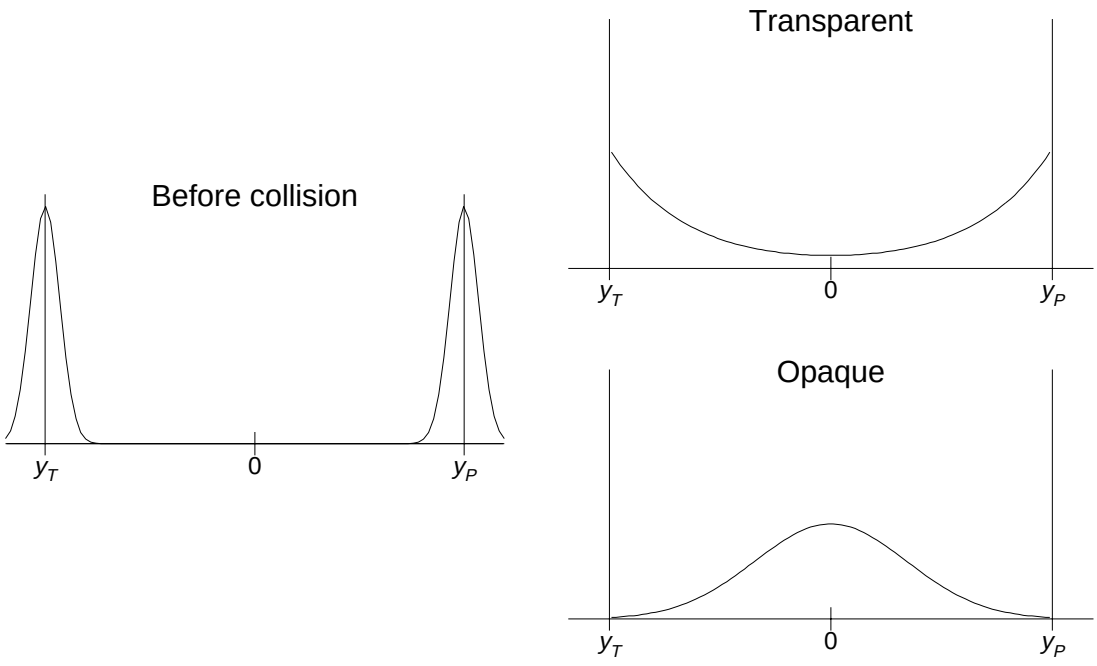

Figure 1.2: Two extreme scenarios of baryon stopping. Rapidity distributions of the net baryon number are shown before (left) and after a collision. The transparent case (above right) is similar to what is observed in p + p collisions. In the opaque case (below right), baryons are piled up around mid-rapidity.

from the buildup of a collective flow velocity due to interactions among the produced particles. It may also be due in part to the generation of $p_\perp$ by the multiple collisions that the incoming baryons suffer in the stopping process.

1.4 Models of Stopping, Particle Production and A + A Collisions

Motivated by the leading baryon effect from p + p collisions, most models of nucleon interactions at SPS energies and above treat the nucleon as a quark-diquark pair, where the diquark acts as a single entity and typically fragments directly into the leading baryon. Since the diquark carries a large fraction of the initial proton momentum, the produced baryon will also. This picture qualitatively describes the net proton distributions from p + p collisions. However, based on a study of the energy dependence of the mid-rapidity net proton yield in p + p collisions, it was shown that an additional component (or components) beyond diquark fragmentation must be present, resulting in enhanced baryon stopping, albeit with small relative probability [KZ89].

The mechanism by which this component acts is not clear. Diquark breaking [KZ89], in which only one of the two quarks from the diquark ends up in the leading baryon, is one possibility. This enhances the net baryon yield at large rapidity shift from the projectile. An alternative picture was proposed in [Kha96], in which the gauge-invariant gluon structure of baryons [RV77] can act dynamically in collisions and transport baryon number over large rapidity intervals, independent

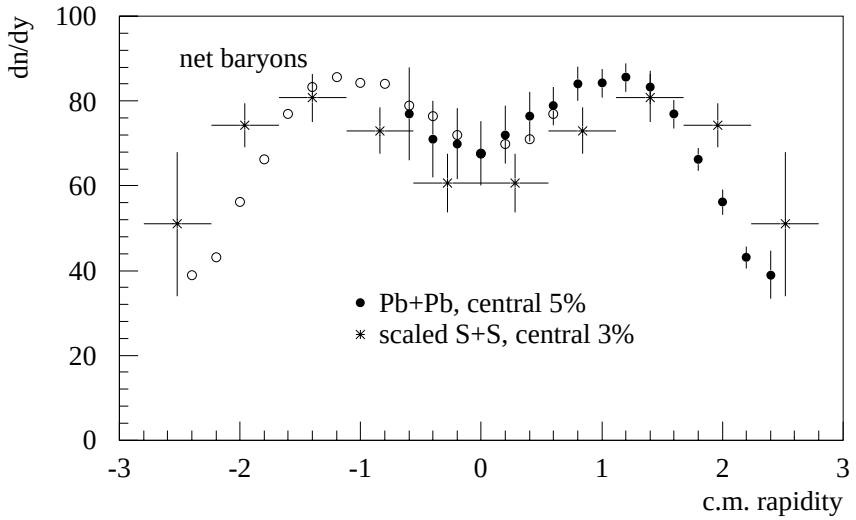

Figure 1.3: Net baryon rapidity distributions from central S + S and Pb + Pb collisions at the CERN SPS. The S + S data are scaled to match the number of participant nucleons from Pb + Pb. Because the collisions systems are symmetric, the measured data points can be reflected about $y = 0$. For S + S, the data points with $y < 0$ are measured. For Pb + Pb, the filled circles are measured [Ap+99, Toy99].

of the baryon's valence quarks. Arguments based on this "gluon junction" picture or the diquark-breaking picture lead to differences in the energy dependence of baryon stopping, the probability for flavor change of a stopped baryon, and the produced multiplicity associated with stopping.

A number of microscopic transport codes exist which model A + A collisions. Typically, these models invoke the quark-diquark model of nucleon interactions and may (see VENUS [Wer93] and RQMD [Sor95]) or may not (see DPM [Ca+94] and HIJING [WG91]) include mechanisms beyond diquark fragmentation. It was noted in [GPV97] that components beyond simple diquark fragmentation are important for describing the baryon stopping results from A + A collisions. Attempts to add mechanisms for enhanced stopping based on the above pictures to models which otherwise consider only diquark fragmentation have been reasonably successful (see [CK96] and [VG99]).

Particle production in the transport models is based on the phenomenological model of formation and breakup of relativistic strings, using standard parameterizations such as the Lund string dynamics model [AGP93]. The models incorporate various mechanisms for calculating interactions between produced particles. In this work, data will be compared to both RQMD and VENUS. In contrast to VENUS, which allows little scattering between produced particles, RQMD propagates produced particles along classical trajectories and allows them to re-interact. In addition, data will be compared to the HIJING and HIJING/B [Van99] models. HIJING/B incorporates the baryon junction model into the HIJING model which otherwise contains only standard diquark fragmentation dynamics.

Another class of models widely used to simulate A + A collisions is based on relativistic hydrodynamics [SSH93b]. For hydrodynamics to be valid, the system must evolve in local equilibrium. While such conditions certainly do not exist very early or very late in the collision, and it is also not clear that this requirement is ever met, it has been observed that these models are able to describe produced particle spectra well for both light and heavy systems, even out to rather large $p_\perp$. A common picture that emerges from hydrodynamic calculations and fits to data is that

after the initial collision, the dense matter expands strongly in both the longitudinal and transverse directions, developing a large collective velocity field before the produced particles stop interacting. A fit to NA49 data from central Pb+Pb collisions using a recent model of this type [He+96, CNH95] shows a system at freeze-out with a temperature of 120 ± 12MeV and a transverse flow velocity of $\beta = 0.55$ [Ap+98b].

While hydrodynamics is able to fit the transverse spectra systematics from A + A collisions successfully, it has been argued that this transverse motion may in fact be due principally to the random walk of the incident nucleons, which generates successive collisions with collision centers that have transverse motion relative to the initial nucleon direction [LNS97]. In [BM98], the mid-rapidity transverse momentum spectra of net charged hadrons ($h^+ - h^-$) from centrality selected Pb + Pb collisions [Cer98] have been used in an attempt to rule out this random walk picture. At some level, this effect should be present, however, and transverse spectra of identified particles as a function of rapidity and impact parameter can be used to further clarify this argument.

1.5 Thesis Objectives

In this thesis, I will present and discuss semi-inclusive spectra of protons, $\overline{\mathrm{p}}$, K^+, K^-, π^+, and π^- measured in Pb+Pb collisions at 158 GeV/nucleon. I will use these spectra to study baryon stopping, particle production, and transverse momentum generation as a function of the collision impact parameter or size of the colliding system. In particular, I will address:

- The increase of the rapidity shift of baryons toward the center of mass as a function of the size of the colliding system. The results will be compared to results obtained for nucleon-nucleon collisions. The results will also be compared to A + A collision models to assess whether the baryon stopping mechanisms in these models are reasonable.

- The dependence of the yield of π on the size of the colliding system. How this yield scales with the number of nucleons participating in the collision will be presented. The additional dependence on the increase in baryon stopping will be studied.

- The dependence of the mean $p_\perp$ and shape of transverse spectra of proton, K, and π on the system size. The success of the competing models of initial multiple scattering of the interacting nucleons and of hydrodynamic flow of the produced particles in describing these data will be assessed.

While the measured data do provide a good measure of the dependence of the K yield on the system size, a discussion of these results and the general topic of strangeness enhancement in A+A collisions is beyond the scope of this thesis.

The remainder of this thesis is organized as follows. The NA49 experiment and data collection are described in Chapter 2. The analysis procedures for obtaining particle spectra from raw data are described in Chapter 3. The results are presented and discussed in Chapter 4. Chapter 5 summarizes this work and discusses areas for further study. Several appendices are included which contain further details concerning the determination of event centrality, simulations of the detector response, and model calculations. A final appendix contains a tabulation and parameterization of the measured particle distributions.

Chapter 2

Experimental Apparatus and Data Collection

2.1 Overview and Design Considerations

The NA49 apparatus is used to study the hadronic final states produced by collisions of beam particles accelerated by the CERN SPS with a variety of fixed targets. Charged hadrons are detected over a large fraction of the available phase space, allowing study of the correlations and internal structure of the events. The design was driven primarily by the desire to study central Pb + Pb collisions, which produce a very high multiplicity of hadrons, but also by the need to characterize lower multiplicity events, such as non-central nucleus-nucleus events and proton-nucleus events. This chapter will describe the components of the NA49 apparatus, with special emphasis on those components used in the study of central and non-central Pb + Pb collisions.

The NA49 experiment, shown in Figure 2.1, is a magnetic spectrometer with momentum reconstruction and identification of charged particles over a large angular acceptance [Af+99]. It is centered on two super-conducting magnets and four large volume Time Projection Chambers (TPC's). The TPC's are the primary charged particle tracking and identification devices. Identification of charged particles is accomplished by measuring the specific ionization of each track in the TPC's. It is supplemented by time-of-flight (TOF) measurement in those momentum ranges where particle separation by specific ionization is not possible. Additional identification of neutral and charged strange particles is accomplished by reconstruction of the decay topologies. A complement of fast detectors for characterizing the beam and for determining gross features of the collision is used for both on-line triggering of the detectors and for off-line event selection. The detector readout and data recording system was designed to be able to record about 10^6 events per run period.

The high particle multiplicities which are generated in central heavy ion collisions lead to high track densities in the plane perpendicular to the beam. Except for a relatively few particles with low laboratory momentum, most particles produce tracks which tend to run closely parallel to other particle tracks. Reconstructing the momentum and identifying individual tracks in this situation requires sampling of the tracks in a three dimensional grid with small grid spacing. TPC's naturally provide such a high spatial sampling.

The fixed target kinematics of the experiment strongly focuses produced particles into a narrow cone surrounding the beam. Even with the high spatial sampling provided by TPC's, the charged particle tracks in this cone must be significantly separated to allow for reconstruction. This requires both a magnetic field with a large total bending power and sufficient particle flight distance. To reconstruct both lower momentum particles, which are quickly bent out of cone, and high momentum particles, which are only slightly deflected, a detector system covering a long total baseline along the beam direction is required. A single TPC of this total length was not practical.

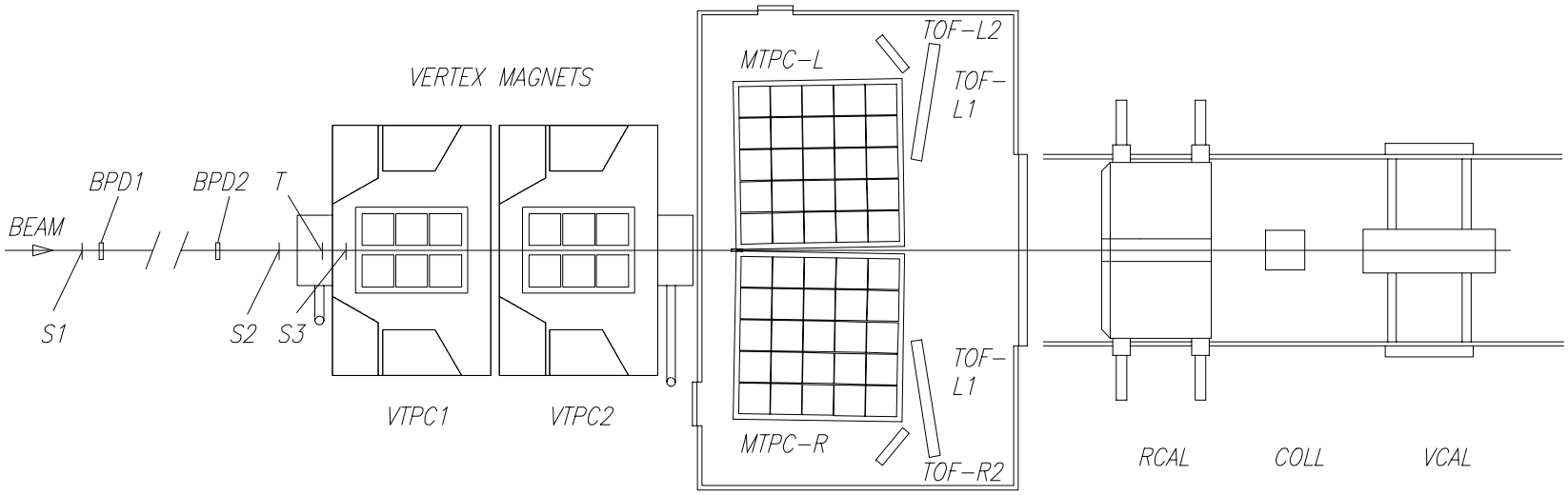

Figure 2.1: Layout of the NA49 experiment. The beam enters the experimental apparatus from the left and impinges on the target (T). Upstream are beam definition detectors (S1, S2, BPD1 and BPD2) and just downstream is the gas Cerenkov trigger detector (S3). The experiment is centered on four large Time Projection Chambers (TPC). Two TPC's (VTPC1 and VTPC2) are located inside superconducting dipole magnets (VERTEX MAGNETS). Two more TPC's (MTPC-L and MTPC-R) are located downstream of the magnets and on either side of the beam line. Four time-of-flight walls (TOF-L1, TOF-L2, TOF-R1, and TOF-R2) supplement the particle identification capabilities of the TPC's. The ring calorimeter (RCAL) is used with the magnets off for measuring transverse energy production. The zero-degree or veto calorimeter (VCAL) is located at the end of the beam line. Its acceptance is defined by an iron collimator (COLL), which is configured to accept neutral and positively charged particles emitted at the target at beam momentum and within 0.5° of the beam.

Therefore, several TPC's covering overlapping momentum ranges were utilized. The detectors must also be constructed using a minimum of low-mass material to limit multiple scattering and ensure good momentum resolution.

The overall tracking length of the TPC's determines the resolution with which the specific ionization of a track can be measured. Most of the particles detected have velocities in the relativistic rise between minimum ionizing ($\beta\gamma \approx 3$) and the Fermi plateau. Identifying particles in this region requires a relative resolution of better than 4%, which can be achieved with a sufficient number of samples over 4 m of track.

2.2 Magnets

The two identical super-conducting dipole magnets are placed in series and centered on the beam line downstream of the target. They have vertical gaps of 100 cm between the coils which, to a large extent, determine the charged particle acceptance of the experiment. Two of the four TPC's are placed in the gaps. The magnet yokes are configured to provide the maximum opening in the (horizontal) bending plane at the downstream end. Each magnet has a maximum current of 5000 A which generates a field of 1.5 T, for a maximum combined bending power of 9 Tm. In normal operation of the experiment, the upstream magnet is operated at the maximum field and the downstream magnet is operated at a reduced field of 1.1 T. This provides charged particles which traverse the full length of the field with a momentum kick in the horizontal plane of about 2.4 GeV/c, which largely separates oppositely charged particles into opposite horizontal hemispheres on opposite sides of the beam line.

The field has large inhomogeneities away from the center of the magnet gaps. Detailed measurements of the field were made in three dimensions with a grid spacing of 4 cm. These measurements were matched to a calculation of the field based on the magnet design. Data is analyzed with a map of the field which uses a combination of the measured and calculated fields. Outside the measured region, only the calculated field is used. Where they overlap, the measurements and calculation agree with 0.5 percent.

2.3 Time Projection Chambers

A TPC is a gas filled tracking device which records the three dimensional position of the ionization trail left by charged particles as they traverse the device. An electric field applied across the gas volume causes the ionization trail to drift to one side of the TPC, where the ionization is amplified and measured. Two of the three dimensions are determined by segmenting the planar readout situated at the end of the drift. The third dimension is determined by recording the time between the point of production of the particle and the arrival of the ionization at the readout plane (the particle flight time from its production to when it deposits ionization is usually small compared to the drift time). This is shown schematically in Figure 2.2. In addition to position information, measurement of the specific ionization by integration of the charge associated with the track along its trajectory provides information on the particle velocity and the magnitude of its charge.

The four NA49 TPC's are rectangular boxes with vertical drift fields and readout at the top of the chambers. Two of the TPC's (Vertex TPC's or VTPC's) are situated inside the dipole magnets. Each of these TPC's occupies a horizontal area of $200\times250\,\mathrm{cm}^2$, has a vertical drift length of 666 cm and consists of a single gas volume with two drift volumes on either side of the beam. The beam itself passes through a gap between the two drift volumes. The highly charged beam particles scatter delta electrons from the TPC gas. The gap provides space for the bulk of these highly ionizing particles to curl up in the magnetic field and prevents the TPC readout from saturating. The two TPC's outside the magnetic field (Main TPC's or MTPC's) are located on either side of

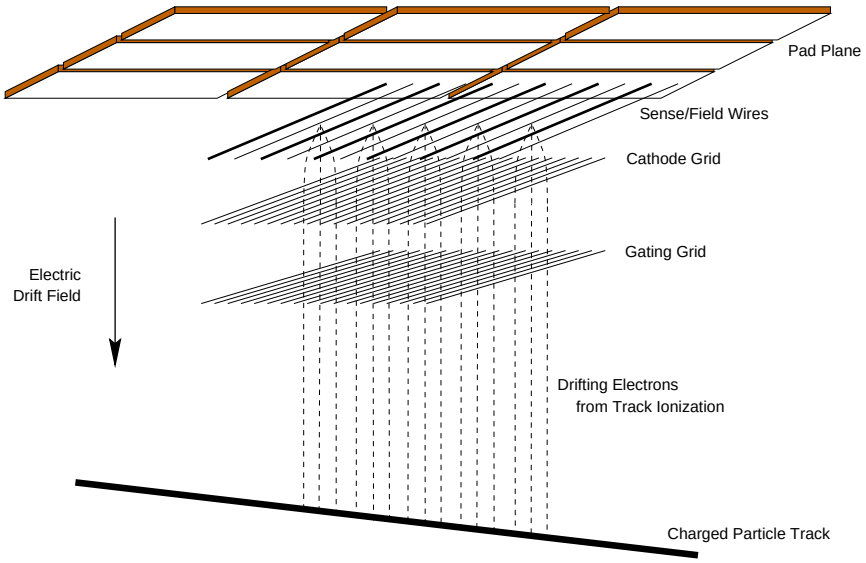

Figure 2.2: Principle of TPC operation. Ionization produced in the TPC gas by a charged particle track drifts vertically and is amplified at the sense wires. Signals are induced on the segmented TPC pad plane above the positions where amplification occurs.

the beam. Each occupies of horizontal area of 4000×4000 cm^2, has a vertical drift length of 1117 cm, and consists of a single drift volume.

Based on results from development studies of various gas mixtures [Al+94, RD396], TPC gases were chosen with low diffusion constants and moderate drift velocities to limit the width of the ionization distributions which arrive at the readout planes. This maximizes the spatial or two-track resolution of the detector. A low mass, lower diffusion gas (Ne 90%, CO_2 10%) was used in the VTPC's to maximize the two-track resolution and space charge effects in the highest track density regions and to further minimize the effect of scattering of delta electrons by the beam as it passes through the TPC's. A higher mass, lower cost gas (Ar 90%, CH_4 5%, CO_2 5%) with comparable resolution in specific ionization was used in the MTPC's.

The drift field in each TPC is maintained by a high voltage plane at the bottom of each chamber. The readout plane is held at ground potential. The uniformity of the drift field is ensured by field cages consisting of aluminized mylar strips which encircle the rectangular drift volumes. The strips are suspended from ceramic posts situated around the edges of the field cage. The drift fields are in the unsaturated range, where drift velocities vary almost linearly with the drift field, so that accurate control and determination of the drift velocities are required. The applied drift fields and resulting drift velocities are 200 V/cm and 1.4 cm/μsec for the VTPC's and 175 V/cm and 2.4 cm/μsec for the MTPC's.

The TPC's are read out via wire proportional chambers. There are six chambers in each VTPC and 25 chambers in each MTPC. Each chamber has three separate planes of wires. The lowest plane is the gating grid, followed by the cathode plane, followed by the sense wire plane. The sense wire plane consists of an alternating pattern of sense wires held at high voltage for charge amplification and field wires held at the cathode potential (ground). Because of the high track density, many tracks can cross each wire and traditional TPC readout of the sense wires is not sufficient. Instead, readout is from a pad plane situated above the sense wire plane. The pad plane is segmented into rectangular copper pads. Signals are induced on the pads above the positions where an avalanche at the sense wires occurs.

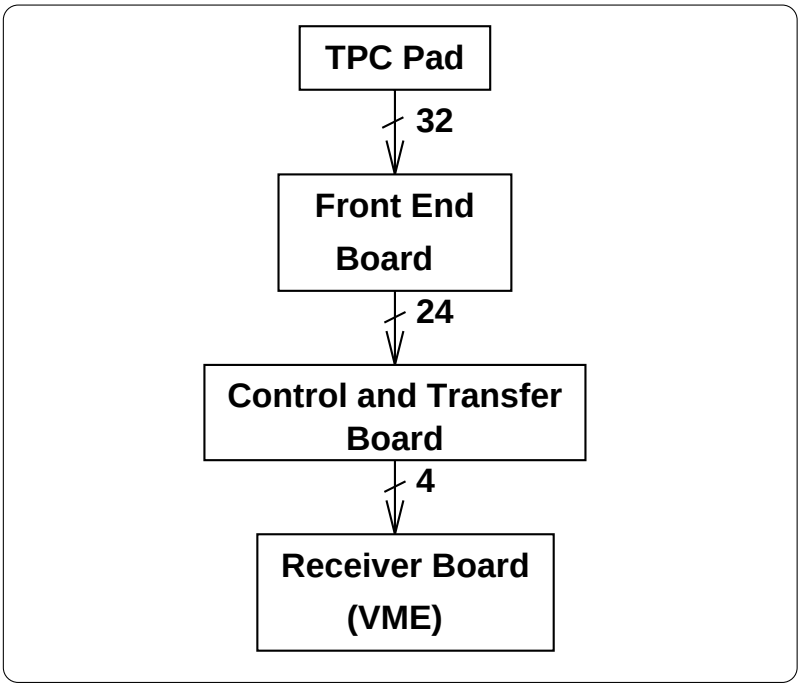

Figure 2.3: Schematic of the TPC readout electronics. Signals originate at the TPC pads and are processed in three stages. Significant multiplexing occurs at each stage to minimize cost and maintenance requirements. The functions of the front end, control, and receiver boards are described in the text.

Both the distance between the pad plane and the sense wires (2–3 mm) and the pad width (3.5–5.5 mm) were optimized to match the width of the induced signal to the width of the drifted ionization charge and to ensure most induced signals would appear on at least three pads. In order to minimize the increase in the width of the induced signal with changing track angle, the pads were angled relative to the sense wire direction as appropriate in each detector area so that the longer pad dimension (16–40 mm) was approximately parallel to the mean track direction in that detector area.

2.4 TPC Readout Electronics and Data Acquisition

The highly segmented TPC's have a total of 182,000 pads. For reasons of cost, system reliability, and packing density, highly integrated electronics were required to readout the large number of densely packed channels. Performance requirements included (1) a low intrinsic noise to allow operation of the TPC's at relatively low gain, (2) signal shaping and sampling rate to match the pad signal characteristics, and (3) sufficient dynamic range to cover variations in the ionization signal of singly charged particles. The modest event readout rate of 1 event/second allowed significant multiplexing of the data, which reduced cost and maintenance requirements.

The readout system consists of three major modules, shown in Figure 2.3. The front-end card is directly connected to 32 TPC pads. It amplifies and shapes the pad signals and provides temporary analog storage of signal samples at a rate of 10 MHz. After the chamber drift time (50 μsec), the stored samples are digitized and multiplexed onto a flat ribbon cable.

The control and transfer (CT) boards, also mounted on the TPC's, collect the data from 24 front-end cards connected via flat ribbon cables. The data are multiplexed onto a fiber optic cable for transmission to the receiver boards which are located off the detector inside the NA49 counting house. The CT boards also provide the front-end board with power and control signals.

A receiver board consists of four modules, each of which receives the multiplexed data from a CT board via the fiber optic link, subtracts pedestals previously measured and stored on board for each channel and time sample, and saves the data in an input buffer for further processing. The input buffers have 32 pages for accumulating up to 32 events. Once the first event has been received, while events are still being accumulated, each receiver board module compresses the pedestal subtracted data and saves the result in an output buffer. The receiver boards are located in six VME crates.

More detailed design and performance information on the readout electronics system can be found in [Bi+97].

The data acquisition system is centered on one master VME crate and six slave VME crates. The master crate contains a master processor for controlling the system and dual-ported memory buffers for organizing the event data before writing it to tape. The slave crates contain the receiver boards and a slave processor. The full event data is written to a high speed (up to 16 MByte/second) tape drive. The data acquisition software is organized as a set of concurrent processes under control of a single process running on the master processor.

2.5 Calorimetry and Trigger

Online event characterization and triggering is accomplished by beam definition detectors located in the beam line upstream of the target and interaction counters and calorimeters downstream of the target. Three beam detection counters and three beam position detectors are employed to provide a precise reference start time for the time-of-flight detectors and to measure the charge, position, and trajectory of the incoming beam particle.

For central Pb + Pb collisions, the primary trigger detector is a zero degree calorimeter (ZDC) located about 20 m downstream of the target behind a collimator. The opening of the collimator is adjusted so that beam particles and un-interacted or spectator protons, neutrons, and fragments from the beam reach the calorimeter. The ZDC consists of an electromagnetic section of alternating lead and scintillator plates of a total of 16 radiation lengths followed by a hadronic section of iron and scintillator plates of 7.5 interactions lengths. Light from the scintillators is collected by acrylic readout rods and transmitted to photomultipliers.

Central collisions of Pb beam nuclei with a heavy nuclear target remove a large fraction of the beam energy and these events are clearly identifiable by a small E_0 measurement by the calorimeter. Triggering is accomplished by placing an upper threshold on the summed signals from the ZDC photomultipliers in coincidence with valid signals from the beam detectors.

Because of the significant distance and amount of material between the target and the ZDC, this method does not work for triggering on non-central Pb + Pb collisions. An interaction between a beam particle and the light nuclei in the detector materials and gases between the target and ZDC results in E_0 measurements which mimic non-central Pb+Pb collisions. To trigger on such collisions, the Cerenkov counter (S_3) shown in Figure 2.4 is used to detect the Cerenkov light produced by beam particles or fast secondary particles in the gas region immediately downstream of the target. This counter consists of a gas filled volume which surrounds the target, a thin reflective mylar mirror 17 cm downstream of the target to reflect produced Cerenkov light, a thin-walled plastic foam tube internally coated with aluminum for guiding the reflected light, and a photomultiplier.

Triggering is accomplished by placing an upper threshold on the signal from S_3 in coincidence with valid signals from the beam detectors. Because the detected Cerenkov light varies approximately as the squared charge of the highest charge beam fragment and the counter has an estimated pulse height resolution of 10%, the trigger threshold can be set to discriminate beam particles from heavy beam fragments, which are produced in very peripheral Pb+Pb collisions. However,

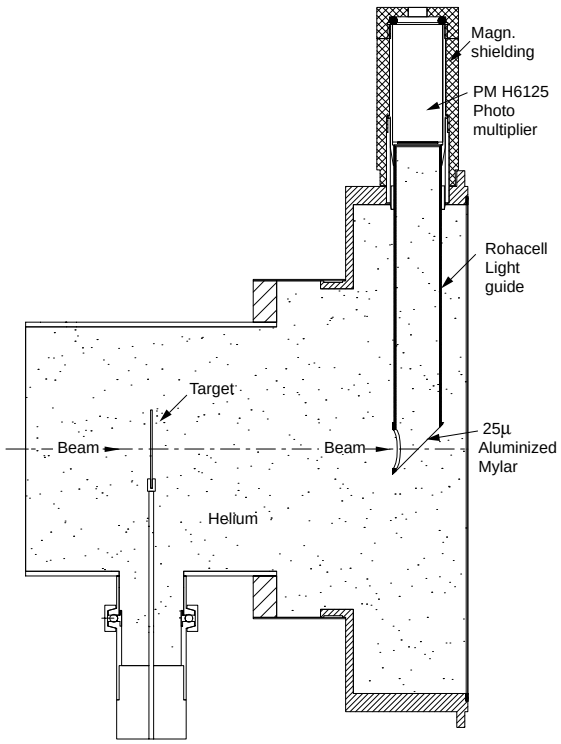

Figure 2.4: Gas Cerenkov counter for detection of Pb beam particles and triggering on peripheral Pb + Pb collisions.

interaction between the Pb beam and the gas surrounding the target produces an S_3 signal similar to peripheral Pb+Pb collisions. In practice, the threshold is based on a compromise between acceptance of peripheral Pb+ Pb events and rejection of the non-target event background. Off-line event cuts based on reconstructed TPC tracks and the signal in the ZDC are made to further reduce the event background and characterize the collision geometry. These are discussed in Section 2.6 and in Chapter 3.

2.6 Data Sample

The data sample used in this work was recorded in the fall of 1996. The ^{208}Pb beam produced by the CERN SPS with a beam energy of 158 GeV/nucleon collided with a 224 mg/cm^2 natural Pb target. Events were selected with the S_3 interaction trigger at two different threshold settings. The first setting maximized acceptance of peripheral Pb + Pb collisions, but accepted about 50% non-target event background. The lower threshold resulted in about 30% non-target event background with more bias against the most peripheral Pb+ Pb collisions. A total of 260,000 events were recorded under both trigger condition. Of this total, 160,000 events passed the off-line event cuts and are used in this thesis. These events consist of digitized data from the TPC's, TOF detectors, calorimeter, and beam and trigger detectors. The bulk of the data is from the TPC's. Uncompressed, each event is 90 MByte. The compressed events occupy 1-10 MByte, depending on event centrality.

The raw S_3 pulse height distributions for these event samples is shown in Figure 2.5a. It is seen that the lower S_3 threshold can be simulated with an off-line cut at an S_3 ADC value of 83.

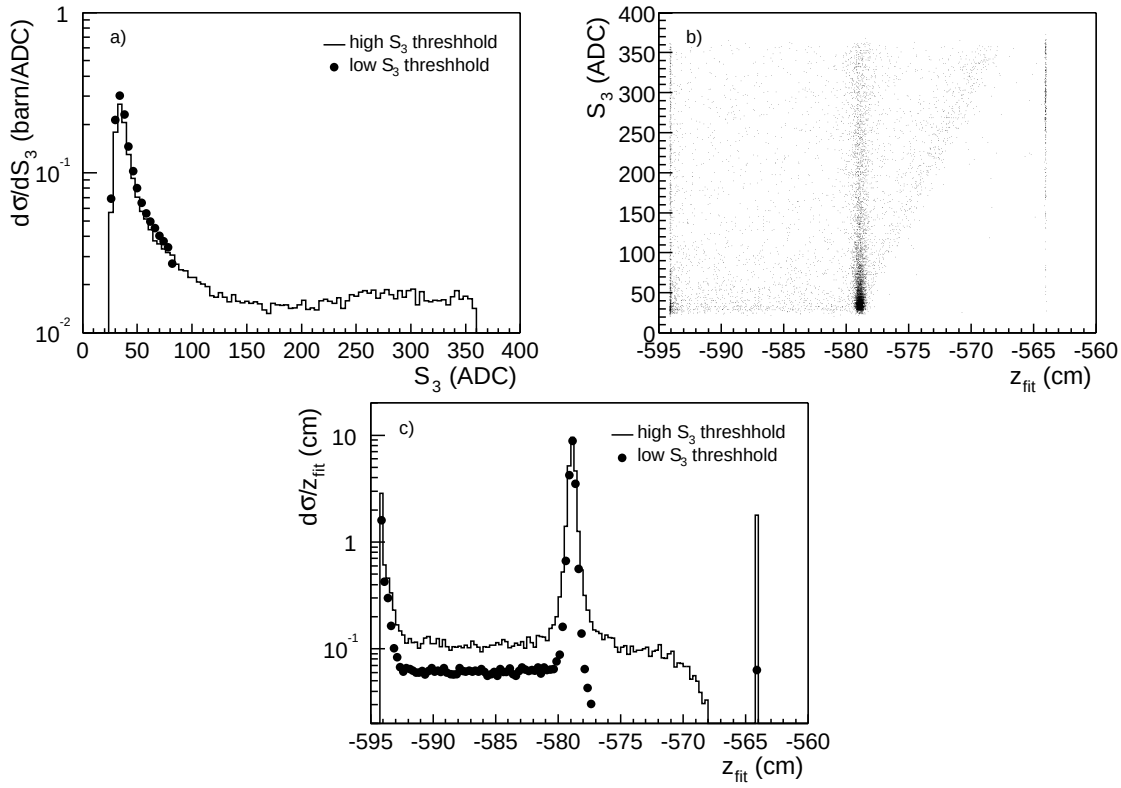

Figure 2.5: S_3 and fitted vertex position distributions. Panel a) shows the raw S_3 spectra for the high threshold and low threshold triggers. Panel b) shows the correlation between S_3 and the primary vertex fit coordinate along the beam direction. Panel c) shows the distribution of the primary vertex fit coordinate for each of the two S_3 threshold settings.

As described in Chapter 3, the measured TPC tracks are used to fit the three dimensional position of interaction point. The correlation between the S_3 signal and the fitted position of the interaction point along the beam line is shown in Figure 2.5b. Here a clear peak at the nominal target position is seen. Peaks at -15 cm and +15 cm are due to a cutoff in the fitting procedure. Downstream of the target, events above the upward sloping diagonal are beam particles which pass through the target and interact in the gas between the target and the S_3 mirror. Events are not seen below the diagonal because beam particles that interact downstream of the target produce a minimum Cerenkov signal that is proportional to the distance between the target and the interaction point. Additional Cerenkov light can be produced by large fragments from the Pb + gas interaction. Events upstream of the target are uniformly distributed in interaction position, as seen in Figure 2.5c. Since the target shadows the S_3 mirror from light produced by beam particles which interact before the target, all events which occur downstream of the last beam counter and upstream of the target are accepted by the trigger. However, Figure 2.5c shows that the good resolution of the off-line fit of the interaction position can be used to select target events, with only small non-target event contamination. This event selection and an estimate of the non-target background is discussed in Chapter 3.

Although the S_3 detector provides a good means of discriminating un-interacted beam particles from peripheral Pb + Pb collisions, it does not provide a good measure of the centrality of a collision. On the other hand, it is known that measurement of E_0 is well correlated with the

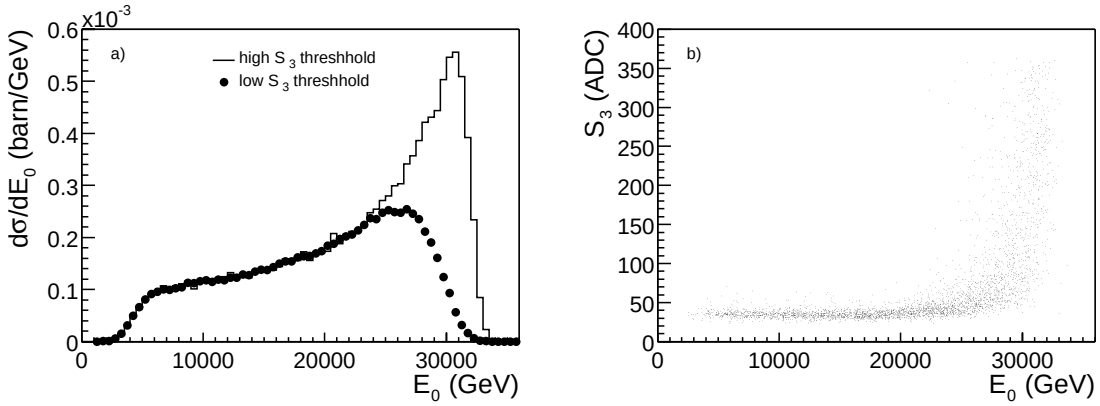

Figure 2.6: E_0 and S_3 distributions. Panel a) shows the E_0 distributions for both of the S_3 threshold settings. Panel b) shows the correlation between S_3 and E_0.

geometry of the collision [Al+95, Ap+98c]. The calibrated E_0 distributions for the two S_3 samples are shown in Figure 2.6a. The better acceptance of the high S_3 threshold for peripheral collisions can be seen at large values of E_0. Figure 2.6b shows the correlation between S_3 and E_0. Chapter 3 and appendix C provide further details on estimating collision centrality and the separation of events into several centrality classes.

Chapter 3

Data Analysis

3.1 Overview

This thesis reports on the measurement of the spectra of charged hadrons from centrality selected Pb + Pb collisions. Particle identification and momentum determination are accomplished with the NA49 TPC's. The specific ionization (dE/dx) measured by the MTPC's is used to obtain identified spectra of $\pi^{\pm}$, $K^{\pm}$, proton, and $\overline{p}$ over the MTPC acceptance. Tracking in the VTPC's without consideration of dE/dx is used to extend the MTPC acceptance for unidentified hadrons ($h^{\pm}$). The collision centrality is determined by the zero-degree calorimeter (ZDC) which measures the energy (E_0) carried by the projectile spectator nucleons. This chapter describes the analysis procedures for obtaining the particle and event information from the TPC's and ZDC. The analysis procedure consists of:

1. Raw data are calibrated and converted into tracks having momentum and particle identification information, along with quality information used for rejecting background events and low quality tracks.

2. Events are segregated into six centrality bins according to E_0; the impact parameter mean and range in each bin are estimated.

3. Tracks in each centrality sample are segregated into momentum bins, and the raw spectra are determined by fitting the dE/dx distribution in each bin.

4. Corrections for feed-down from decaying long-lived hadrons, tracking inefficiencies and acceptance, and particle mis-identification are estimated and applied.

5. Corrected spectra obtained in fixed momentum bins are transformed into distributions in y or x_F and extrapolated to phase space outside the acceptance where possible.

The following sections describe these steps in more detail.

3.2 Calibration and Reduction of Raw Data

3.2.1 Calibration

Calibration of the ZDC was described in detail in [HMSV95] and [Hua97]. For data taking, the gains of the four photomultipliers are adjusted so that a beam of hadrons striking the center of the calorimeter generates four equal signals. Digitized signals from each sector are corrected for the pedestals and small non-linearities of the ADC's and summed in the off-line analysis. Signals

from Pb beam particles which pass through the detector without interacting are recorded during the run and used along with the known beam energy to determine the calibration constant to convert measured ADC values into energy.

Calibration of the TPC data is divided into geometry calibrations and pulse height calibrations. A geometry database is maintained which includes information from TPC as-built data, optical survey of the detector positions, and corrections based on experience gained during the data analysis. TPC drift velocities are measured in a test chamber and recorded with the data. The measurements are corrected for atmospheric pressure and temperature variations. Distortions in the geometry occur because of local inhomogeneities in the drift field, primarily in the transition between the drift region and the readout chambers, and $\boldsymbol{E}\times\boldsymbol{B}$ effects due to the non-principal components in the magnetic field. Corrections are applied for these distortions after cluster finding (see below).

TPC pulse height data are calibrated for TPC sector and electronics gain variations once during the run period by releasing radioactive ^{83m}Kr gas into the TPC's, and matching the resulting local ionization spectrum measurements to a Monte Carlo simulation. Several effects of the readout chambers and electronics cause track ionization to influence the recorded pulse height of nearby tracks whose ionization arrives at the readout plane at the same or later times. In a region with a high density of tracks, this can lead to significant shifts in the recorded pulse heights and degradation of the TPC particle identification capability. Detailed measurement and study of these effects have been made and corrections for them are applied to the raw data [Rol99]. Additional corrections are applied after cluster and track finding for charge losses due to electron attachment during drift and cluster truncation due to the ADC threshold imposed by the data acquisition. Specific energy loss is obtained by normalizing the cluster charge by the actual track length across the pad row, which may vary because of finite track-pad row crossing angles. After these calibrations have been performed, a sample of the data is analyzed and the readout sector gain constants are adjusted to maximize the dE/dx resolution and to fix the parameterization of the dE/dx response. This procedure is discussed more fully in Section 3.4. After event reconstruction, a second pass is made through the data to correct for time variation in the sector gains, which is mainly due to atmospheric pressure changes and voltage setting uncertainties. The correction for time variation is accomplished by normalizing the average of the cluster charges within each sector taken over fixed event recording intervals to the sector average over all events.

3.2.2 Cluster Finding and Tracking

Cluster finding in each pad row is accomplished by finding contiguous charge regions in the two-dimensional pad-time space and then computing a charge weighted mean position of the region. The cluster centers are used for finding tracks. The total cluster charge is obtained by simply summing the digital pulse heights of each pixel contained in the cluster.

Track finding is accomplished in several steps, using both projective and step-wise approaches. Tracking begins in the MTPC's, where tracks are straight and sparsest, making track finding easier. Momenta are assigned to the found tracks based on their positions and angles, under the assumption that they are primary (i.e. they come from the Pb + Pb interaction vertex). These tracks are then extrapolated into the VTPC's, and predicted cluster positions are saved. The VTPC2 clusters are then searched for tracks which lie near the predictions. Remaining clusters not associated with the MTPC predictions are searched for additional tracks. These additional tracks are then extrapolated to the other TPC's. MTPC tracks which had predicted tracks in VTPC2 but for which no matching track was found are discarded. This procedure is repeated for VTPC1. Finally, tracks are searched again in the MTPC using the VTPC1 and VTPC2 predictions and any remaining tracks unmatched between TPC's are associated, if possible. After track finding, an additional quality assessment is performed which identifies and repairs split tracks. Also, in the highest density region of the MTPC where many clusters overlap, the found track position and angle information is used to re-fit the found clusters from the raw data to obtain a better estimate of the

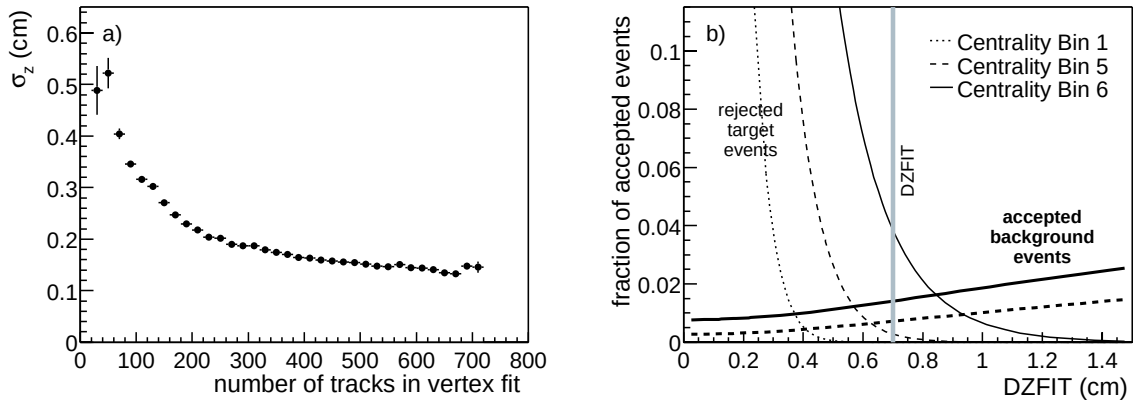

Figure 3.1: Primary vertex cut details. Panel a) shows the resolution of the z-coordinate of the primary vertex fit as a function of the number of tracks used in the fit. Panel b) shows the estimates of target events rejected (thin lines) and background events accepted (bold lines) as a function of the event vertex position cut, $|z_{Fit} - z_{TGT}| \leq$ DZFIT. The estimates are shown as a fraction of the total number of events accepted in three of the six centrality bins. For centrality bins 1–4 (2–4 not shown), there are no background events. The value of DZFIT used for the data analysis is indicated (grey vertical line).

charge contained in overlapping clusters, which improves the specific ionization measurement in this region.

Momenta for the found tracks are determined using a chi-square minimization of cluster residuals from a trajectory determined by Runge-Kutta integration through the magnetic field. Clusters are assigned position errors based on a parameterization of the found cluster residuals as a function of position in the TPC's and as a function of the track-pad row crossing angles. During fitting, cluster errors are increased along the track length to account for multiple scattering of the actual charged particle. Momentum fitting is first accomplished using only the cluster data. A second fit is obtained imposing the additional constraint that the track starts from the primary interaction point, as determined by the intersection of the beam trajectory and the target.

3.2.3 Event and Track Quality Cuts

Quality cuts are imposed to reject background events and tracks and to reject poorly reconstructed tracks. Background events come from beam–gas interactions which can occur both upstream and downstream of the target. The event selection is based on a fit of the primary vertex position using the TPC tracks. The resolution of this fit depends on the multiplicity of found tracks and is shown in Figure 3.1a. Events are rejected if this fit does not converge. This occurs only for the lowest multiplicity events. Additionally, events are accepted when the z-position of the vertex is sufficiently close to the nominal target position, $|z_{Fit} - z_{TGT}| \leq$ DZFIT. The magnitude of DZFIT is chosen to limit the fraction of background events in the accepted events samples while minimizing the bias imposed against peripheral events. How this optimization is accomplished is shown in Figure 3.1b. Estimates of the accepted background and rejected target event fractions as a function of DZFIT are shown for three centrality samples. For centrality bin 1 (and also 2, 3, and 4, which are not shown), there are no background events because no beam–gas events have an E_0 signal compatible with these more central Pb + Pb events. For the more peripheral centrality bins, the background fraction rises linearly with increasing DZFIT, once DZFIT exceeds the resolution of the fit of the primary vertex position. On the other hand, more Pb + Pb events are rejected as

Cut Name	Cut Equation	Nominal Value
DZFIT	$\lvert z_{fit} - z_{target} \rvert \leq$ DZFIT	0.7 cm
POTLEN	$N_{cl,pot} \geq$ POTLEN	20 for each TPC
CLRAT	$N_{cl}/N_{cl,pot} \geq$ CLRAT	0.5
BXMAX	$b_x^2/\text{BXMAX}^2 + b_y^2/\text{BYMAX}^2 \leq 1$	4.0 cm
BYMAX		0.5 cm
PHIMAX	$\lvert \phi - \phi_{bend} \rvert \leq$ PHIMAX	54°

Table 3.1: Event and track quality cuts.

DZFIT is decreased. For this thesis, a fixed cut of DZFIT = 0.7 cm was chosen for all centrality bins. This value yields a maximum background fraction for centrality bin 6 of less than 1.5%.

The potential length of a found track is based on detector geometry and is specified by the total number of clusters it could have along its trajectory. The track cuts are based on the potential length, the actual number of found clusters, and the quality of the momentum fit obtained with the primary vertex constraint. An additional cut is made on the azimuthal emission angle of the track. The potential length (POTLEN) is calculated as a function of track momentum for each TPC from a detailed simulation of the detector including $\boldsymbol{E}\times\boldsymbol{B}$ effects, as described in Appendix D. Cluster losses can occur randomly, for instance because of energetic δ-electron production, or in a high density region of a TPC. The number of found clusters on a high quality track will be a large fraction of the track's potential points. In the case of a split track, one or both segments will have fewer than 50 percent of the potential points. Figure 3.2 shows the ratio between the number of found clusters and the potential length (CLRAT) for track segments in each TPC separately and for all TPC's summed. The acceptance of each TPC is defined by a cut on the minimum potential length of a track. A quality cut is imposed on the ratio of the number of found clusters to the potential length in each TPC. If a track passes the acceptance cut for one of the VTPC's, it must also pass the quality cut for that TPC. This requirement reduces background from secondaries which are produced downstream of the VTPC's. Because the momentum of such MTPC-only tracks is determined by assuming they come from the primary vertex, a secondary will be assigned an incorrect momentum and distort the $\langle dE/dx \rangle$ distributions. Finally, cuts are placed on the azimuthal emission angle of the track from the primary vertex and on the distance between the point at the target position to which a track projects and the position of the primary vertex determined from all tracks in the event. The azimuthal angle cut selects only those tracks which are reconstructed with an emission angle which is in the same direction that the magnetic field bends the track ($\lvert \phi - \phi_{bend} \rvert \leq$ PHIMAX). The track projection cut rejects tracks which project to the primary vertex outside an ellipse (defined BXMAX and BYMAX) around the fitted primary vertex position. These cuts act to further reduce the background due to secondaries from long-lived hadrons decaying away from the target position and due to electrons produced by conversion in the detector materials. The background tracks are produced downstream of target and therefore tend either not to project back to the primary vertex position, or to project back as "wrong-side" tracks whose trajectory crosses the beam line in the magnetic field. Nominal cuts applied to the data are given in Table 3.1.

3.3 Centrality Determination

This section summarizes the several approaches which are used to estimate the centrality range of each event sample. Each approach yields a measure of the mean and dispersion in the collision impact parameter (b) or in the number of participating nucleons (N_{part}) in each centrality bin. Additional details can be found in Appendix C.

Figure 3.3 shows the windows placed on E_0 which define the centrality bins. The estimates

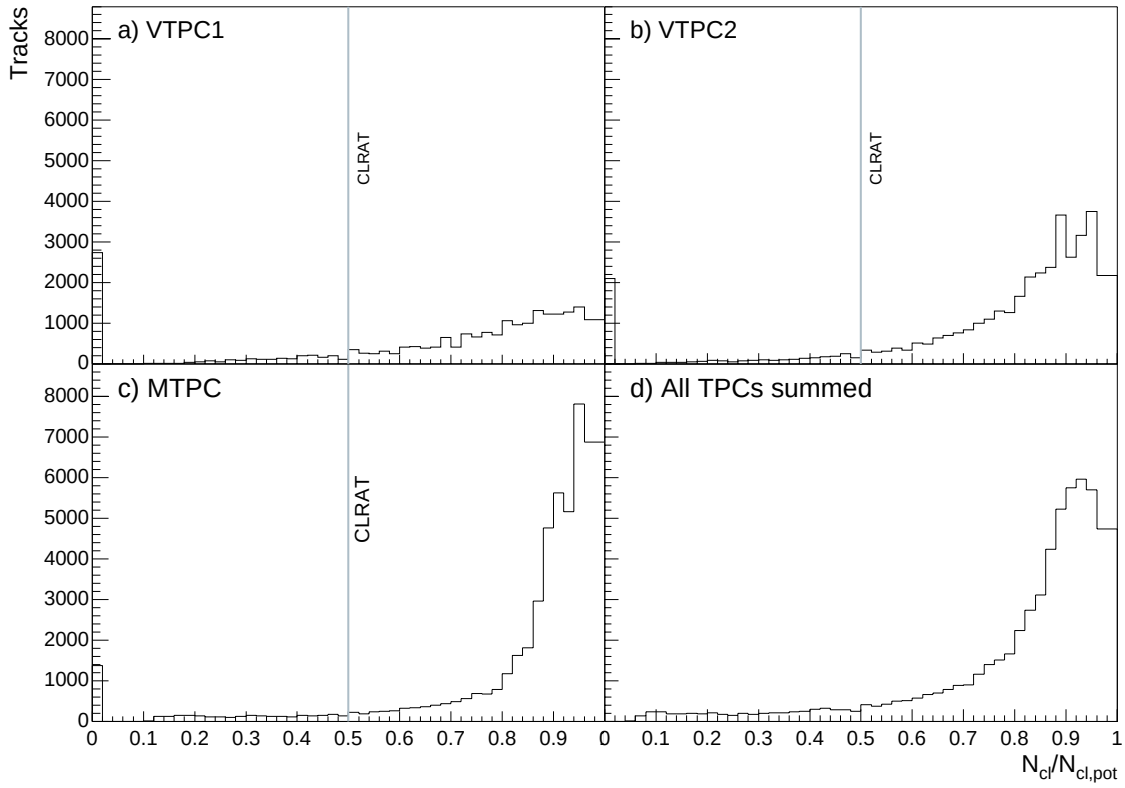

Figure 3.2: Distribution of the ratio of number of clusters to potential length of found tracks. Panels show results for each TPC separately and summed values for all tracks. The minimum ratio applied as a track quality criterion is shown. Tracks below this ratio occur infrequently and are usually of low quality. Most come from a tracking software failure which splits a track into two or more pieces. A cut of CLRAT = 0.5 ensures that at most one of the split pieces will be used.

of b and number of participants are based on either the E_0 measurement or the measured final spectra.

The first approach estimates b in each centrality bin by assuming that the mean E_0 ($\langle E_0 \rangle$) for an event sample increases monotonically with increasing b, so that

$$\int_0^{E_0} \frac{d\sigma}{dE_0'} dE_0' = \int_0^{b} \frac{d\sigma}{db'} db'$$

where $d\sigma/dE_0$ is the measured E_0 spectrum corrected for the trigger bias and $d\sigma/db$ is closely given by the geometrical cross-section $2\pi b$ since the probability of at least one nucleon-nucleon interaction is large, up to very peripheral collisions. Obtaining a reasonable estimate of $\langle b \rangle$ over a window in E_0 requires a small dispersion in b at fixed E_0. The dispersion is estimated by model calculation and Monte Carlo simulation of the ZDC to be about 1 fm.

The second approach utilizes a simulation of the NA49 apparatus and E_0 response to correlate b with the E_0 signals produced by events simulated at fixed b by an event generator. This method relies on the accuracy of both the event generator and experimental simulation. In Appendix C, this simulation is shown to match the measure E_0 spectrum well.

The third method for estimating centrality uses the E_0 measurements as a direct measure of projectile spectator nucleons. E_0 is composed of the kinetic energy carried by the spectators plus

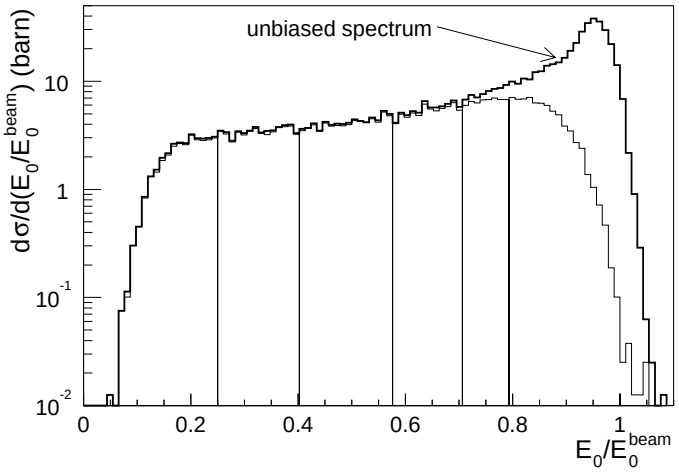

Figure 3.3: E_0 spectrum and centrality bins. The upper curve shows the estimate of the unbiased Pb + Pb inelastic cross section which has a total integral of 7.1 barn. The lower curve shows the bias imposed by the event trigger and off-line event selection. This spectrum is divided into six centrality bins.

produced particles accepted by the collimator, which include high momentum charged particles and neutral particles not swept out of the beam trajectory by the magnetic field. This contamination and the effect of calorimeter non-uniformity and shower leakage from the collimator are estimated and corrected using the experimental simulation.

The final method for estimating centrality extrapolates the measured charged particle spectra to obtain the net baryon number carried by all particles emitted from the collision into phase space regions other than the spectator regions. The net protons ($p - \overline{p}$) are measured over most of phase space forward of the center of mass and only a small extrapolation to beam rapidity is needed. Since the net neutrons ($n - \overline{n}$) and hyperons ($Y - \overline{Y}$) are not measured, their contribution must be estimated. $n - \overline{n}$ is estimated from $p - \overline{p}$ using a scaling factor determined from VENUS and RQMD. This scaling factor is close to one and only weakly depends on rapidity. The $Y - \overline{Y}$ yield is estimated from the measured $K^+ - K^-$ yield using the constraint of conservation of strangeness. Since the net strangeness carried by the hyperons is compensated by the net strangeness carried by the kaons, and the neutral mesons ($K^0 - \overline{K^0}$) should carry approximately the same net strangeness as $K^+ - K^-$,

$$Y - \overline{Y} = (2 - \beta)(K^+ - K^-),$$

and

$$N_{\rm part} = (2 + \alpha)(p - \overline{p}) + (2 - \beta)(K^+ - K^-), \tag{3.1}$$

where α accounts for the scaling factor between $p - \overline{p}$ and $n - \overline{n}$ and β accounts for multi-strange baryons.

Figure 3.4 shows the correlation between b and E_0 as determined by the simulation. The E_0 ranges and the estimates of centrality are shown in Table 3.2. The E_0 range for the most central bin was chosen to correspond to the most central five percent of the Pb + Pb interaction cross-section. This matches the central event sample used in [Ap+99]. The next bin corresponds to a total of 7.5 percent of the cross-section. Taken together, these bins match the data taken in 1996 with the central interaction trigger. Data in these first two bins can then be supplemented by the central trigger data to achieve sufficient statistics. The remaining bins were chosen to achieve sufficient sampling in centrality while maintaining good statistics in each bin. The $N_{\rm part}$ estimates are based

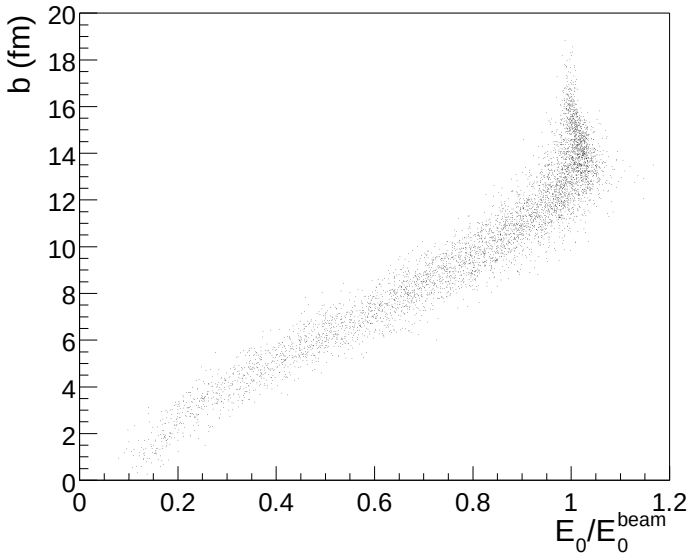

Figure 3.4: Correlation between impact parameter and E_0 as determined from an event generator and simulation of the zero-degree calorimeter (see Appendix C for details). At fixed E_0, the mean square deviation in impact parameter is about 1 fm. At large b, the recorded E_0 exceeds the beam energy due to the non-uniformity in the calorimeter response.

Bin	E_0/E_0^{beam} Range	Fraction of Cross Section	b Range (fm)	N_{part}	N_W
1	0-0.251	0.05	0-3.4	366±8	352
2	0.251-0.399	0.075	3.4-5.3	309±10	281
3	0.399-0.576	0.11	5.3-7.4	242±10	204
4	0.576-0.709	0.10	7.4-9.1	178±10	134
5	0.709-0.797	0.10	9.1-10.2	132±10	88
6	0.797-	0.57	10.2-	85±6	42

Table 3.2: Centrality bins used for data analysis. Also shown are the estimates of the impact parameter range and mean number of participating and wounded nucleons for each bin.

on an average of the results. An additional column in Table 3.2 shows the number of wounded nucleons (N_W) obtained from a Glauber calculation using the spectator-participant model of A + A collisions for the b distribution in each centrality bin. For all bins, this result is always smaller than N_{part} determined from the other methods. This difference is likely due to the addition of participants from cascading within what would otherwise be the spectator portions of the colliding nuclei. The relative difference is largest for the most peripheral collisions where the spectator portion of the nuclei is the largest.

3.4 Raw Spectra Determination

Charged particles are identified by combining the measurement of their momentum with the magnitude of their specific energy loss (dE/dx) in the TPC gas, which occurs through excitation and ionization of the gas atoms. The mean energy loss per unit path length depends on the particle

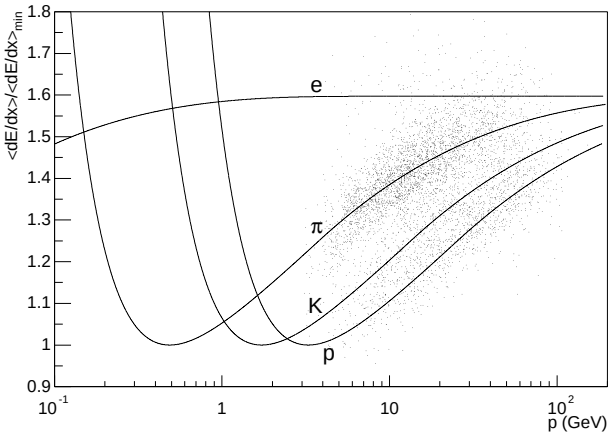

Figure 3.5: Bethe-Bloch distribution, parameterization, and $\langle dE/dx \rangle$ data for positively charged particles (100 events). $\langle dE/dx \rangle$ is a function of velocity. At fixed momentum (p), particles of different mass are separated by the $\langle dE/dx \rangle$ measurement. Curves and data have been normalized to the minimum ionization, $\langle dE/dx \rangle_{min}$, which occurs at $\beta\gamma \sim 3$.

velocity (β) and is given by the Bethe-Bloch formula,

$$\frac{dE}{dx} = C_1 \frac{z^2}{\beta^2} \left[\log \left(C_2 \beta^2 \gamma^2 \right) - 2\beta^2 + \text{corrections} \right], \tag{3.2}$$

where z is the particle charge, $\gamma = (1-\beta^2)^{1/2}$, C_1 and C_2 are parameters which depend on the properties of the material, and the correction term limits the energy loss at low and high particle energies. As shown in Figure 3.5, above $\beta\gamma \sim 3$ and below the plateau at very high velocities, which is the range of interest for this thesis, particles of known momentum can be separated by mass with the dE/dx measurement.

In practice, the ability to identify individual particles is limited by the resolution of the dE/dx measurement, which depends both on the total charge in each cluster and on the number of clusters on a track. Because the distribution of energy deposited by any single ionization is broad and characterized by a long, high energy tail from near head-on collisions with the atomic electrons and because the number of primary ionizations contained in a cluster is small, the cluster charge distribution is also broad and has a long tail. Previous studies have determined that resolution with which the specific energy loss is determined can be improved by calculating a truncated mean ($\langle dE/dx \rangle$), truncating the charge distribution at the high, and possibly the low end in the calculation of the mean. For these data, the best resolution is obtained by calculating the mean from clusters in the lowest 50 percent of the charge distribution on a track. The resulting resolution in the MTPC was studied for fixed number of clusters ($\mathrm{N_{cl}}$) and fixed $\langle dE/dx \rangle$ and found to obey the parameterization

$$\frac{\sigma_{\langle dE/dx \rangle}}{\langle dE/dx \rangle} = A \left(\frac{\langle dE/dx \rangle}{\langle dE/dx \rangle_{min}} \right)^{\lambda} \frac{1}{\mathrm{N_{cl}}^{\alpha}} \tag{3.3}$$

where $A \simeq 29.5$ percent, $\alpha \simeq 0.5$, $\lambda \simeq 0.7$, and $\langle dE/dx \rangle_{min}$ is the mean ionization produced by a minimum ionizing particle.

For tracks with at least 20 clusters in the MTPC, the resulting $\langle dE/dx \rangle$ distribution for tracks of known particle type and fixed momentum is nearly Gaussian with a resolution of about four percent. Since the proton-K and K-π separation given by Equation 3.2 is also on this order, the π,

K, and proton distributions overlap. Therefore, the $\langle dE/dx \rangle$ for each selected track is accumulated into histograms in small bins of total momentum (p) and $p_\perp$and these $\langle dE/dx \rangle$ spectra are fit to extract the yield of each particle species in each p-$p_\perp$ bin.

For such a fit, the positions, yields, and widths of the contribution of each particle species to the $\langle dE/dx \rangle$ spectra should be free parameters. However, for most p-$p_\perp$ bins, a completely free fit does not converge well. Therefore, assumptions about the $\langle dE/dx \rangle$ spectra and the TPC performance are made to further constrain the fits. For the results presented here, the following assumptions were made about the $\langle dE/dx \rangle$ spectra:

1. The mean for each particle species obeys the parameterization of Equation 3.2 calibrated to the data, up to an overall scaling factor that is independent for each p-$p_\perp$ bin. The scaling factor ranges over approximately 0.98–1.02 in comparison to a typical relative width (σ/μ) of 4-5 percent. In many p-$p_\perp$ bins, the scaling factor is well determined because the yield of one particle species is dominant.

2. The resolution for each particle species obeys the parameterization of Equation 3.3, with α and λ fixed at the measured values, and with only A independent for each p-$p_\perp$ bin.

3. The positions and resolution of neighboring p-$p_\perp$ bins should exhibit similar deviations from the parameterizations, since the tracks which populate these bins are located nearby in the TPC's. This assumption is enforced by fitting the p-$p_\perp$ bin of interest along with the bins in a surrounding window in p-$p_\perp$ space. In performing this coupled fit, the free parameters from the items 1 and 2 are common for all bins in the window, whereas the yields remain independent for each bin.

Imposing these conditions results in fits that converge well and gives reasonable fit quality. Several example fits are shown in Figure 3.6. In most bins, these fits yield $\chi^2/d.o.f.$ between 0.75 and 1.25. In a few bins, $\chi^2/d.o.f.$ up to 2 are obtained. In these bins, error estimates from the fits are scaled to account for the lower fit quality. The fitted means are compared to the parameterizations in Figure 3.7. Such fits are performed for each p-$p_\perp$ bin in each centrality sample for which there are enough entries (at least 250). The resulting yields are saved for further analysis.

For unidentified hadrons with momenta outside of the MTPC acceptance, the VTPC specific ionization measurement is used only to exclude electrons from the accumulated yields. An upper cut on $\langle dE/dx \rangle$ is placed at -2σ from the electron peak position predicted by the $\langle dE/dx \rangle$ parameterization. If this cut is closer than 3σ to the pion peak position, which occurs above about 10 GeV, no cut is applied. However, this is already within the MTPC acceptance where the identified hadron yields from the $\langle dE/dx \rangle$ fits are used to determine the $h^\pm$ spectra.

3.5 Corrections to Spectra

The yields from the $\langle dE/dx \rangle$ fits must be corrected for acceptance, tracking inefficiencies, and backgrounds from decay of long-lived hadrons to obtain the spectra of charged particles emitted directly from the collision. These corrections are obtained by embedding a few simulated tracks of known species and momentum into real events, processing the combined event through the full reconstruction chain, and identifying whether the embedded tracks result in reconstructed clusters and found tracks which meet the kinematic and quality criteria. Since tracking inefficiency and precision may depend upon the environment in which a track is found, embedding has the advantage over full event simulation that a realistic tracking environment is automatically provided.

In addition, a significant fraction of $K^\pm$ can be lost by decay in flight. Since the $K^\pm$ spectra are not central to this thesis, only an approximate correction was made by assuming that the entire fraction of kaons which decay before reaching the mid-plane of the MTPC are lost. The error associated with this correction was conservatively estimated by also determining the correction for

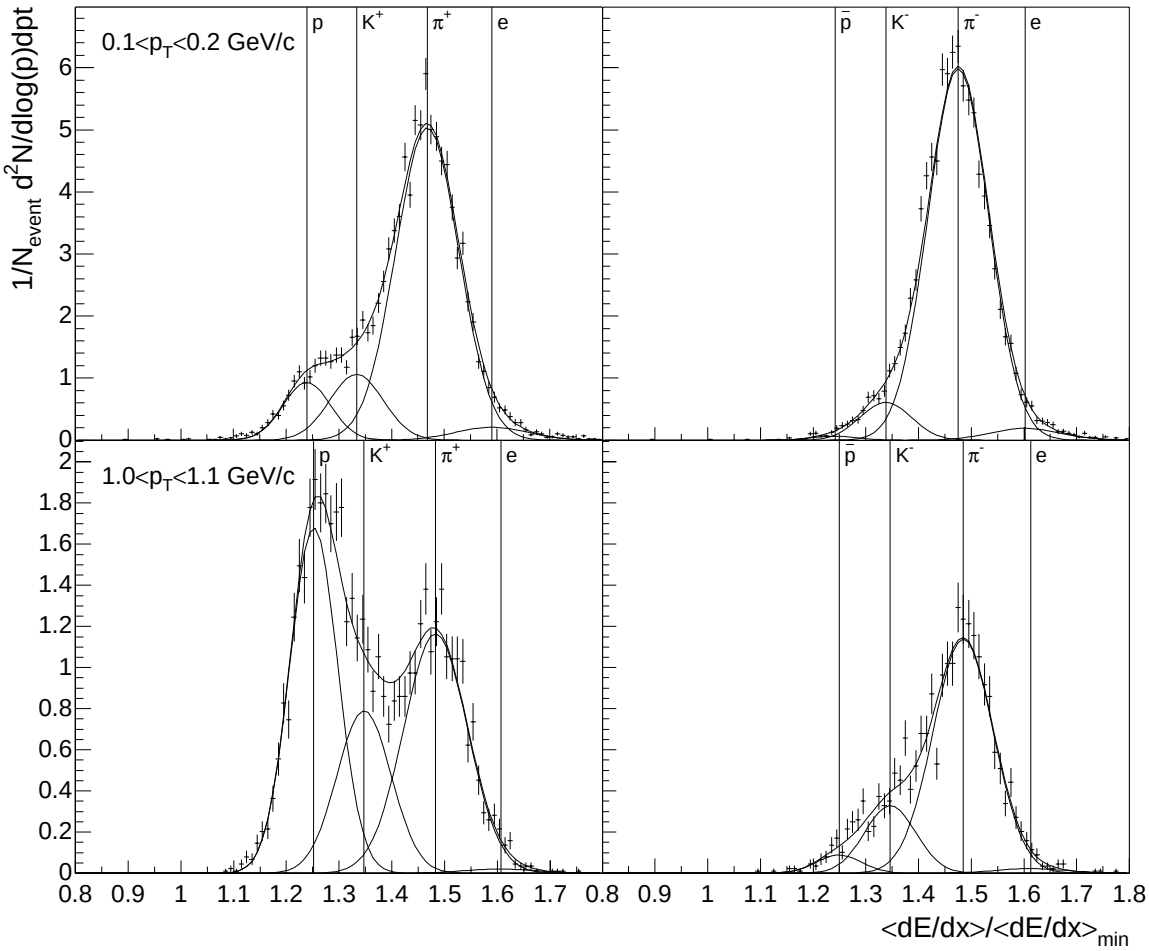

Figure 3.6: Example fits of the $\langle dE/dx \rangle$ distributions. All plots are for $3.1 \leq \log(p) < 3.3$ and for $|z\phi| < 54°$. The upper row is at low $p_\perp (0.1 \leq p_\perp < 0.2 \mathrm{GeV}/c)$ and the lower row is at high $p_\perp (1.1 \leq p_\perp < 1.1 \mathrm{GeV}/c)$. Left panels are for positively charged particles and right panels are for negatively charged particles.

the fraction of kaons which decay before reaching the upstream and downstream faces of the MTPC. The maximum correction of about 40% occurs for the kaons of lowest momentum.

For simulating the embedded tracks, the GEANT detector simulation code [GEA93] and a description of the detector geometry is used for tracking of particles through the NA49 apparatus. A code incorporating a parameterized response of the TPC's and TPC readout (MTSIM) is used for generating raw data from the tracking simulation. MTSIM was originally developed for the MTPC's [Toy99]. It has been extended for use in all NA49 TPC's. As discussed in more detail in Appendix D, MTSIM generates raw data which agree well with data from real events. This is a necessary condition to determine corrections with reasonable accuracy. The estimate of the uncertainty in these corrections is discussed in Section 3.7.

A strict definition of acceptance is imposed by considering the distribution of the number of clusters which embedded tracks from a small bin in $(p, p_\perp, \phi)$ deposit in the TPC active volume. If there are any tracks from this bin which leave fewer than a minimum number of clusters (see Table 3.1) in the TPC active volume, the entire bin is declared outside the acceptance and not used

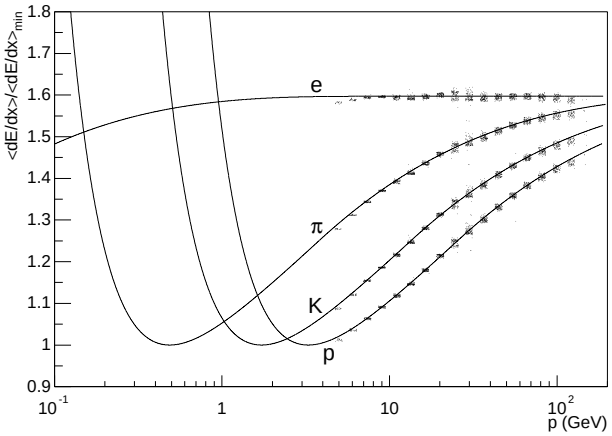

Figure 3.7: Fitted means from the $\langle dE/dx \rangle$ spectra

for further analysis. The acceptance fraction for a p-$p_\perp$ bin is the ratio of the number of accepted ϕ bins to the number of ϕ bins for the full azimuth. This acceptance definition is strict in the sense that bins which overlap with the edge of the TPC active volume are not used at all, which excludes some otherwise good tracks near the TPC edges. However, the p-$p_\perp$-ϕ bins utilized are small, and the resulting acceptance loss is less than one percent of the total detector acceptance.

For assessing tracking inefficiencies, simulated proton tracks were embedded. Tracking inefficiencies can arise because of physical cluster loss in the TPC's or readout, merging of close pairs of tracks into a single reconstructed track, mis-reconstruction of clusters and tracks by the raw data analysis software, and loss of tracks due to the imposed quality cuts. On the other hand, extra tracks may be found due to splitting of a single physical track into two or more reconstructed tracks. The simulation-embedding-reconstruction framework attempts to estimate all of these effects to obtain a single tracking efficiency value in each p-$p_\perp$-ϕ bin for each centrality sample. Figure 3.8 shows sample results from the efficiency calculation, along with geometrical acceptance, as a function of $p_\perp$ and at several fixed total momenta. The plots in the left column show results for identified particles and the plots in the right column show results for charged particles when particle identification is not considered. The steps in the acceptance results arise because of the finite ϕ bins. Efficiency calculations are shown for both the most central and most peripheral event samples. In certain kinematic regions, these calculations diverge from each other due to track density dependent reductions in the tracking efficiency.

The dominant backgrounds to the spectra come from the weak decay of strange particles into charged π and proton (and $\overline{\mathrm{p}}$). These charged decay products can produce tracks in the TPC's which, when reconstructed, appear to come from the Pb+Pb interaction point. Whether this occurs depends on their production and decay kinematics. The strange particles which contribute the bulk of the background are K^0_S to π and singly-strange baryons (Λ, Σ^+, Σ^0, Σ^-, and their anti-particles) to proton, $\overline{\mathrm{p}}$, and π. Multiply-strange baryons also contribute but to a significantly lesser extent due to their much lower yield.

In particular p-$p_\perp$ bins, this contamination can range up to about 50 percent of the measured proton yield and up to about 10 (5) percent of the measured $\pi^+(\pi^-)$. When integrated over $p_\perp$ at fixed y, the maximum contamination for protons occurs at mid-rapidity and is approximately 30 percent. The total relative contamination to π^+ and π^- does not depend as strongly on $p_\perp$ and the maximum contamination to the measured yield is also about 10 and 5 percent.

For assessing these decay backgrounds, simulated Λ and K^0_S and their decay products were

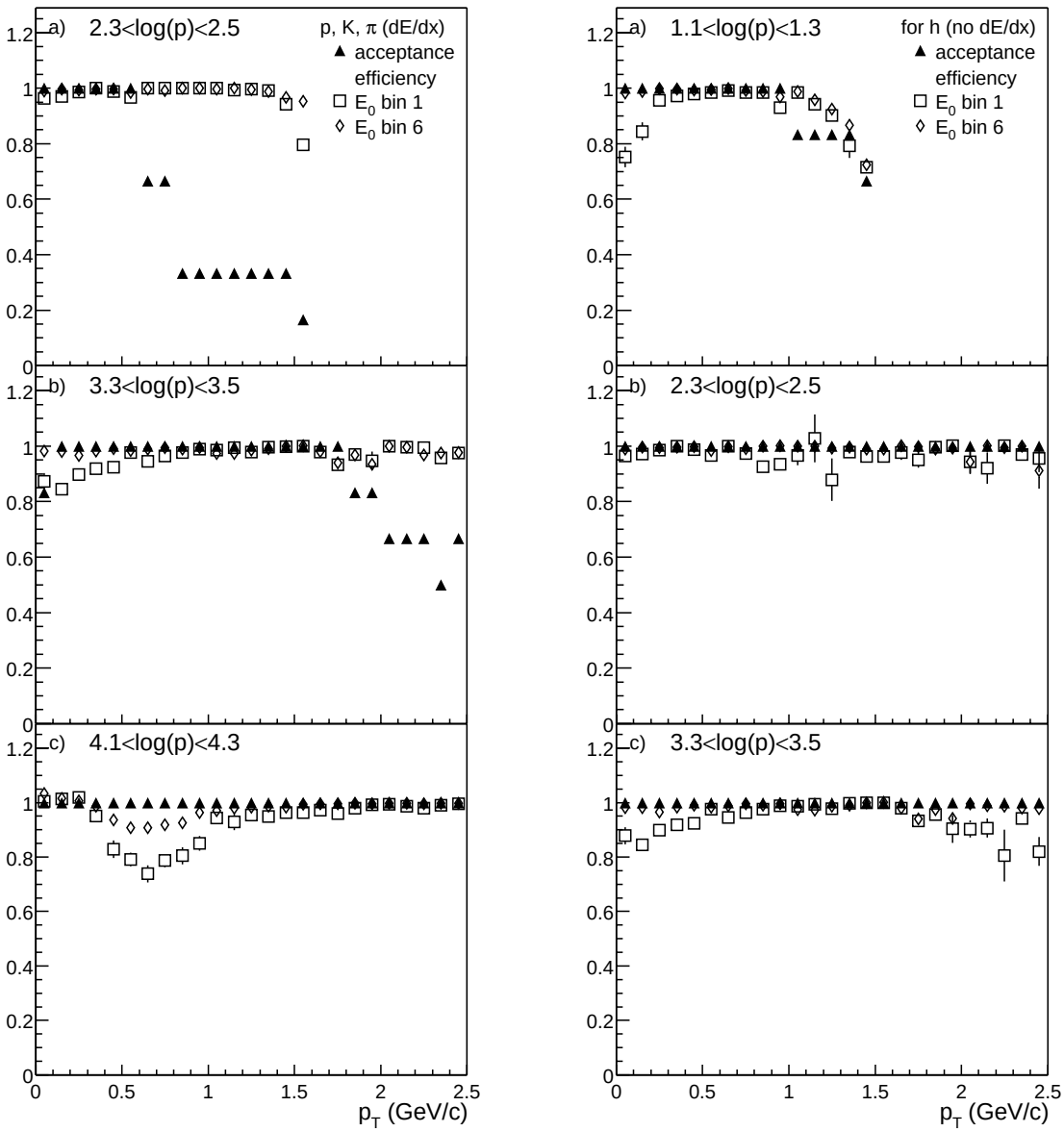

Figure 3.8: Sample acceptance and tracking efficiency corrections. The left column shows corrections for identified particles. The right column shows corrections for charged particles when particle identification by dE/dx is not considered. The corrections are shown as a function of $p_\perp$ and each plot is at a different fixed total momentum. The tracking efficiency is shown for both the most central (□) and most peripheral (◇) centrality samples.

embedded. Because Σ^0 decays rapidly to Λ, no separate simulation for Σ^0 is required. In principle, since Σ^+ and Σ^- are charged and would follow a different flight path from a Λ before decay and also decay with different lifetime, a separate simulation of these species should be performed. However, because of uncertainty about their distribution and yield and on the distribution of Λ itself, it was assumed that the background from these particles scales according the ratio of their relevant decay fraction to those for Λ. The Λ simulation is also used to estimate the background from $\overline{\Lambda}$ and other strange anti-baryons. In doing this, systematic effects are introduced due to the small differences in the tracking inefficiencies for positively and negatively charged tracks. However, this effect is insignificant in comparison to the systematic error assigned due the uncertainty in the $\overline{\Lambda}$ yield.

The actual distribution of Λ and K^0_S produced in these collisions is not known. In order to assess the magnitude of the corrections due to these backgrounds, a parent distribution which is uniform in y and $p_\perp$ was simulated. The decay correction for any parent distribution is then obtained by re-weighting the resulting reconstructed tracks by that y-$p_\perp$ distribution. The RQMD and VENUS event generators were used, along with constraints which the spectra measured in this thesis provide, to generate representative parent distributions. The measured spectra constrain the possible Λ and K^0_S distributions in two ways:

1. The integrated yield of K^0_S should be approximately equal to the average of the integrated yields of K^+ and K^-. The effect of the net isospin of Pb + Pb collisions on the ratio of charged to neutral kaon production should be small, and this is confirmed by preliminary NA49 data from central Pb + Pb collisions [Sik99].

2. The net strangeness carried by the charged kaons (which is given by the integrated yield of $K^+ - K^-$) should be proportional to the net strangeness carried by the strange baryons ($Y - \overline{Y}$). Given that the anti-hyperon yield is a small fraction of the hyperon yield, the integrated Λ yield should be approximately proportional to the yield of $K^+ - K^-$. RQMD and VENUS predict that this proportionality constant is about 0.7.

Sample results for the feed-down corrections are presented in Chapter 4 along with the final corrected results. For both the efficiency and background, the statistical errors on the corrections are estimated by dividing the sample of embedded tracks into thirds, calculating the corrections for each third in each p-$p_\perp$-ϕ bin, and determining the mean square deviation of the results.

3.6 Transformation to Final Spectra

The charged particle and identified spectra are determined in bins of $\log(p)$, $p_\perp$, and ϕ. An extrapolation to 2π is performed by averaging over the ϕ bins used and assuming azimuthal symmetry in the primary particle spectra. On an inclusive basis, where the event impact parameter occurs at random ϕ, this assumption must be valid.

In order to obtain spectra in the kinematic variables y or x_F and $p_\perp$ or $m_\perp$, the $\log(p)$-$p_\perp$ distributions are sampled in a grid in the kinematic variables with finer bins than the desired final spectra. These samples are weighted by the Jacobian of the transformation, which is given in Appendix B, and accumulated in histograms for the final spectra.

To obtain integrated longitudinal spectra, an extrapolation to high $p_\perp$ or $m_\perp$ must be made. This extrapolation is typically less than ten percent and is done by fitting the measured spectra in the small y or x_F bins and at high $p_\perp$ by

$$\frac{1}{p_\perp}\frac{dN}{dp_\perp} = Ae^{-m_\perp/T} \tag{3.4}$$

which, as discussed in Chapter 4, fits the spectra well beyond some minimum $p_\perp$.

3.7 Systematic Errors

The systematic errors in determining the particle distributions come from uncertainties in the fitting procedure used to extract particle yields from the dE/dx distributions, uncertainties in the quality of the tracking efficiency calculations, and poor knowledge of the parent distributions used for making the weak particle decay background corrections.

Because the total number of particles contributing to a given dE/dx distribution is fixed by the total number of entries in the distribution, systematic errors in the yields of each particle species due to errors in the fit are anti-correlated. This effect is particularly important for protons and K^+ (or $\overline{p}$ and K^-), where usually no clear separation of peaks is visible, and where the $K^{\pm}$ yields are used to scale the model-estimated hyperon distributions which provide the input to the proton feed-down estimates. The correlated fit errors are propagated through the analysis and reported in the final results.

From studying the variation in the corrected spectra as the track quality cuts are varied, it is estimated that the typical systematic error due to the simulation inaccuracies are on the order of 5 percent. In those regions where the tracking efficiency correction factors are large (greater than 20 percent), a systematic error of 10 percent is assumed.

The uncertainty in the parent hyperon distributions is estimated by considering the predictions from two different models, VENUS 4.12 and RQMD 2.3. After scaling the model predictions by the measured $K^+ - K^-$, the dN/dy of $\Lambda + \Sigma^0$ differs by up to 20 percent. The hyperon distributions are assumed to have a relative uncertainty of 20 percent. This uncertainty is augmented by the absolute difference between the scaled VENUS and RQMD distributions.

Chapter 4

Results and Discussion

4.1 Overview

The measured distributions and yields of unidentified and identified hadrons will be used to study baryon stopping, particle production, and the generation of transverse momentum as a function of centrality in Pb + Pb collisions at 158 GeV/nucleon. This study will show that more central collisions have a greater degree of stopping and harder transverse momentum distributions than peripheral collisions. These trends are consistent with those found by comparing central collisions of light nuclei with central collisions of heavy nuclei at the SPS [Ap+99, Toy99] and with centrality selected collisions at lower collision energies [Ah+99]. The yield of charged pions depends on the centrality of the collision, showing a slightly greater than linear dependence on the number of participating nucleons. In addition, only small changes in the momentum distributions of pions are observed.

In Section 4.2 the measured and derived distributions relevant for this discussion are presented. In Section 4.3, the net proton and net baryon rapidity distributions are interpreted in terms of stopping and compared to RQMD, VENUS, and HIJING/B predictions. In Section 4.4, the scaling of pion rapidity distributions and yields with centrality is studied. In Section 4.5, properties of the transverse distributions of the pions, kaons, and protons are interpreted in the context of random walk of the incident nucleons and radial flow of the produced system.

4.2 Measured and Derived Particle Distributions

Identified particle distributions are measured over the acceptance of the MTPC's, which extends from a laboratory momentum of 7 GeV/c to about 100 GeV/c, with no restriction on transverse momentum. The distributions are limited at high transverse momentum (typically between 1.5 and 2.0 GeV/c) by low statistics. For laboratory momenta between 4.5 and 7 GeV/c, the $p_\perp$ range of the measured distributions is limited by acceptance. When transformed into rapidity, this results in nearly full acceptance forward of mid-rapidity for protons, $\overline{\mathrm{p}}$, and $\mathrm{K}^{\pm}$. To determine the yield at fixed rapidity in this region, only a small extrapolation (nowhere larger than five percent) of the measured $p_\perp$ distributions to large $p_\perp$ is needed. Because these collisions are symmetric, the rapidity distributions can be reflected about mid-rapidity to obtain an estimate of the total yields.[1]

[1] Events are selected and segregated into centrality bins using measurements which depend only on the spectator portion of the *beam* nucleus. Since the same selection criteria are not imposed on the spectator portion of the *target* nucleus, a bias can be introduced. A study of this effect was performed using events produced with the VENUS 4.12 event generator. Introducing a sharp cut on number of beam nucleus spectators introduced less than 1% asymmetry in the inclusive dN/dy distributions from these events. Since the experimental trigger and E_0 measurement determine the number of spectators with finite precision, they should generate a smaller asymmetry.

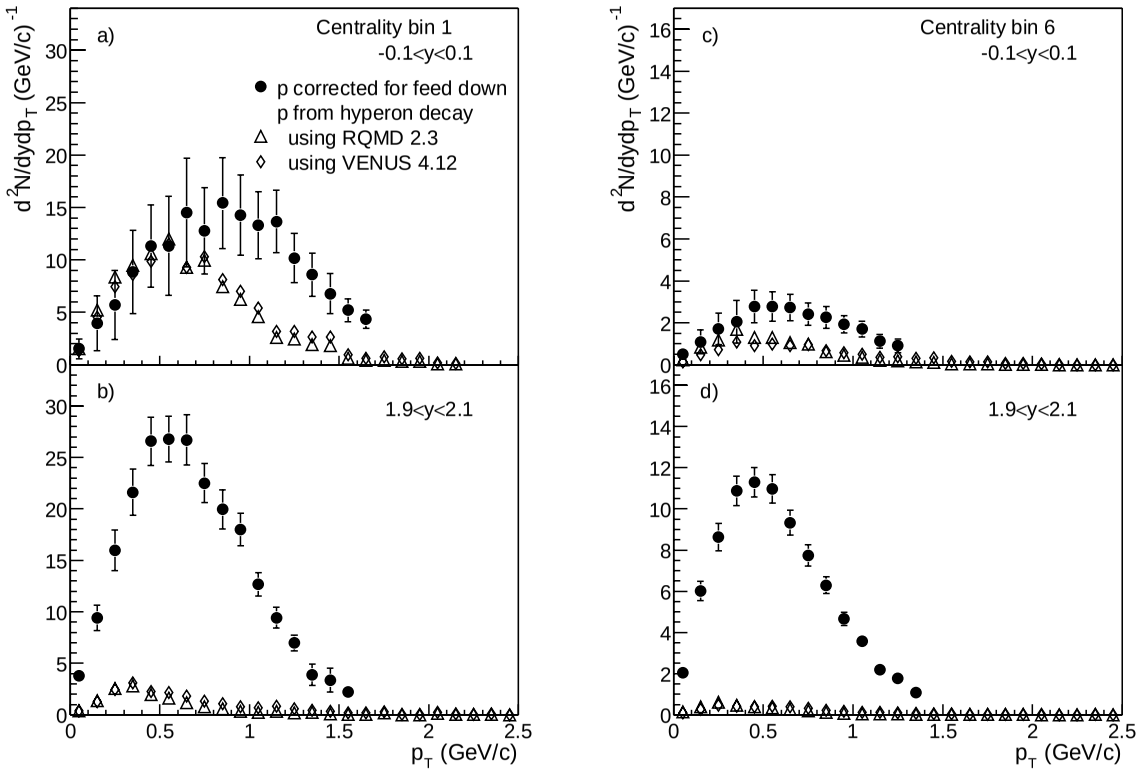

Figure 4.1: Proton $p_\perp$ distributions at fixed rapidity for two rapidity and two centrality bins. Each panel shows the corrected proton distribution along with the estimated corrections for the feed-down from the decay of hyperons. For comparison, the feed-down estimates from both RQMD ($\triangle$) and VENUS ($\diamond$) are shown. The left panels are for the most central collisions and the right panels are for the most peripheral collisions. Panels a) and c) are for mid-rapidity ($y = 0$) and panels b) and d) are for a forward rapidity ($y = 2.0$).

For $\pi^\pm$, acceptance at low $p_\perp$ extends from beam rapidity to only about one unit above mid-rapidity. However, unidentified charged hadrons are measured over the larger acceptance of the full NA49 TPC system, which extends down to 0.5 GeV/c laboratory momentum. This is equivalent to a π rapidity of -1. To obtain an estimate of the $\pi^\pm$ distributions over the full acceptance for unidentified charged hadrons, the measured y-$p_\perp$ distributions of $h^\pm$ can be corrected for the contamination from $K^\pm$ and protons or $\overline{p}$ by reflecting the measured distributions, in order to obtain an estimate of the $\pi^\pm$ rapidity and $p_\perp$ distributions. Since the π yield dominates except at large $p_\perp$ and at the largest laboratory longitudinal momenta, this method works reasonably well.

4.2.1 Transverse Distributions

Figure 4.1 shows the fully corrected $p_\perp$ distributions for protons for the most central and most peripheral centrality bins at mid-rapidity ($y = 0$) and at a forward rapidity ($y = 2.0$). Also shown as open symbols are the feed-down corrections applied for decay of hyperons to protons. For comparison, the corrections obtained from the RQMD and VENUS models are both shown. As noted in Chapter 3, the RQMD calculation is used as the default correction and the difference between the two models is used to assist in estimating the systematic error of this correction. At

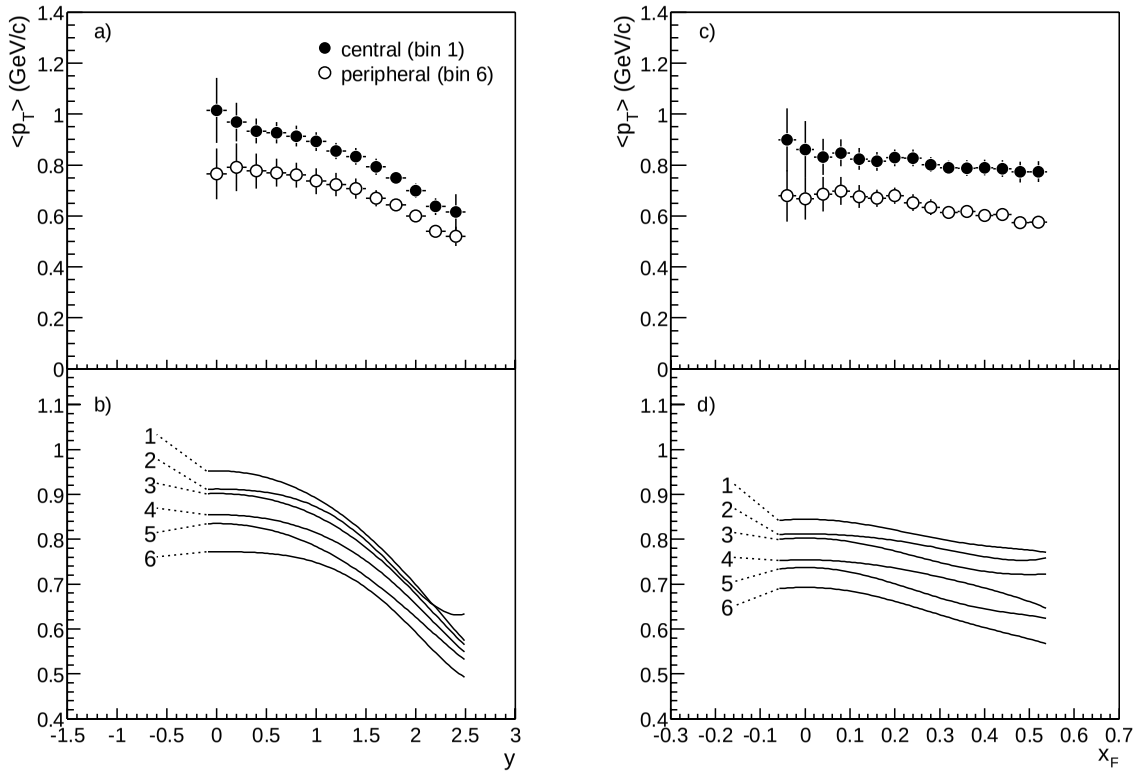

Figure 4.2: $\langle p_\perp \rangle$ of protons as a function of rapidity (left panels) and as a function of x_F (right panels). The upper panels show individual data points for the most central and most peripheral event samples. The error bars shown include both statistical and systematic errors and indicate typical errors for all centrality bins. The lower plots show smoothed curves for centrality bin 1 (most central) to bin 6 (most peripheral). The lower plots have an expanded scale and suppressed zero.

mid-rapidity and low $p_\perp$, the correction is approximately equal to the corrected proton yield and the uncertainty of this correction dominates the estimated systematic error for the proton yield in this kinematic region. At higher $p_\perp$and higher total momentum, the relative correction is smaller. The quoted errors on the result include the uncertainties in particle identification, feed-down corrections, and corrections for tracking efficiency and acceptance.

The upper panels of Figure 4.2 show the mean transverse momentum ($\langle p_\perp \rangle$) of protons as a function of rapidity (a) and as a function of x_F (b) for the most central and most peripheral bins. The $p_\perp$ spectrum of the central collisions is harder than the corresponding $p_\perp$ spectrum of the peripheral collisions at all rapidity or x_F. $\langle p_\perp \rangle$ is a maximum at mid-rapidity and decreases toward projectile rapidity. This is primarily an effect of momentum conservation, as high rapidity protons are limited to low $p_\perp$ so that the total momentum of interacted protons is limited to be below the beam nucleon momentum. The lower panels of Figure 4.2 show $\langle p_\perp \rangle$ for all six centrality bins as smoothed curves with the error bars of the individual data points suppressed. The curves show that, at all y or x_F, $\langle p_\perp \rangle$ increases with increasing centrality.

Figure 4.3 shows the procedure for determining the π^+ $p_\perp$ distribution from the measured h^+ distribution and the reflected proton and K^+ distributions, carried out for the distributions from the most central event sample. The left panels show the distribution at mid-rapidity for π, where

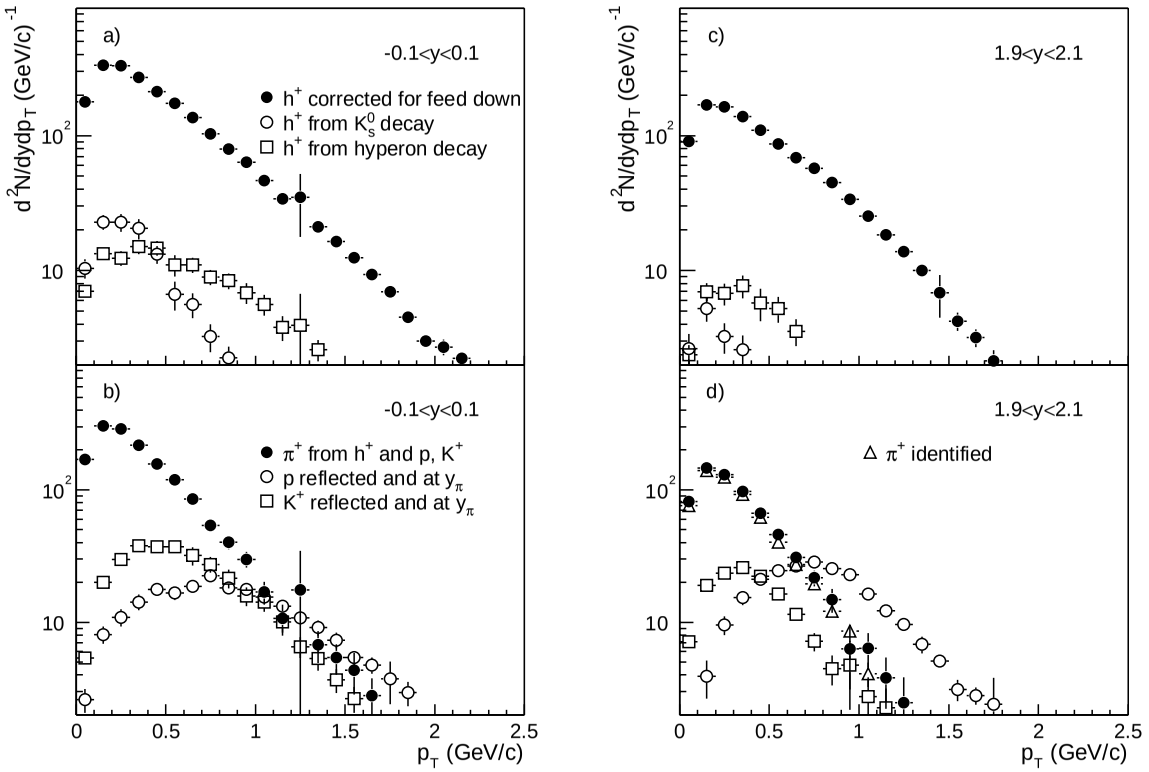

Figure 4.3: Determining π $p_\perp$ distributions from h, proton, and K distributions. As described in the text, these plots show how the π^+ distributions are obtained from the measured h^+, proton, and K^+ distributions and the estimated feed-down corrections. All distributions are for central events. The left panels are at mid-rapidity ($y = 0$) and the right panels are at a forward rapidity ($y = 2.0$). For comparison, panel d) also shows the measured π^+ distribution, which can be obtained directly by dE/dx in this kinematic region.

only the yield of unidentified, charged hadrons ($h^\pm$) were determined. Panel a) shows the corrected h^+ $p_\perp$ distribution and the corrections applied to h^+ for decay of K^0_S and hyperons. Panel b) shows the estimate of proton and K^+ contributions to the corrected h^+ distribution. These estimates were obtained by reflecting the proton and K^+ y-$p_\perp$ distributions measured forward of mid-rapidity and transforming them into distributions as a function of pion rapidity and $p_\perp$. Panel b) also shows the π^+ distribution resulting from subtracting these proton and K^+ estimates from the h^+ distribution in panel a).

The right panel of Figure 4.3 shows the application of the same procedure at a forward rapidity ($y = 2$). In this kinematic region, π^+ identified via dE/dx are also measured and these are shown in panel d). Here the identified π^+ yields are below the yields estimated from h^+ by about 5 percent. This difference is due to contamination of h^+ by conversion electrons. This contamination is removed by the full dE/dx fit used to obtain π^+ and is also removed from h^+ at lower momenta where good separation exists between the π and electron dE/dx peaks. In this kinematic region, however, the peaks are too close for a cut to be useful and the electron contamination to h^+ is not removed. Given this contamination, the π^+ distribution obtained from h^+ agrees well with the directly measured π^+ distribution.

While at both mid-rapidity and forward rapidities the yield of π^+ is larger than that of

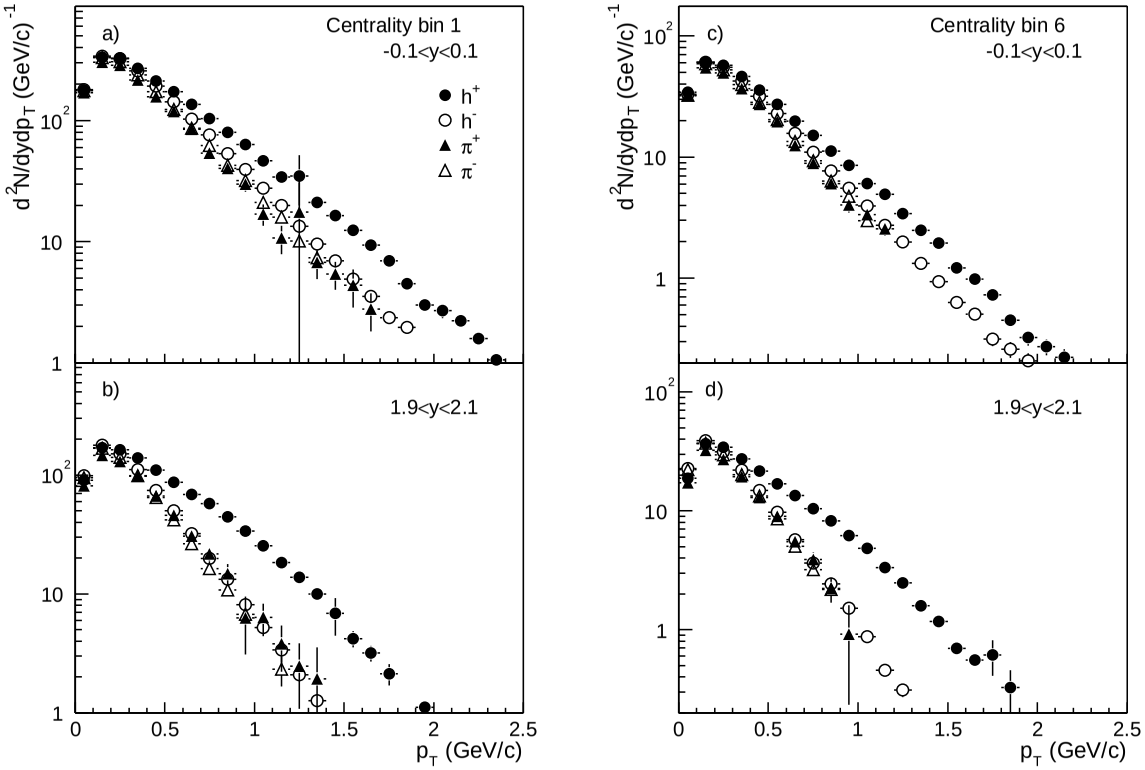

Figure 4.4: Sample $h^{\pm}$ and $\pi^{\pm}$ $p_{\perp}$ distributions. Each panel shows the corrected h^+, h^-, π^+, and π^- $p_{\perp}$ distributions for a single rapidity and centrality bin. The upper panels are at mid-rapidity ($y = 0$) and the lower panels are at a forward rapidity ($y = 2.0$). The left panels are for the most central event sample and the right panels are for the most peripheral event sample. The high $p_{\perp}$ enhancement of h^+ over π^+ is due to the addition of the harder proton and K^+ distributions. The difference between h^- and π^- is smaller because of the lower relative yields of K^- and $\overline{p}$.

K^+ and protons, the $p_{\perp}$ distributions of K^+ and protons are harder than π^+. This gives the h^+ $p_{\perp}$ distributions a high $p_{\perp}$ tail which is substantially reduced in the π^+ distributions by making the K^+ and proton subtractions. While not shown, this effect is also present in the determination of π^- from h^-, K^-, and $\overline{p}$ but to a lesser extent because of the lower yields of K^- and $\overline{p}$ relative to the π^- yield.

Figure 4.4 shows the corrected $p_{\perp}$ distributions for $h^{\pm}$ and $\pi^{\pm}$ for the most central and most peripheral event samples at mid-rapidity and at a forward rapidity ($y = 2.0$). While all of these distributions show an excess of h^+ over h^- at nearly all $p_{\perp}$ due to the excess of K^+ and protons over K^- and $\overline{p}$, they also show a smaller excess of π^- over π^+. This is primarily a reflection of the net negative isospin of the colliding system. As discussed in Appendix E, model calculations show that the bulk of this net isospin is transferred from the incoming nucleons to pions, which can occur through production and decay of Δ, N^*, and higher resonances.

The upper panels of Figure 4.5 show $\langle p_{\perp} \rangle$ of π^+ as a function of (a) rapidity and (b) x_F for the most central and most peripheral bins. While the effect is not as marked as was shown for protons, the $\langle p_{\perp} \rangle$ of π^+ produced in central collisions is larger at all rapidities or x_F than that produced in peripheral collisions. For π, the kinematic effect which limits $\langle p_{\perp} \rangle$ at large rapidities is also present but smaller since at fixed large rapidity and moderate $p_{\perp}$ (in comparison to their $\langle p_{\perp} \rangle$),

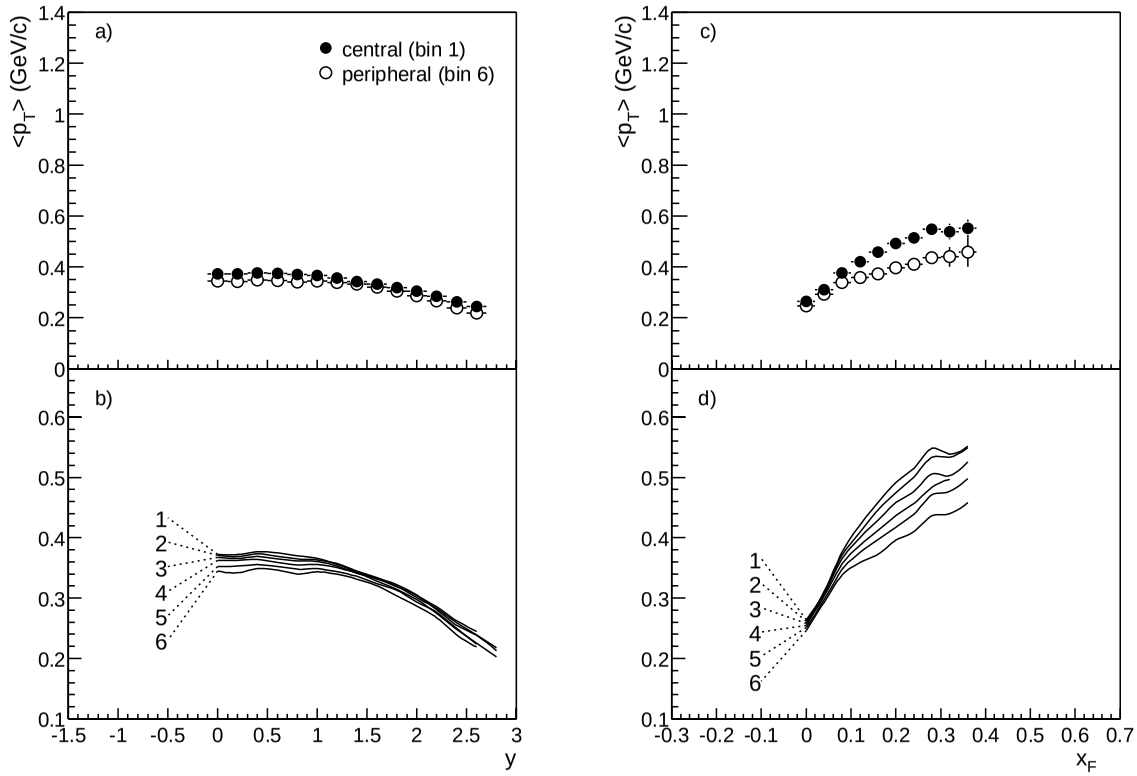

Figure 4.5: $\langle p_\perp \rangle$ of π^- as a function of rapidity (left panels) and as a function of x_F (right panels). The upper panels show individual data points for the most central and most peripheral event samples. The error bars shown include both statistical and systematic errors and indicate typical errors for centrality bin 1 (most central) to bin 6 (most peripheral). The lower plots have an expanded scale and suppressed zero.

protons have a larger total momentum than π. As a function of x_F, the distributions show the well-known "seagull" effect [Mor72], which refers to the larger $\langle p_\perp \rangle$ observed for particles produced with larger center-of-mass longitudinal momentum. It is thought that this correlation between transverse and longitudinal momentum is due to a combination of phase space constraints and resonance decay. The lower panels of Figure 4.5 show $\langle p_\perp \rangle$ for all six centrality bins as smoothed curves with the error bars of the individual data points suppressed. Again like protons, the π^+ distributions show that at all rapidities or x_F, $\langle p_\perp \rangle$ increases with increasing centrality, although the effect is smaller.

4.2.2 Rapidity Distributions

As discussed in Section 3.6, rapidity distributions are obtained by integrating $p_\perp$ distributions measured at fixed rapidity and extrapolating to high $p_\perp$ with a fit to equation 3.4 of the high $p_\perp$ data points. In no case does this extrapolation exceed 5% of the integral of the measured data and is added with an assumed 50% relative error.

Figure 4.6 shows the rapidity distributions for protons and $\overline{\mathrm{p}}$. The upper panels show the fully corrected distributions for the central events along with the correction that is applied for decay of hyperons into protons or $\overline{\mathrm{p}}$. For protons, the measured data extend below mid-rapidity. Because of the symmetry of the colliding system, the corrected proton spectra should also be symmetric

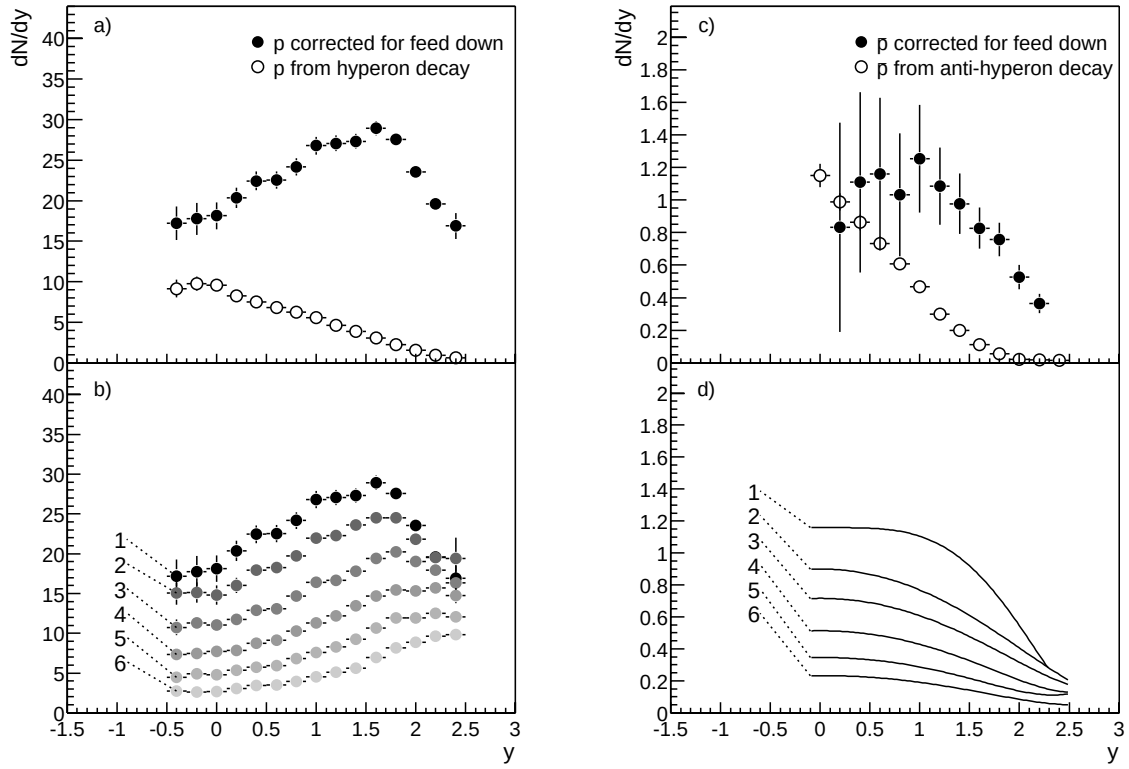

Figure 4.6: Proton (left panels) and $\overline{\mathrm{p}}$ (right panels) y distributions. The upper panels show the fully corrected distribution for the most central event sample along with the correction that was applied for feed-down from hyperon and anti-hyperon decay. The lower panels show the corrected distributions for all six centrality bins (1–6). The $\overline{\mathrm{p}}$ distributions are represented by polynomials symmetric about $y = 0$ which were fitted to the data points. The error bars shown include both statistical and systematic errors.

about mid-rapidity. The fact that the final spectra are not symmetric is primarily a result of the systematic uncertainty in the correction for feed-down from hyperon decay. Although the hyperon distributions assumed for estimating the correction are symmetric about mid-rapidity, the resulting distribution of feed-down protons is not symmetric because lower momentum hyperons decay closer to the Pb+Pb interaction point and the resulting decay protons have a greater probability of having a trajectory consistent with that of a primary proton. The same effect may also be the cause for the apparent dip in the yield of $\overline{\mathrm{p}}$ at mid-rapidity. In this case, the estimate of the ratio of primary anti-hyperon to primary $\overline{\mathrm{p}}$ yield is larger than one and systematic uncertainty in the primary anti-hyperon distribution results in a large systematic uncertainty in the corrected $\overline{\mathrm{p}}$ distributions. Since the $\overline{\mathrm{p}}$ distributions will only be used in combination with the proton distributions to measure $\mathrm{p} - \overline{\mathrm{p}}$, and the yield of $\overline{\mathrm{p}}$ is small compared to protons, this large systematic uncertainty does not significantly degrade the net proton and net baryon results to be presented.

The lower panels show the rapidity distributions for all centrality bins. For $\overline{\mathrm{p}}$, these distributions are shown as smoothed curves with the error bars of the individual data points suppressed. As will be discussed more fully in Section 4.3, the proton spectra show a shift in the maximum yield from near beam rapidity for peripheral collisions toward mid-rapidity for more central collisions. Within the systematic uncertainty of the $\overline{\mathrm{p}}$ distributions, no change in shape is indicated while the

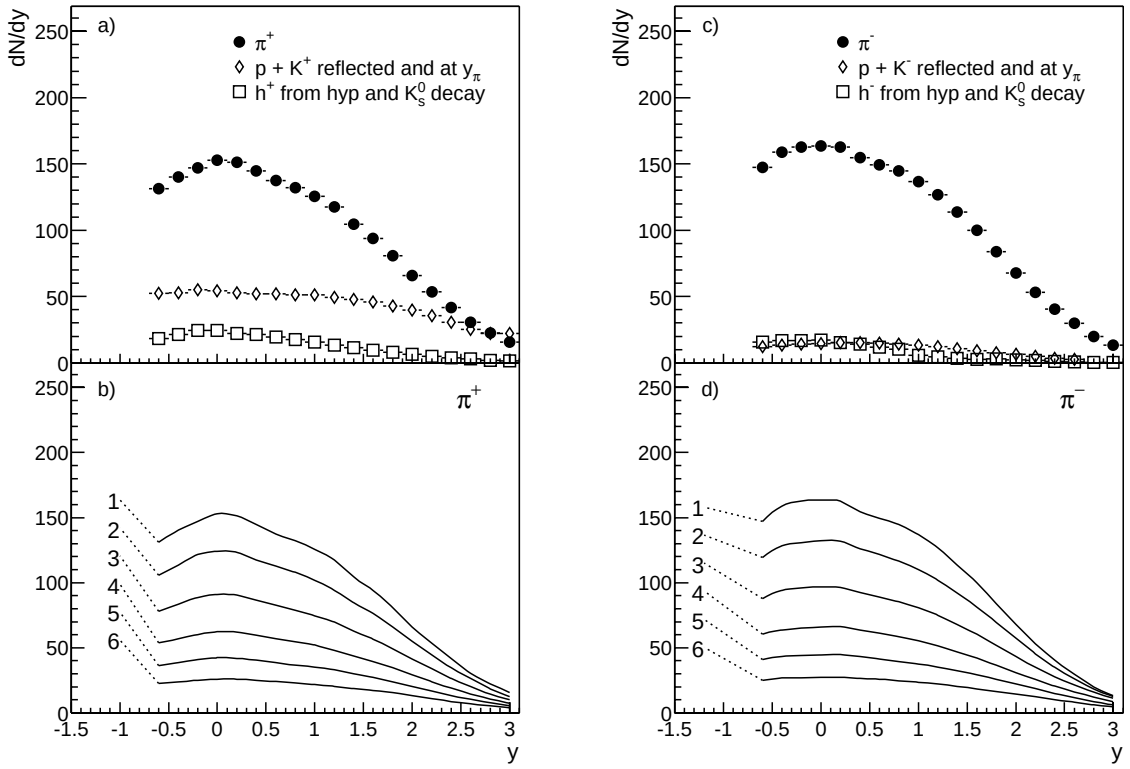

Figure 4.7: π^+ (left panels) and π^- (right panels) rapidity distributions. The upper plot shows the rapidity distributions for the most central data sample. These distributions were obtained from $h^\pm$ by correcting for the measured proton, $\overline{\mathrm{p}}$, and $\mathrm{K}^\pm$ distributions as discussed in the text. The proton, $\overline{\mathrm{p}}$, and $\mathrm{K}^\pm$ distributions and the corrections applied for the feed-down from the decay of K^0_S and hyperons are also shown. The lower panels show the corrected distributions for all six centrality bins (1–6) as smooth curves through the data points with the error bars suppressed.

yield increases from peripheral to central collisions.

Figure 4.7 shows the rapidity distributions of π^+ (left panels) and π^- (right panels) determined from the $h^\pm$ distributions and subtraction of the $\mathrm{K}^\pm$, proton, and $\overline{\mathrm{p}}$ distributions as discussed in Section 4.2.1 for the $p_\perp$ distributions. The upper panels show the π^+ and π^- distributions for central collisions along with the corrections that were applied for feed-down from K^0_S and hyperons and the $\mathrm{K}^\pm$, proton, and $\overline{\mathrm{p}}$ subtractions. Except at forward rapidities for the π^+, the relative magnitude of the corrections is small. The lower panels show the $\pi^\pm$ rapidity distributions for all centrality bins as smoothed curves with the error bars of the individual data points suppressed. Unlike protons, these distributions show no obvious change in shape in going from peripheral to central collisions. The yield increases with centrality. How the shapes and yield scale with the centrality measures will be discussed quantitatively in Section 4.4.

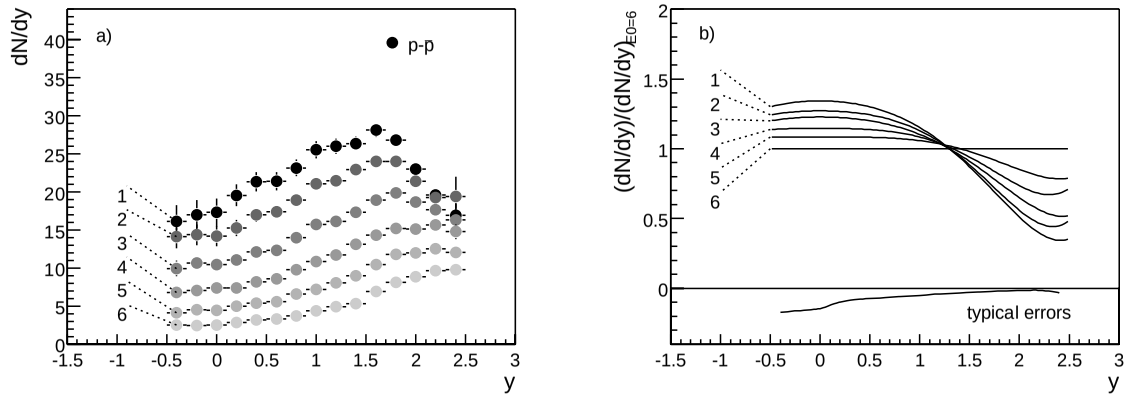

Figure 4.8: $p - \overline{p}$ y distributions for the six centrality samples. The left panel shows the absolute yield. For the right panel, the data in each centrality sample (1–6) are normalized by the number of participating nucleons and divided by the distribution in the most peripheral sample. The resulting distributions were fit to polynomials symmetric about mid-rapidity. The magnitude of the typical systematic errors is shown below the horizontal axis.

4.3 Baryon Stopping

4.3.1 Net Proton Distributions

As discussed in Section 1.3, stopping is studied with *net* particle distributions to remove the effect of particle/anti-particle pair production. The left panel of Figure 4.8 shows the rapidity distributions of net protons ($p - \overline{p}$) for each of the six centrality bins. These distributions are not very different from the proton rapidity distributions since the ratio of yields of $\overline{p}$ to protons, which is largest at mid-rapidity, is nowhere larger than about 0.1. Firstly, these distributions show an increasing yield of $p - \overline{p}$ in going from peripheral to central collisions. This reflects the increasing volume of the overlap region of the two colliding nuclei and the resulting increase in the number of nucleons participating in the reactions. This effect has been removed in the right panel of Figure 4.8, in which the data points at each rapidity have been normalized by their integral and divided by the corresponding data points in the most peripheral bin. The data are shown as smoothed curves with the error bars of the individual data points suppressed. These curves show that the relative yield of $p - \overline{p}$ near beam rapidity is strongly suppressed in central collisions relative to that in peripheral collisions. At $y = 2.5$, $dN/dy|^{norm}_{\mathrm{E_0\ bin\ 1}} = (0.4 \pm 0.1)\ dN/dy|^{norm}_{\mathrm{E_0\ bin\ 6}}$. On the other hand, the relative yield at mid-rapidity is enhanced in central collisions. Here, $dN/dy|^{norm}_{\mathrm{E_0\ bin\ 1}} = (1.38 \pm 0.15)\ dN/dy|^{norm}_{\mathrm{E_0\ bin\ 6}}$. The centrality bins between peripheral and central collisions show a smooth variation between these two extremes.

As noted in Chapter 1, the $p-\overline{p}$ rapidity distribution was previously measured and reported in [Ap+99]. Those results were obtained using a method for fitting the dE/dx distributions that did not separate the proton and K contributions. Instead, a correction to the $p - \overline{p}$ result was made using unpublished measurements of K^+ and K^- obtained by reconstructing K decays. These unpublished kaon results had poor phase space coverage and large systematic error, which resulted, in comparison to the results presented in this thesis, in a 30 percent overestimate of the $p - \overline{p}$ yield for $y < 1.5$.

Figure 4.9 compares the $p - \overline{p}$ distributions in the central and peripheral bins, normalized by the number of participating nucleon pairs to the equivalent nucleon-nucleon collision system. This system, called here $N_{Pb} + N_{Pb}$, is an average of $p + p$, $p + n$, and $n + n$ collisions which corresponds

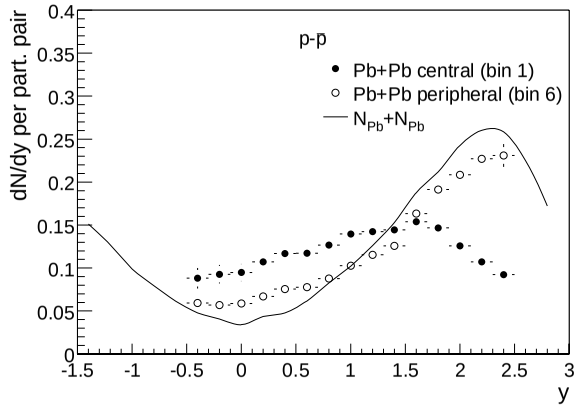

Figure 4.9: $\mathrm{p}-\overline{\mathrm{p}}$ y distributions for the most central and most peripheral centrality samples compared to the $\mathrm{N_{Pb}} + \mathrm{N_{Pb}}$ system, which is the isospin averaged nucleon-nucleon system appropriate for comparison to $\mathrm{Pb} + \mathrm{Pb}$ (see text and Appendix E).

to the isospin content of Pb + Pb collisions. This average was made using the RQMD model as described in Appendix E. Figure 4.9 shows that the $\mathrm{p} - \overline{\mathrm{p}}$ yield for $\mathrm{N_{Pb}} + \mathrm{N_{Pb}}$ is even smaller at mid-rapidity and more strongly peaked toward beam rapidity than for peripheral collisions.

4.3.2 Net Baryon Distributions

An estimate of the net baryon ($\mathrm{B} - \overline{\mathrm{B}}$) distributions can be made using the procedure described in Section 3.3 for estimating the number of interacting nucleons along with the procedure described in Section 3.5 for estimating the rapidity distributions of the hyperons. Then equation 3.1 becomes

$$\frac{dN_{\mathrm{B}-\overline{\mathrm{B}}}}{dy} = (2 + \alpha(y))\frac{dN_{\mathrm{p}-\overline{\mathrm{p}}}}{dy} + \gamma\frac{dN_{\mathrm{Y}-\overline{\mathrm{Y}}}}{dy}, \tag{4.1}$$

where $1 + \alpha(y)$ is the rapidity dependent ratio between the yield of $\mathrm{n} - \overline{\mathrm{n}}$ and $\mathrm{p} - \overline{\mathrm{p}}$, γ is the ratio of $\mathrm{K}^+ - \mathrm{K}^-$ found in $\mathrm{Pb} + \mathrm{Pb}$ collisions to that from the model, and $dN_{\mathrm{Y}-\overline{\mathrm{Y}}}/dy$ is from the model. Because model distributions of $\mathrm{Y} - \overline{\mathrm{Y}}$ are used to determine the corrections to the proton and $\overline{\mathrm{p}}$ distributions for feed-down from hyperon decay, and these distributions are added back in estimating $\mathrm{B}-\overline{\mathrm{B}}$, the uncertainty in the model estimates of the hyperon distributions partially cancels in $\mathrm{B}-\overline{\mathrm{B}}$. This is demonstrated more fully in Appendix E.

The left panel of Figure 4.10 shows the estimated rapidity distributions of $\mathrm{B} - \overline{\mathrm{B}}$ for each of the six centrality bins. The right panel of Figure 4.10 shown the same distributions normalized by their integral and divided by the corresponding $\mathrm{B} - \overline{\mathrm{B}}$ data points in the most peripheral bin. Like $\mathrm{p} - \overline{\mathrm{p}}$, the distributions show a suppression of the net baryon yield at forward rapidities and an enhancement at mid-rapidity, when comparing more central to more peripheral collisions. Figure 4.11 shows the distributions of $\mathrm{B} - \overline{\mathrm{B}}$ for the most central, most peripheral and estimated $\mathrm{N_{Pb}} + \mathrm{N_{Pb}}$ collision system, normalized by the number of participating nucleon pairs.

4.3.3 Stopping and Energy Loss

Baryon stopping depends on the colliding thickness of nuclear matter. In more peripheral collisions, most of the participating nucleons intersect the surface region of the opposing nucleus. In central collisions, a significant fraction of the nucleons pass through the central region of the opposing nucleus, where their trajectories can intersect many nucleons. In both cases, however, the

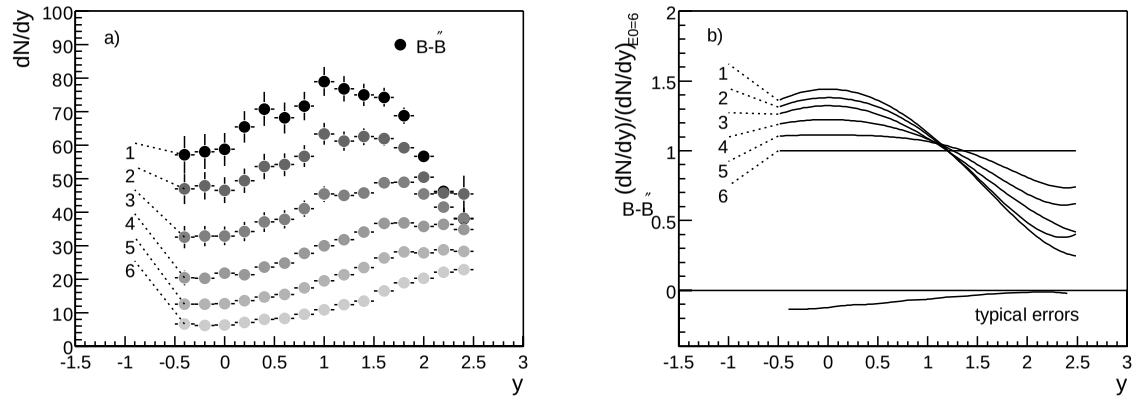

Figure 4.10: $B - \overline{B}$ y distributions for the six centrality samples (1–6). $B - \overline{B}$ were obtained by extrapolating the measured $p - \overline{p}$ distributions using model estimates of the $n - \overline{n}$ and $Y - \overline{Y}$ distributions (see text and Appendix E). The left panel shows the absolute yield. For the right panel, the data in each centrality sample are normalized by by the number of participating nucleons and divided by the distribution in the most peripheral sample. The resulting distributions were fit to polynomials symmetric about mid-rapidity. The magnitude of the typical systematic errors is shown below the horizontal axis.

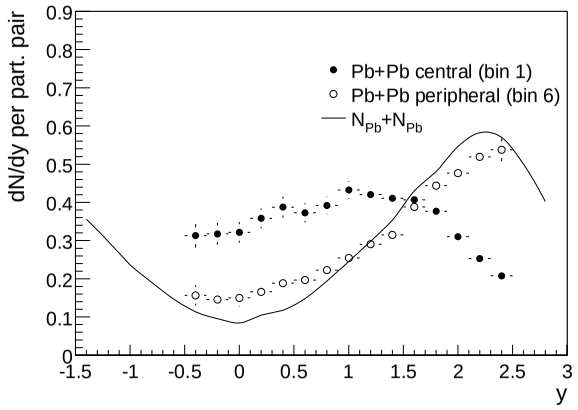

Figure 4.11: $B - \overline{B}$ y distributions for the most central and most peripheral centrality samples compared to nucleon-nucleon collisions, which is estimated from data on $p + p$ collisions and model calculations (see text and Appendix E).

distribution in nuclear thickness that the participating nucleons see is broad. This is shown in Figure 4.12, which is an estimate of the distribution of the number of collisions which the participating nucleons of one nucleus have with the nucleons of the other nucleus[2]. Because these distributions are broad, the distribution in stopping can be broad also.

Stopping can be characterized quantitatively by both the rapidity shift and energy loss of the nucleons. In making these calculations from the produced particle spectra, it is not possible to distinguish those nucleons that have been decelerated from the projectile to just above mid-rapidity

[2] For this estimate, the participating nucleons were assumed to follow straight trajectories through the other nucleus and interact with a cross section of 30 mbarn. Details of the calculation are given in Appendix E.

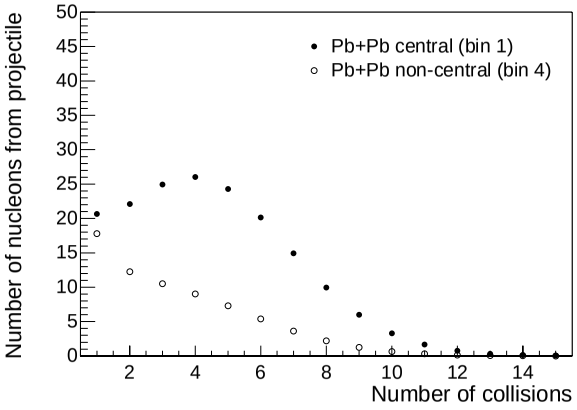

Figure 4.12: Glauber model calculation of the distribution of nucleon collision number for two centrality samples. This figure shows the mean number of nucleons (vertical axis) from one of two colliding nuclei which suffer a given number of collisions (horizontal axis) according to a Glauber model of nuclear collisions. The calculation is made at fixed collision impact parameter. The results shown are averaged over the estimated impact parameter distribution of each event sample. For this calculation, a nucleon-nucleon cross section of 30 mbarn was used.

from those originating from the target nucleus which are more strongly accelerated through mid-rapidity into the projectile hemisphere. Not accounting for baryons which have crossed mid-rapidity results in an underestimate of stopping.

Total energy loss of the participating nucleons is not well measured by NA49 because of the lack of acceptance of the MTPC's above about one half of the laboratory beam momentum. Differences in the number and distribution of nucleons in this momentum region strongly affect the calculated total nucleon energy loss. Additionally, at the high momentum limit, the $p - \overline{p}$ and $B - \overline{B}$ distributions fall most rapidly with increasing momentum for central collisions, so that the fraction of the initial energy carried by the unobserved protons above the acceptance limit is larger for peripheral collisions than for central collisions. As a result, the difference in average energy loss between central and peripheral collisions is underestimated.

In spite of these limitations, calculations of the rapidity shift and energy loss provide useful measures for comparing different collision systems. Table 4.1 shows the mean and root mean square deviation of the rapidity shift of $p - \overline{p}$ and $B - \overline{B}$ for each of the six centrality bins and the $N_{Pb} + N_{Pb}$ collision system. The calculation is over the forward hemisphere up to the acceptance limit of $y = 2.5$. In the most peripheral bin, the mean rapidity shift is enhanced 12–14% over that for $N_{Pb} + N_{Pb}$. This enhancement increases further for more central collisions, and the enhancement for central collisions is 41–43%. The root mean square deviation of the rapidity shift also increases in $Pb + Pb$ collisions over that in $N_{Pb} + N_{Pb}$. However, it does not increase with increasing collision centrality. This indicates that the spread in rapidity loss is dominated by the spread in nuclear thickness with which the participating nucleons interact and not by fluctuations in the degree of stopping which nucleons traversing similar nuclear thicknesses suffer. Numerical results from the Glauber calculations shown in Figure 4.12 are tabulated in the rightmost columns of Table 4.1. These show that while the mean number of nucleons with which the participating nucleons collide increases with centrality, the dispersion is large and nearly independent of centrality.

Table 4.2 shows the mean and root mean square deviation of the center-of-mass energy loss of $p - \overline{p}$ and $B - \overline{B}$ for each of the six centrality bins and the $N_{Pb} + N_{Pb}$ collision system. This energy loss is expressed as a fraction of the per nucleon initial beam kinetic energy (also calculated in the center-of-mass) since the energy associated with the incoming nucleon masses cannot be "lost" (the

	rapidity shift				ν	
	$p-\overline{p}$		$B-\overline{B}$			
E_0 bin	mean	rms	mean	rms	mean	rms
1	1.589±0.012	0.699±0.010	1.674±0.012	0.693±0.011	4.5	2.5
2	1.532±0.015	0.711±0.011	1.614±0.014	0.711±0.012	4.2	2.5
3	1.482±0.010	0.711±0.011	1.554±0.012	0.717±0.011	3.9	2.5
4	1.420±0.010	0.715±0.008	1.478±0.012	0.721±0.010	3.5	2.3
5	1.359±0.011	0.707±0.009	1.407±0.013	0.714±0.010	3.0	2.1
6	1.278±0.011	0.700±0.009	1.303±0.015	0.705±0.011	2.2	1.9
$N_{Pb}+N_{Pb}$	1.117±0.003	0.632±0.002	1.196±0.003	0.638±0.002	1	0

Table 4.1: Proton and baryon rapidity loss. The mean projectile rapidity loss ($\langle -\Delta y \rangle$) from beam rapidity ($y = 2.81$) is calculated for $p-\overline{p}$ and $B-\overline{B}$ over $0 < y < 2.5$. The dispersion ($\left\langle (y - \langle y \rangle)^2 \right\rangle^{1/2}$) calculated over the same range is also shown. The rightmost columns show the mean and dispersion of the number of collisions which the participating nucleons suffer. The bottom row shows the RQMD 2.3 calculations for the $N_{Pb} + N_{Pb}$ system.

	energy loss (%)			
	$p-\overline{p}$		$B-\overline{B}$	
E_0 bin	mean	rms	mean	rms
1	72.5±0.4	21.8±0.2	75.4±0.4	21.1±0.2
2	71.6±0.4	22.2±0.2	74.1±0.5	21.9±0.2
3	70.0±0.4	22.8±0.1	72.2±0.5	22.7±0.1
4	68.8±0.3	22.9±0.1	70.5±0.4	23.0±0.1
5	67.7±0.3	23.0±0.2	69.0±0.4	23.2±0.2
6	66.1±0.3	22.5±0.2	66.7±0.3	22.8±0.2
$N_{Pb}+N_{Pb}$	67.8±4.9	21.0±4.8	68.4±3.2	20.9±3.2

Table 4.2: Proton and baryon energy loss. The mean loss of kinetic energy of nucleons is calculated for $p-\overline{p}$ and $B-\overline{B}$ over $0 < y < 2.5$ in the Pb+Pb center-of-mass and is expressed as a fraction of the initial beam kinetic energy per nucleon. The dispersion in kinetic energy per nucleon calculated over the same range is also shown. The bottom row shows the RQMD 2.3 calculation for the $N_{Pb} + N_{Pb}$ system.

net baryon number is conserved and the nucleons are the lightest baryons). While the mean energy loss is large (70%) for all centrality bins, the change in energy loss between the most peripheral and most central collisions is only 6–9%. In addition, there is no significant difference in energy loss between peripheral $Pb + Pb$ collisions and $N_{Pb} + N_{Pb}$ collisions. From this comparison, it can be concluded that if a region of dense, strongly interacting matter is created as a result of A + A collisions, the dependence on the collision centrality of the maximum energy density that can be reached should come almost entirely from the scaling of volume to transverse area ($\sim A^{1/3}$) with little additional enhancement due to the increased stopping which occurs for larger A.

4.3.4 Model Predictions of Stopping

Figures 4.13 and 4.14 show a comparison of the measured $p-\overline{p}$ and $B-\overline{B}$ rapidity distributions to those predicted by RQMD and VENUS. Both of these models well describe the $p-\overline{p}$ and $B-\overline{B}$ distributions in N + N collisions (a comparison with RQMD is shown in Appendix E). The

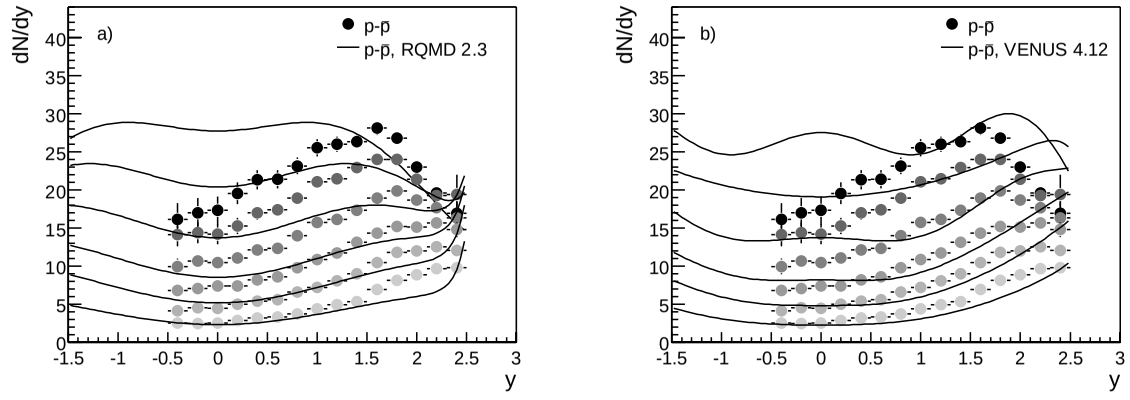

Figure 4.13: $p - \overline{p}$ y distributions compared to RQMD 2.3 and VENUS 4.12. Data points from Figure 4.8 are duplicated in both panels. The curves in the left panel show the RQMD 2.3 predictions for each of the six centrality bins. The curves in the right panel are predictions from the VENUS 4.12 model.

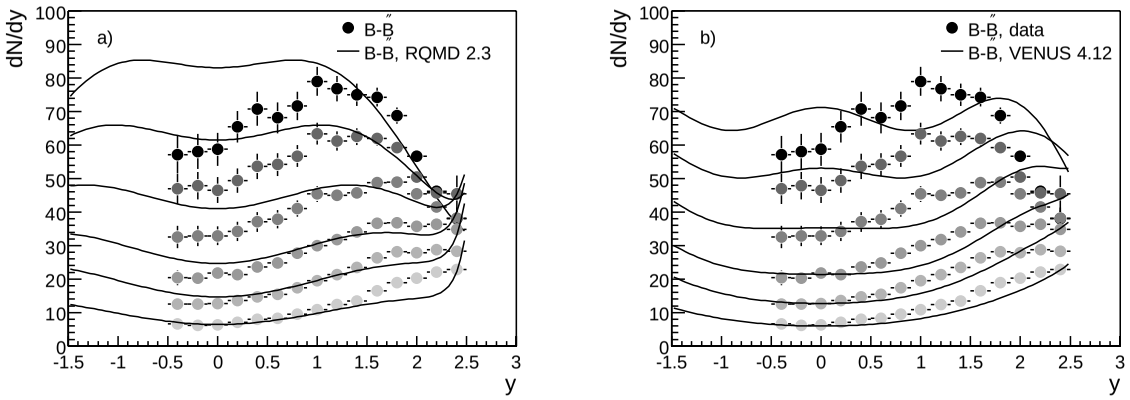

Figure 4.14: $B - \overline{B}$ y distributions compared to RQMD 2.3 and VENUS 4.12. Data points from Figure 4.10 are duplicated in both panels. The curves in the left panel show the RQMD 2.3 predictions for each of the six centrality bins. The curves in the right panel are predictions from the VENUS 4.12 model.

model calculations were made using the b distributions estimated for each centrality sample (see Appendix C). Both RQMD and VENUS well describe the $p - \overline{p}$ and $B - \overline{B}$ yield at mid-rapidity for peripheral collisions. However, both models overpredict the enhancement in the mid-rapidity yield that occurs with increasing centrality. On the other hand, RQMD describes the distributions of $p - \overline{p}$ and $B - \overline{B}$ at forward rapidities best for central collisions and underpredicts the forward rapidity yield for peripheral collisions. VENUS also underpredicts the forward rapidity yield for peripheral collisions but crosses over and overpredicts the forward yield for central collisions. Both models best describe the data in centrality bins 4 and 5.

The fact that the models underpredict the yield at forward rapidities in the most peripheral collisions is puzzling. One possibility is that the b distributions estimated for the centrality bins and used for making the model calculations do not accurately represent the actual b distributions in

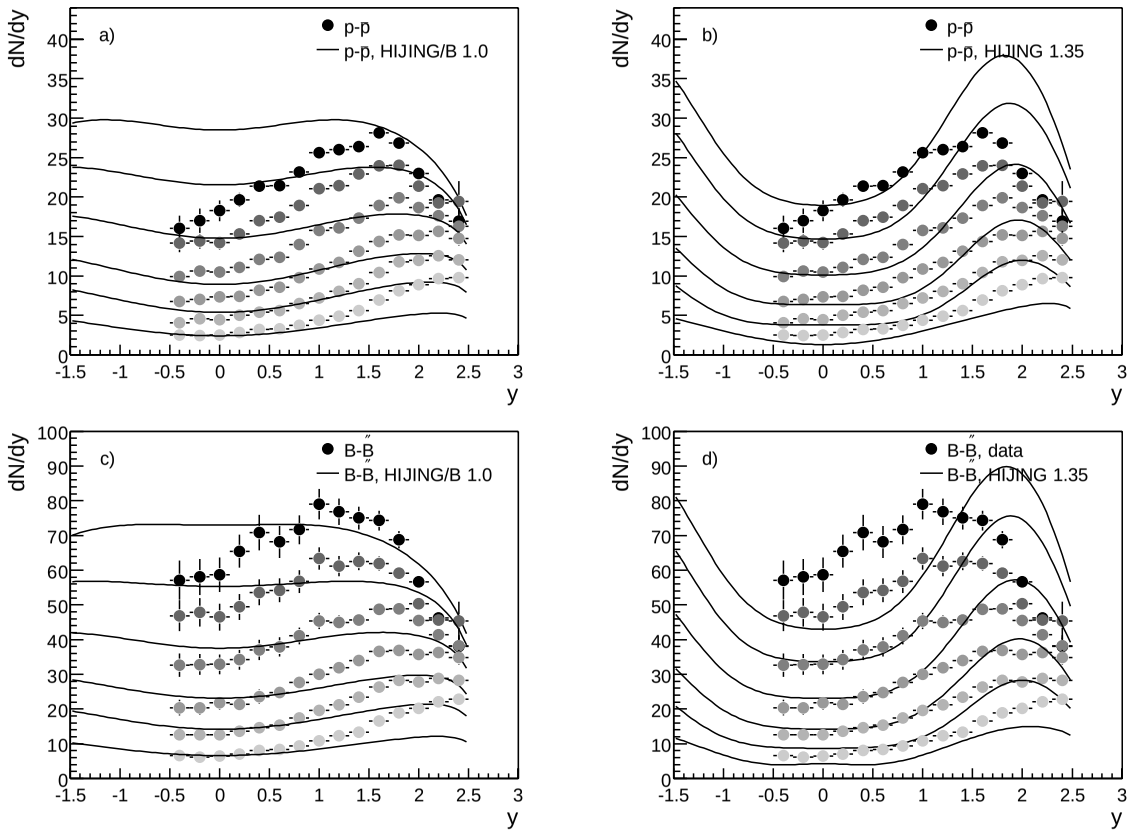

Figure 4.15: $\mathrm{p}-\overline{\mathrm{p}}$ (top) and $\mathrm{B}-\overline{\mathrm{B}}$ (bottom) y distributions compared to HIJING/B (left) and HIJING (right) calculations for the impact parameter distributions corresponding to each centrality bin.

the data. Better agreement with the additional forward peaking in the data could be achieved by including even more peripheral b values in the model calculations. However, doing this would reduce the total yield of $\mathrm{p}-\overline{\mathrm{p}}$ and $\mathrm{B}-\overline{\mathrm{B}}$ and the models already underpredict the total yield also. Another possibility is that the participant-spectator model discussed in Chapter 1 and displayed in Figure 1.1 is taken too literally in the models, which may not reasonably calculate the interactions of the nucleons at the surface of one nuclei with what would otherwise be the spectator portion of the other nucleus. This failure of the models to describe the data at these forward rapidities is significant, as it extends to more than one unit of rapidity below the beam, and nucleons there have lost more than half of their initial center-of-mass kinetic energy.

As noted in Chapter 1, both of these models contain mechanisms beyond the quark-diquark picture which enhance the stopping of baryons. From these comparisons, it appears that these mechanism are too effective at increasing the stopping and that this results in an overprediction of the stopping. To explore this further, Figure 4.15 shows comparisons of the data to the HIJING model (right panels),[GW94] which contains no additional stopping mechanism, and a modified version of HIJING, called HIJING/B [VGW98, Van99], which includes a dynamical model for baryon junction interactions.

For both HIJING and HIJING/B, the total yield of $\mathrm{p}-\overline{\mathrm{p}}$ and $\mathrm{B}-\overline{\mathrm{B}}$ are substantially under-predicted in the peripheral bins. This disagreement is worse than that seen in RQMD and

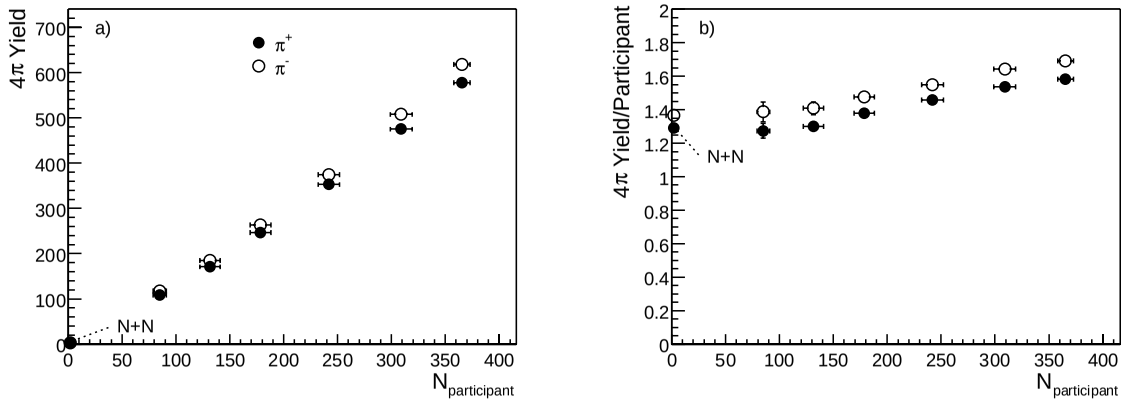

Figure 4.16: Total π yield vs. centrality. The total pion yield is estimated by assuming rapidity distributions symmetric about $y = 0$ and extrapolating to high rapidity as described in the text. The left panel shows the total yield of π^+ and π^- as a function of the estimated number of participants in each centrality sample. The right panel shows the yield per participant.

VENUS and indicates an even bigger problem with the description of peripheral collisions in HIJING. While the increased mid-rapidity yield of HIJING/B matches the data well, this is achieved with a flattened rapidity distribution whose shape disagrees with the data more strongly than the other models. As the collisions become more central, HIJING, in contrast with the other models, severely under-predicts both the shift in the peak toward mid-rapidity and the mid-rapidity yield; however, this can be traced at least in part to the failure of HIJING to reproduce the mid-rapidity yield in $\mathrm{p} + \mathrm{p}$ collisions [GPV97]. HIJING/B, which has been tuned to reproduce the mid-rapidity yield in $\mathrm{p} + \mathrm{p}$ collisions [Van99], does better than HIJING at describing the central collision data, but like RQMD and VENUS, over-predicts the mid-rapidity yield. From the disagreement in both peripheral and central collisions, it can be concluded that the baryon junction mechanism in HIJING/B is also too effective at increasing stopping in $\mathrm{A} + \mathrm{A}$ collisions.

4.4 Particle Production

Figure 4.16 and Table 4.3 show the estimated total yield and yield per participating nucleon of $\pi^{\pm}$ in each centrality bin. The yield in the forward hemisphere is estimated using the measured yield for $y > 0$ and extrapolating to large y using a fit of the $y > 1$ data points to a Gaussian symmetric about mid-rapidity. Because of the symmetry of the collision, the total yield is assumed to be twice the forward hemisphere yield.

The total yield of π^- is greater than π^+ in each centrality bin. This is a result of the net negative isospin of the Pb + Pb system. Figure 4.16b and Table 4.3 show that the relative enhancement is independent of centrality. This is consistent with model estimates which have a ratio of $\mathrm{n} - \overline{\mathrm{n}}$ to $\mathrm{p} - \overline{\mathrm{p}}$ yield which is independent of centrality and essentially unchanged from the same enhancement found in the $\mathrm{N_{Pb}} + \mathrm{N_{Pb}}$ system.

The yield per participant of both π^+ and π^- increases with increasing centrality and smoothly connects the yields observed in single nucleon collisions with the central nuclear collisions. The total increase in going from peripheral to central collisions is $24 \pm 3\%$. The increased stopping observed in the $\mathrm{p} - \overline{\mathrm{p}}$ rapidity distributions is also observed in the longitudinal distributions of π, although to a lesser extent. This is shown in Figure 4.17, where the longitudinal distributions of π^+ and π^- have been normalized by the number of participants and divided by the distribution

E_0bin	total yield		yield/participant		
	π^+	π^-	π^+	π^-	π^+-π^-
1	578.7±4.8	617.6±5.3	1.58±0.01	1.69±0.01	-0.11±0.02
2	475.7±4.5	507.7±4.2	1.54±0.01	1.64±0.01	-0.10±0.02
3	352.8±3.1	374.9±2.0	1.46±0.01	1.55±0.01	-0.09±0.02
4	246.7±4.0	263.8±2.4	1.38±0.02	1.48±0.01	-0.10±0.03
5	171.0±2.7	185.2±3.5	1.30±0.02	1.41±0.03	-0.11±0.03
6	108.3±2.6	118.0±3.7	1.27±0.03	1.39±0.04	-0.11±0.05
$N_{Pb} + N_{Pb}$	2.58±0.00	2.73±0.00	1.29±0.00	1.37±0.00	-0.08±0.00

Table 4.3: Total $\pi^{\pm}$ yield vs. centrality. The $\pi^{\pm}$ yields are estimated using the measured rapidity distributions forward of mid-rapidity and normalized in columns 4–6 using the mean number of participating nucleons estimated for each centrality bin. The bottom row shows the RQMD 2.3 calculation for the $N_{Pb} + N_{Pb}$ system.

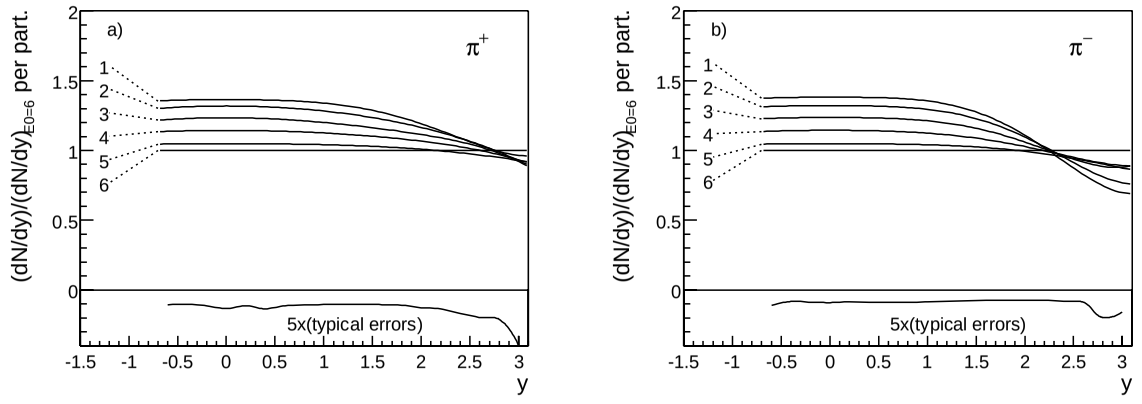

Figure 4.17: Comparison of the shapes of the π^+ and π^- rapidity distributions in each centrality sample (1–6). The distributions are normalized by the number of participants in each sample and divided by the distribution in the most peripheral sample. The resulting distributions were fit to polynomials symmetric about mid-rapidity. Panel a) shows π^+ and panel b) shows π^-. The magnitude of the typical systematic errors are shown below the horizontal axis.

in the most peripheral bin. The yield of very forward pions is constant or slightly suppressed with increasing centrality and all of the increase in yield per participant appears away from this region.

Because of their decreasing yield relative to the number of participating nucleons, fast pions in more central collisions carry away a smaller fraction of the initial nucleon kinetic energy. However, the increased yield of slower pions more than compensates for this and the total fraction of energy carried by pions increases with centrality. This is shown in Table 4.4, where the energy carried by π^+ and π^- is expressed as a fraction of the initial kinetic energy of the participating nucleons. Table 4.4 also shows the estimates for the total energy fraction carried by all π and by K^+, K^-, and all K (estimated as twice $K^+ + K^-$ to include K^0_S and K^0_L). Together, π and K carry most of the energy made available in the collision, as can be seen by comparing Tables 4.2 and 4.4.

E_0 bin	energy/participant (%)					
	π^+	π^-	all π	K^+	K^-	all K
1	17.5±0.2	18.0±0.5	53.3±0.8	6.7±0.4	2.4±0.2	18.4±0.6
2	17.0±0.3	17.4±0.2	51.5±0.5	6.7±0.4	2.5±0.2	18.4±0.8
3	16.2±0.3	16.1±0.1	48.4±0.5	6.0±0.4	2.2±0.2	16.3±0.6
4	15.8±0.8	15.6±0.1	47.1±1.2	5.1±0.4	2.0±0.2	14.3±0.7
5	15.9±0.7	15.0±0.2	46.4±1.0	4.3±0.3	1.7±0.2	12.2±0.7
6	17.2±1.3	15.1±0.1	48.5±2.0	3.8±0.4	1.5±0.2	10.6±0.7
$N_{Pb}+N_{Pb}$	14.7±1.8	15.9±1.9	45.9±3.9	2.0±0.7	1.6±0.6	7.2±1.8

Table 4.4: Energy carried by mesons. The total center-of-mass energy carried by $\pi^\pm$ and $K^\pm$ is normalized by the number of participating nucleons estimated for each centrality bin and is expressed as a fraction of the initial center-of-mass projectile kinetic energy per nucleon. The estimate of the energy fraction carried by all π and K is also shown. These estimates were made using parameterizations of the measured particle distributions, which are given in Appendix F. The bottom row shows the RQMD 2.3 calculation for the $N_{Pb}+N_{Pb}$ system.

4.5 Transverse Momentum Generation

The upper panels of Figure 4.18 show $\langle p_\perp \rangle$ of proton, $K^\pm$, and $\pi^\pm$ as a function of the estimated b in each centrality bin. For all centralities, the $\langle p_\perp \rangle$ of more massive particles is larger, both at mid-rapidity (left panel) and at forward rapidity (right panel). This effect is most pronounced in central collisions but also present in peripheral collisions.

Another common method for characterizing the transverse distributions in A + A collisions is with a fit to an exponential in $m_\perp$ (Equation 3.4), which is an approximation to a Boltzmann thermal distribution [SBM89]. Neither the $\pi^\pm$ nor the proton $p_\perp$ distributions are well fit by this function at all $p_\perp$. For $\pi^\pm$, the yield at low $p_\perp$ is enhanced relative to an exponential fit at high $p_\perp$. This enhancement can arise from decay of resonances. For protons, the yield at low $p_\perp$ is suppressed relative to an exponential fit at high $p_\perp$. The lower panels of Figure 4.18 show the inverse slope, T, obtained from the exponential fits, for $p_\perp$ above the values where these deviations are seen ($p_\perp > 0.4\,\mathrm{GeV}/c$ for $\pi^\pm$and $p_\perp > 0.8\,\mathrm{GeV}/c$ for protons). For $K^\pm$, a single exponential fits the data well over all $p_\perp$. Again, for all centralities, T is larger for more massive particles and this effect is most pronounced in central collisions. However, the relative difference as measured by T between $\pi^\pm$, $K^\pm$, and protons is smaller than that as measured by $\langle p_\perp \rangle$. In addition, in comparing central and peripheral collision, the difference in T between particle species approaches zero more rapidly than the difference in $\langle p_\perp \rangle$. This indicates that the low $p_\perp$ effects observed in the $\pi^\pm$ and proton distributions are less dependent on the system size than the high $p_\perp$ spectral shapes.

As discussed in Chapter 1, attempts have been made to describe the mass dependence of the transverse spectral shapes by considering $p_\perp$ generation by successive collisions of the incident nucleons of one nucleus with the nucleons of the other nucleus [LNS97] and by considering the limit in which rescattering among the produced particles results in hydrodynamic behavior [SSH93a]. In the rescattering picture, produced particles moving with high longitudinal or transverse velocity can collide with particles of lower velocity. This drives slow, more massive particles such as protons toward higher $p_\perp$ and fast moving, light particles such as pions toward lower $p_\perp$. In the limit of a large number of rescatterings, hydrodynamic flow, which is characterized by a common flow velocity shared by all particles, develops. Independent evidence for rescattering in heavy ion collisions at the SPS comes from studying the strength of two particle correlations as a function of transverse momentum [He^+96, Ap^+98b] and from the observation of azimuthally anisotropic charged particle and proton distributions in non-central collisions [Ap^+98a]. The variation with centrality of the magnitude of the rescattering effect should depend on the degree to which the hydrodynamic limit

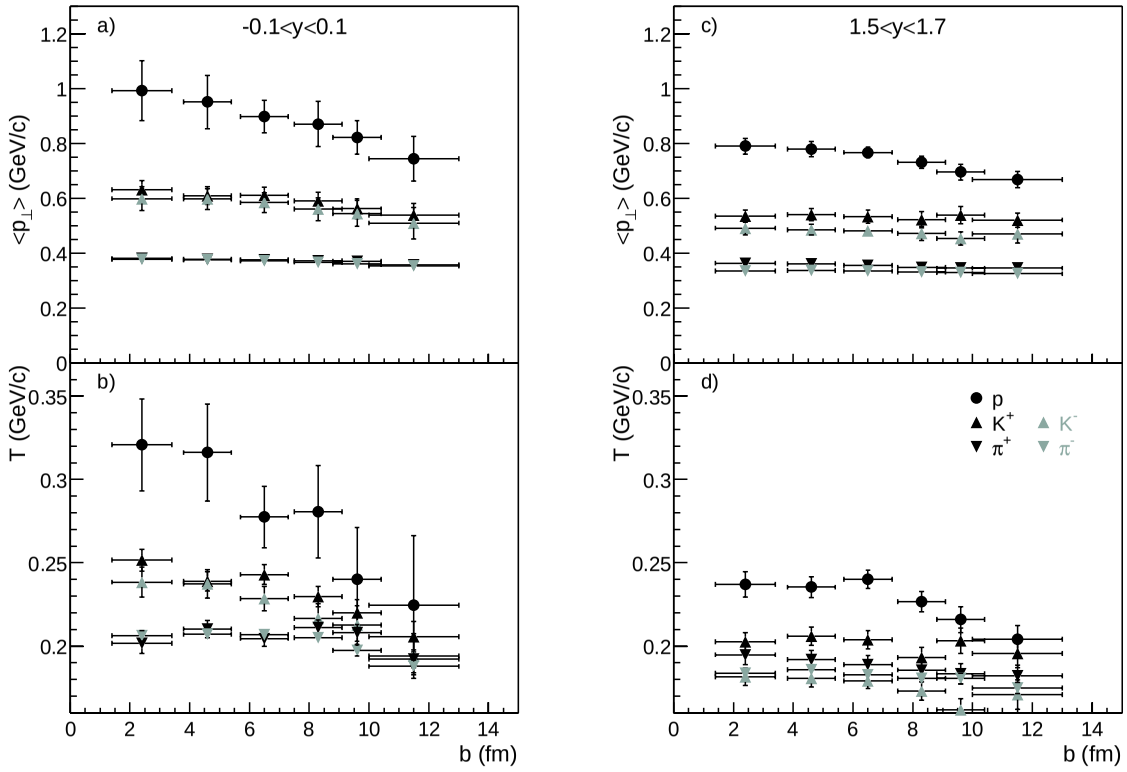

Figure 4.18: $\langle p_\perp \rangle$ and fitted slope vs. b. The upper panels show the $\langle p_\perp \rangle$ and the lower panels show the fitted inverse slope (T) from a fit to an exponential in $m_\perp$ for $\pi^\pm$, $K^\pm$, and proton. The left panels are for mid-rapidity and the right panels are for a forward rapidity. Ranges in $p_\perp$ over which T is determined are specified in the text.

is approached, since the mean number of rescatterings per produced particle will depend on the size of the produced system. In fact, in [VP00], the systematic dependence of the anisotropic particle emission on centrality and energy is studied and the results at the SPS are interpreted as evidence not of the development of fully hydrodynamic behavior but as rescattering in the limit of few collisions.

In the random walk picture, nucleons develop an increasing velocity transverse to their initial direction with each successive collision. Thus, the successive collisions and associated particle production occur in reference frames with increasingly greater transverse velocity relative to the beam direction. As in the rescattering picture, this transverse motion increases the observed $p_\perp$ of heavy particles more than that of light particles. However, the magnitude of this effect depends not on the produced system size but on the number of collisions which the incident nucleons suffered. Since the degree of stopping depends on the number of collisions and the distribution in number of collisions which the incident nucleons suffer is broad, the effect of the random walk on the $p_\perp$ distributions at fixed y, especially for protons, may depend relatively weakly on centrality. Independent evidence for the random walk picture comes from the study of p + A collisions. In this system, where significant rescattering among the few produced particles is not possible, hardening of the $p_\perp$ spectra is observed to be correlated with stopping of the incident proton [To$^+$87, Sik99].

While past analyses of data have attempted to rule in favor of either the rescattering or random walk pictures, it is possible that in A + A collisions both effects are important. Microscopic cascade models should include both of these effects and provide a tool for assessing their relative

strengths. However, more detailed understanding of the dependence of the produced transverse spectra on the number of initial nucleon collisions is required. The data presented in this thesis provide such information because of the well-controlled collision geometry and the large phase-space coverage. Additional information can be gained from data from p + A collisions when events are selected on the rapidity loss of the incoming nucleon, even though the capabilities for controlling the collision geometry and, therefore, restricting the number of collisions that the incoming proton has suffered, are poorer than in A + A collisions. Such data with sufficient statistics have recently become available from the E910 experiment [Ch+99] at the Brookhaven AGS and from the NA49 experiment. Together with the results shown in Figure 4.18, these data may be used to assess the relative contributions of the initial state scattering and produced particle rescattering to the observed systematics of the transverse momentum distributions.

Chapter 5

Conclusion

In collisions between heavy nuclei at the CERN SPS, baryon stopping and particle production have been studied as a function of collision centrality by measuring produced particle spectra with the large acceptance charged particle detector system NA49. Several methods have been used to obtain consistent estimates of the mean and distribution in collision centrality in terms of the collision impact parameter and number of participating nucleons. The produced particle distributions were obtained using the momentum determination and particle identification capabilities of the NA49 TPC's.

Corrections for detector acceptance, tracking inefficiencies, and backgrounds due to feed-down from strange particle decays have been estimated by a detailed detector simulation and applied to the results. Especially for the protons, the data suffer from uncertainties due to poor knowledge of the hyperon distributions used as input to the background estimate. Finalizing the measurement of the centrality dependence of hyperon production from Pb + Pb collisions at the SPS is needed to reduce the systematic uncertainty of the measurements presented in this thesis and should be given high priority.

Using the measured distributions, baryon stopping has been shown to increase with the centrality of the collision, as is expected from the increased nuclear thicknesses involved in the collision. However, even in the most central collisions, significant transparency is still observed. The simple quark-diquark model of stopping underpredicts the degree of stopping that is observed while models which incorporate effects to achieve increased stopping lead to an overprediction of the dependence of stopping on centrality.

While this increase in stopping with collision centrality makes more energy available for producing an excited volume of matter, it is accompanied by an increase in particle production which only slightly exceeds the increase in the number of participating nucleons, corresponding to a scaling in the pion yield of $N_\pi \propto N_{\rm part}^{1.16\pm0.05}$. On the other hand, the transverse distributions of more massive particles become significantly harder for more central collisions. This may indicate that the produced system is approaching hydrodynamic equilibrium, but may also result from the development of transverse motion of successive collision centers as nucleons from one nucleus penetrate and collide within the other nucleus. Assessing the relative strength of these effects requires more detailed theoretical understanding of particle production by successive collisions of nucleons. This understanding will benefit from the data presented here and with particle production data from p + A collisions which are correlated with the degree of stopping suffered by the incident proton. These data are now becoming available.

Bibliography

[AB+91] M. Auguilar-Benitez et al., Z. Phys. C **50**, 405 (1991).

[Af+99] S. Afanasiev et al., Nucl. Instrum. Methods Phys. Res., Sect. A **430**, 210 (1999).

[AGP93] B. Andersson, G. Gustafson, and H. Pi, Z. Phys. C **57**, 485 (1993).

[Ah+99] L. Ahle et al., Phys. Rev. C **59**, 2173 (1999).

[Al+87] G. Alner et al., Phys. Rep. **154**, 247 (1987).

[Al+94] T. Alber et al., Nucl. Instrum. Methods Phys. Res., Sect. A **349**, 56 (1994).

[Al+95] T. Alber et al., Physical Review Letters **75**, 3814 (1995).

[ALE97] ALEPH Collaboration, The ALEPH handbook vols. 1 and 2, Technical report, CERN, 1995, 1997.

[An+99] E. Anderson et al., Phys. Lett. B **449**, 401 (1999).

[Ap+98a] H. Appelshäuser et al., Physical Review Letters **80**, 4136 (1998).

[Ap+98b] H. Appelshäuser et al., Eur. Phys. J. C **2**, 661 (1998).

[Ap+98c] H. Appelshäuser et al., Eur. Phys. J. A **2**, 383 (1998).

[Ap+98d] H. Appelshäuser et al., Phys. Lett. B **444**, 523 (1998).

[Ap+99] H. Appelshäuser et al., Physical Review Letters **82**, 2471 (1999).

[Ba+91] D. Barton et al., Phys. Rev. D **27**, 2580 (1991).

[Ba+99] S. Bass et al., J. Phys. G: Nucl. Part. Phys. **25**, R1 (1999).

[BC74] A. Białas and W. Czyż, Phys. Lett. B **51**, 179 (1974).

[Bi+97] F. Bieser et al., Nucl. Instrum. Methods Phys. Res., Sect. A **385**, 535 (1997).

[BL88] W. Busza and R. Ledoux, Ann. Rev. Nucl. Part. Sci. **38**, 119 (1988).

[BM98] P. Braun-Munzinger, Nucl. Phys. A **638**, 3c (1998).

[BR93] W. Blum and L. Rolandi, *Particle Detection with Drift Chambers*, pages 177–186, Springer-Verlag, 1993.

[Ca+94] A. Capella et al., Phys. Rev. C **236**, 225 (1994).

[Cer98] F. Ceretto, Nucl. Phys. A **638**, 467c (1998).

[Ch+99] I. Chemakin et al., Phys. Rev. C **60**:024902 (1999).

[CK96] A. Capella and B. Kopeliovich, Phys. Lett. B **381**, 325 (1996).

[CL84] T. Cheng and L. Li, *Gauge Theory of Elementary Particle Physics*, Oxford University Press, 1984.

[CNH95] S. Chapman, J. Nix, and U. Heinz, Phys. Rev. C **52**, 2694 (1995).

[En+75] J. Engler et al., Nucl. Phys. B **84**, 70 (1975).

[EOS] EOS Collaboration, *Simulation Documentation.*

[FK72] J. I. Friedman and H. W. Kendall, Ann. Rev. Nucl. Sci. **22**, 203 (1972).

[GEA93] *GEANT, Detector Description and Simulation Tool*, 1993, CERN Program Library Long Writeup W5013.

[GH91] M. Gazdzick and O. Hansen, Nucl. Phys. A **528**, 754 (1991).

[Gla59] R. J. Glauber, in *Lectures in Theoretical Physics*, edited by W. E. Brittin and L. G. Dungam, volume 1, page 315, Interscience, New York, 1959.

[GM70] R. J. Glauber and G. Matthiae, Nucl. Phys. B **21**, 135 (1970).

[Go+97] S. Gottlieb et al., Phys. Rev. D **55**, 6852 (1997).

[GPV97] M. Gyulassy, V. T. Pop, and S. Vance, Heavy Ion Physics **5**, 299 (1997).

[GPW97] N. Glendenning, S. Pei, and F. Weber, Phys. Rev. Lett. **79**, 1603 (1997).

[GW73] D. J. Gross and F. A. Wilczek, Phys. Rev. Lett. **30**, 1343 (1973).

[GW94] M. Gyulassy and X.-N. Wang, Comp. Phys. Comm. **83**, 307 (1994).

[Hay99] R. W. Haymaker, Phys. Rep. **315**, 153 (1999).

[He+96] U. Heinz et al., Phys. Lett. B **382**, 181 (1996).

[HM96] J. Harris and B. Müller, Ann. Rev. Nucl. Part. Sci. **46**, 71 (1996).

[HMSV95] I. Huang, S. Margetis, P. Seyboth, and D. Vranic, Reduction of the Calorimeter Data with ^{208}Pb Projectiles at 158 GeV/Nucleon in the CERN Experiment NA49, Technical report, LBL, 1995.

[Hua97] I. Huang, *Global and Collective Phenomena in Pb+Pb Collisions at Projectile Energy of 158 GeV/nucleon*, PhD thesis, University of California, Davis, 1997.

[JC99] P. Jacobs and G. Cooper, Remarks on the Geometry of High Energy Nuclear Collisions, STAR Note 402, 1999.

[Kar75] P. J. Karol, Phys. Rev. C **11**, 1203 (1975).

[Kha96] D. Kharzeev, Phys. Lett. B **378**, 238 (1996).

[KZ89] B. Kopeliovich and B. Zakharov, Z. Phys. C **43**, 241 (1989).

[LNS97] A. Leonidov, M. Nardi, and H. Satz, Z. Phys. C **74**, 535 (1997).

[Mor72] D. Morrison, Review of Many-body Interactions at High Energy, in *Proc. 4th Int. Conf. on high-energy collisions*, page 253, Oxford, 1972, Rutherford Lab, 1972.

[Ody98] G. Odyniec, Nucl. Phys. A **638**, 135 (1998).

[Pol73] H. D. Politzer, Phys. Rev. Lett. **30**, 1346 (1973).

[Raj99] K. Rajagopal, Nucl. Phys. A , 150c (1999).

[Ram98] L. Ramello, Nucl. Phys. A **638**, 261 (1998).

[RD396] RD 32 final report, Technical Report CERN-LHCC 96-16, CERN, 1996.

[Ree90] H. Reeves, Phys. Rep. **201**, 335 (1990).

[RM82] J. Rafelski and B. Müller, Phys. Rev. Lett. **48**, 1066 (1982).

[RM86] J. Rafelski and B. Müller, Phys. Rev. Lett. **56**, 2324 (1986).

[Rol99] C. Roland, *Flavor Fluctuations in Central Pb–Pb Collisions at 158 GeV/Nucleon*, PhD thesis, University of Frankfurt, 1999.

[RV77] G. Rossi and G. Veneziano, Nucl. Phys. B **123**, 507 (1977).

[SBM89] J. Stachel and P. Braun-Munzinger, Phys. Lett. B **216**, 1 (1989).

[Sik99] F. Sikler, Nucl. Phys. A **661**, 45c (1999).

[Sor95] H. Sorge, Phys. Rev. C **52**, 3291 (1995).

[SSH93a] E. Schnedermann, J. Sollfrank, and U. Heinz, Phys. Rev. C **48**, 2462 (1993).

[SSH93b] E. Schnedermann, J. Sollfrank, and U. Heinz, Fireball Spectra, in *Particle Production in Highly Excited Matter*, edited by H. Gutbrod and J. Rafelski, page 175, Plenum Press, New York, 1993.

[tH72] G. 't Hooft, 1972.

[To+87] W. Toothacker et al., Phys. Lett. B **197**, 295 (1987).

[Toy99] M. Y. Toy, *Baryon Stopping and Charged Particle Production from Lead–Lead Collisions at 158 GeV per Nucleon*, PhD thesis, University of California, Los Angeles, 1999.

[Tra96] T. Trainor, A Comparison of 1D⊗1D and 2D Cluster Finders for the NA49 Time Projection Chambers, Unpublished, 1996.

[Van99] S. E. Vance, *The Role of the Baryon Junction in Relativistic Heavy-Ion Collisions*, PhD thesis, Columbia University, 1999.

[VG99] S. E. Vance and M. Gyulassy, Phys. Rev. Lett. **83**, 1735 (1999).

[VGW98] S. Vance, M. Gyulassy, and X. Wang, Nucl. Phys. A **638**, 395c (1998).

[VH95] F. Videbæk and O. Hansen, Phys. Rev. C **52**, 2684 (1995).

[VP00] S. Voloshin and A. Poskanzer, Phys. Lett. B **474**, 27 (2000).

[Wer93] K. Werner, Phys. Rep. **232**, 87 (1993).

[WG91] X. Wang and M. Gyulassy, Phys. Rev. D **44**, 3501 (1991).

Appendix A

Glossary of Terms

B,$\overline{\mathbf{B}}$ Final state baryons or anti-baryons including p, n, Λ, Σ, Ξ, and Ω^-, or their anti-particles

b Impact parameter of a nuclear collision, see Figure 1.1

CERN European Laboratory for Particle Physics, Geneva, Switzerland

CT board Control and Transfer board

dE/dx Specific ionization measured for a track

DPM Dual Parton Model, which is a model for nuclear collisions [Ca+94]

$\mathbf{E_0}$ Energy measured by the Zero Degree Calorimeter

HIJING A transport model for nuclear collisions [WG91]

HIJING/B A modified version of the HIJING transport model to incorporate the dynamics of baryon junctions [Van99]

$m_\perp$ Transverse mass, see Appendix B

MTPC Main Time Projection Chamber

NA49 A large acceptance hadronic spectrometer at the CERN SPS

$\mathbf{N_{part}}$ Number of nucleons participating in a collision

$\mathbf{N_{Pb}}$ Hypothetical nucleon with isospin content equal to the per nucleon isospin of Pb

$\mathbf{N_{spec}}$ Number of nucleons not participating in a collision

$\mathbf{N_W}$ Number of wounded nucleons determined using a Glauber calculation for a collision at fixed impact parameter

$p_\perp$ Transverse momentum, see Appendix B

QCD Quantum Chromodynamics

QGP Quark-Gluon Plasma

RQMD Relativistic Quantum Molecular Dynamics, which is a cascade model for nuclear collisions [Sor95]

S_3 Gas Cerenkov Trigger Detector

SPS Super Proton Synchrotron, accelerator at CERN

TOF Time-of-flight

TPC Time Projection Chamber

VENUS A transport model for nuclear collisions [Wer93]

VTPC Vertex Time Projection Chamber

x_F Feynman-x variable, see Appendix B

y Rapidity, see Appendix B

ZDC Zero Degree Calorimeter

Appendix B

Kinematic Variables and Particle Distributions

High energy hadronic and especially A+A collisions produce final states with large numbers of particles. These final states are fully characterized by *exclusive* measurements in which all particles are observed. In practice, making these measurements is difficult or impossible and analyzing such a state is also hard because of the large number of independent variables. Instead, it is more useful to consider *inclusive* processes in which a single particle or small set of particles occur in the final state. In this thesis, only distributions for the single-particle inclusive process

$$a + b \rightarrow c + X$$

will be considered. Here, a and b are the projectile and target, c is the produced particle of interest, and X is whatever else may be produced along with c.

A *fully inclusive* measurement includes all events in which c is produced, regardless of, for instance, the geometry of the collision or what else might be in X. A *semi-inclusive* measurement is made by imposing restrictions on the type of collisions which are considered. In this thesis, semi-inclusive samples are selected based on collision centrality, as determined by the energy of forward going particles measured in the zero-degree calorimeter.

The semi-inclusive process is characterized by the invariant cross section

$$E\frac{d^3\sigma_c}{d^3\boldsymbol{p}}$$

where $d^3\sigma_c$ is the rate for producing particle c in the momentum cell $d^3\boldsymbol{p}$ per unit incident flux, and by the invariant yield

$$E\frac{d^3N_c}{d^3\boldsymbol{p}},$$

where d^3N is the number of particles c in the momentum cell $d^3\boldsymbol{p}$ per event. E is the energy of particle c, measured in the same frame as the momentum $\boldsymbol{p}$. The yield and cross-section are related by

$$E\frac{d^3N_c}{d^3\boldsymbol{p}} = \frac{1}{\sigma_{a+b}}E\frac{d^3\sigma_c}{d^3\boldsymbol{p}}$$

where σ_{a+b} is the total cross-section for collisions which meet the conditions that define the semi-inclusive event sample.

NA49 employs a coordinate system in which the beam direction defines the longitudinal direction and the $+z$-axis. In the plane transverse to the beam direction, the x-axis is horizontal and the y-axis is vertical. The azimuthal angle, as measured from the $+x$-axis, is ϕ.

Cross-sections are reported as a function of either of the longitudinal variables Feynman-x ($x_{\rm F}$) or rapidity (y) and either the transverse momentum ($p_\perp$) or transverse mass ($m_\perp$). $x_{\rm F}$ is defined as

$$x_{\rm F} = \frac{p_z}{p_{z,max}}$$

where p_z is the momentum component in the longitudinal direction measured in the center-of-mass system, and $p_{z,max}$ is calculated for a nucleon-nucleon (N + N) collision at the same center-of-mass energy per nucleon. For Pb + Pb collisions at 158 GeV/nucleon, $p_{z,max} = 8.4 - 8.6\,{\rm GeV}/c$ depending on the produced particle species. Rapidity is defined as

$$y = \tfrac{1}{2}\log\left(\frac{E+p_z}{E-p_z}\right).$$

This variable has the advantage that under a Lorentz boost by velocity β along the longitudinal axis,

$$y \rightarrow y + \tfrac{1}{2}\log\left(\frac{1+\beta}{1-\beta}\right),$$

which implies that differences in rapidity and the shapes of rapidity distributions are invariant under such boosts. The momentum transverse to the beam direction is simply

$$p_\perp = \sqrt{p_x^2 + p_y^2},$$

and for a particle of mass m,

$$m_\perp = \sqrt{m^2 + p_\perp^2}.$$

Rewritten in terms of the kinematic variables, the invariant cross-section and yield are

$$\begin{aligned} E\frac{d^3\sigma_c}{d^3\boldsymbol{p}} &= \frac{E_{max}}{p_{z,max}}\frac{1}{p_\perp}\frac{d^3\sigma_c}{dx_{\rm F}\,dp_\perp\,d\phi} \\ &= \frac{1}{p_\perp}\frac{d^3\sigma_c}{dy\,dp_\perp\,d\phi} \\ &= \frac{1}{m_\perp}\frac{d^3\sigma_c}{dy\,dm_\perp\,d\phi} \end{aligned}$$

and

$$\begin{aligned} E\frac{d^3N_c}{d^3\boldsymbol{p}} &= \frac{E_{max}}{p_{z,max}}\frac{1}{p_\perp}\frac{d^3N_c}{dx_{\rm F}\,dp_\perp\,d\phi} \\ &= \frac{1}{p_\perp}\frac{d^3N_c}{dy\,dp_\perp\,d\phi} \\ &= \frac{1}{m_\perp}\frac{d^3N_c}{dy\,dm_\perp\,d\phi} \end{aligned}$$

where $E_{max} = \sqrt{m^2 + p_{z,max}^2}$. Distributions are often integrated over ϕ and plotted as a function of $p_\perp$ at fixed y or $x_{\rm F}$, and also integrated over both ϕ and $p_\perp$ and plotted as a function of y or $x_{\rm F}$.

Appendix C

Determination of Event Centrality

C.1 Introduction

As discussed in Chapter 1, the nature of the system produced in a collision between two nuclei depends on the geometry of the collision. For spherical nuclei such as Pb, this geometry is determined by the collision impact parameter (b). While b cannot be measured, other experimentally determined quantities including the energy carried by the spectator nucleons, the produced transverse energy, and the produced particle multiplicity are found to be well correlated and good indicators of the centrality of the collision. In addition, measurement of identified hadron distributions over a large fraction of phase space can be used to determine the net baryon number that has been transported away from the projectile and target momenta. Since the net baryon number is conserved, this number is equal to the number of nucleons which interacted inelastically in the collision (N_{part}) and is the complement of the number of spectator nucleons (N_{spec}).[1] It is also useful for comparison to theoretical models to estimate the b distribution and $< b >$ within each centrality sample. This appendix describes the methods used for extracting the centrality measures (b, N_{spec}, N_{part}, N_W) within each event sample. Section C.2 describes supporting analyses which are needed by several of the methods. Section C.3 outlines each of the methods. Section C.4 presents and compares the results.

In NA49, the zero-degree energy (E_0), which is dominated by the energy carried by the projectile spectator nucleons, and a large fraction of the total produced particle multiplicity are measured. These measures can be used to segregate events into samples with different impact parameter ranges. In this thesis, centrality selection is accomplished using E_0 alone. Within each event sample, the identified hadron distributions are extrapolated to estimate the number of nucleons which interacted in the collision.

C.2 Supporting Analyses

C.2.1 Estimate of Trigger Bias

Events are selected by the NA49 trigger and by off-line event cuts. This selection introduces a bias which depends on centrality. This bias must be estimated for use in several of the centrality determination methods. Unfortunately, an insufficient number of untriggered events and events with no target in place were recorded to enable determination of the trigger bias directly. Instead, an

[1] It is customary to refer to those nucleons which interact in the collision as participants. However, in A+A collisions, some nucleons in the collision may participate only through cascading collisions within their original nucleus. For the purpose of this thesis and in Glauber calculations [Gla59, GM70], such nucleons are not included in counting the number of wounded nucleons (N_W) but are included in the number of participating nucleons (N_{part}).

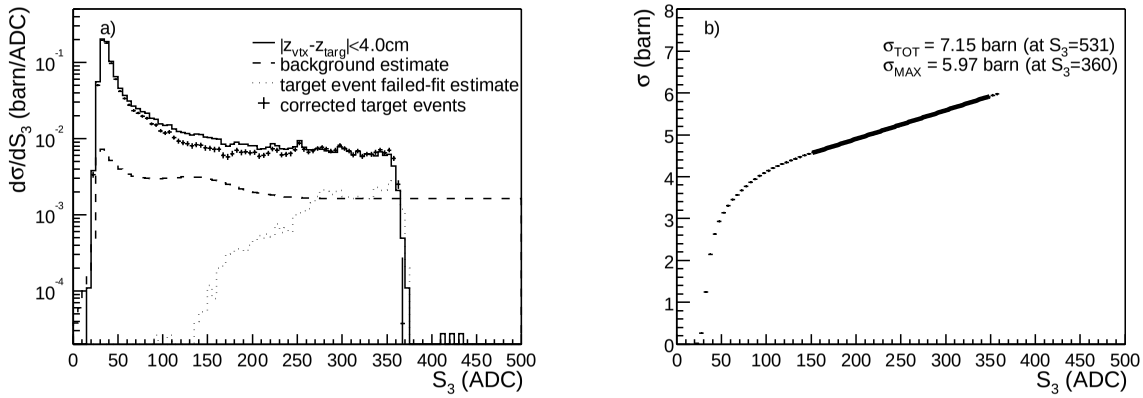

Figure C.1: S_3 spectrum and extrapolation. Panel a) shows the three components which contribute to the estimate of the true Pb + Pb S_3 distribution (corrected target events), shown as data points. Panel b) shows the running integral of the data points in panel a). An extrapolation using a linear fit over the S_3 range of 150-360 is made to the measured beam S_3 ADC signal of 531.

extrapolation of events recorded with a loose trigger is made to estimate the unbiased Pb + Pb interaction cross section. This section describes this extrapolation.

Figure C.1a shows the S_3 ADC distribution for events taken with the looser S_3 veto trigger. The events in this sample are divided into two categories: those where a fit of the primary vertex position from the tracks succeeded, and those where the fit failed. For the fitted events, a cut on the primary vertex z position is made around the target position. The solid histogram shows the spectrum with a loose cut on the position of this fit (±4cm). This spectrum contains both real Pb + Pb events and Pb + gas events which occur close to the target. The Pb + gas event contamination is estimated by considering the distribution of S_3 as a function of primary vertex z position for events well away and either upstream or downstream of the target. These distributions are parameterized. Upstream of the target the parameterization is independent of z. Downstream of the target the parameterization depends on z. These parameterizations are used to estimate the Pb + gas event S_3 spectrum within the above z cut. This estimate is shown in Figure C.1a as the dashed histogram which goes out past $S_3 = 500$. The stability of the difference between the solid and dashed histogram was studied as a function of the cut on the primary vertex z position. With a cut larger than ±3cm, the difference is stable, indicating that essentially all fitted Pb + Pb events have a fitted primary vertex within ±3cm of the target position. The dotted histogram is an estimate of the target events for which a fit of the primary vertex position failed, which occurs primarily because the produced particle multiplicity is too low. The estimate is made by scaling the S_3 distribution of all recorded events without a primary vertex fit by the ratio of the estimates of the Pb+Pb and non-target interaction thicknesses.[2] The estimate of $d\sigma/dS_3$ for Pb+Pb is obtained by (solid) − (dashed) + (dotted) and is shown as data points. Beyond S_3 of about 200, the distribution appears flat.

Figure C.1b shows the running integral of $d\sigma/dS_3$. A linear extrapolation of the curve out to the measured beam S_3 signal (531) is made, which results in a total Pb + Pb interaction cross section of 7.15 barn.[3]

[2] Because events without a vertex fit are low multiplicity, the cross sections assumed for this scaling are not the full Pb + Pb and Pb + gas inelastic cross sections, which are proportional to $(r_A + r_B)^2$. Instead, it is assumed that only the peripheral collision part of the cross section contributes to the low multiplicity events and that this cross section is approximately proportional to $(r_A + r_B)$.

[3] The total Pb + Pb cross section was also calculated according to [Kar75]. The interaction cross sections σ_{pp} and σ_{pn} were assumed to be 30 mbarn, which resulted in a total hadronic inelastic Pb + Pb cross section of 7.1 barn.

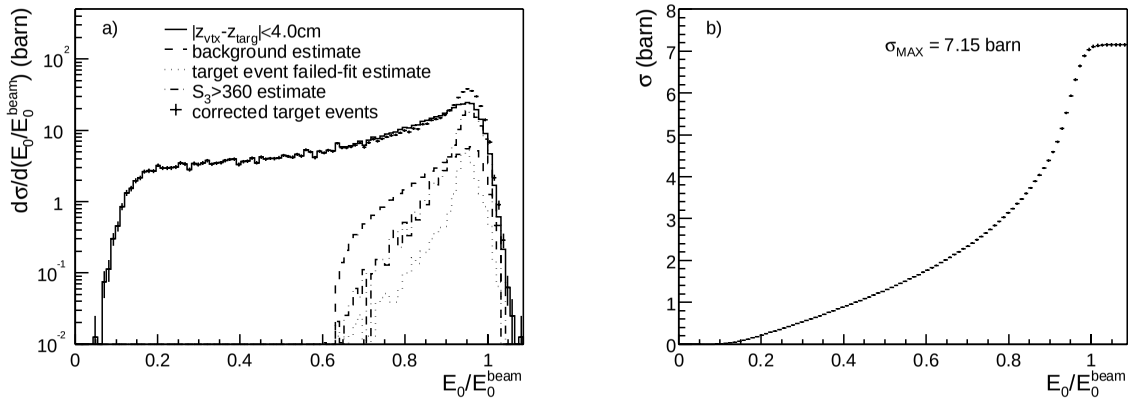

Figure C.2: E_0 spectrum and extrapolation. Panel a) shows the four components which contribute to the estimate of the true Pb + Pb E_0 distribution (corrected target events), shown as data points. Panel b) shows the running integral of the corrected target events in panel a). The total extrapolated Pb + Pb cross section of 7.15 barn agrees well with the theoretically calculated value of 7.1 barn.

For calculating the cross section as a function of E_0, the procedure is nearly the same, except for the extrapolation beyond the S_3 trigger cutoff. Figure C.2a shows the E_0 distribution for events within ±4cm of the target (solid), the estimate of the background (dashed), and the estimate of target events without a vertex fit (dotted). In addition the dot-dashed histogram shows the estimate of the E_0 spectrum of Pb + Pb events which are beyond the S_3 veto threshold. These events are assumed to have the same E_0 distribution as those events just below the S_3 threshold, in the S_3 range of 275-350. In this range the E_0 distribution is nearly constant as a function of S_3. Since the signal in the S_3 Cerenkov detector is approximately proportional to the sum of the square of the projectile fragment spectator charges, this assumption relies on the additional assumption that, for peripheral Pb + Pb events, the probability for producing a high-Z fragment instead of several smaller fragments does not depend on the total number of spectator nucleons. The E_0 distribution for events in the S_3 range 275-350 is scaled to the number of events in the S_3 extrapolation. The estimate of $d\sigma/dE_0$ for Pb + Pb is obtained by (solid) − (dashed) + (dotted) + (dash − dotted) and is shown as data points. The running integral of $d\sigma/dE_0$ is shown in Figure C.2b.

The estimate of the trigger bias as a function of either S_3 or E_0 is obtained by taking the ratio of the S_3 or E_0 distributions for selected events to these estimates of the unbiased distributions.

C.2.2 Simulation of the Zero-Degree Calorimeter

In order to estimate the contamination of E_0 by produced particles and to estimate the correlation between E_0 and b, a simulation of the zero-degree calorimeter response to Pb + Pb collisions was made. Minimum bias VENUS 4.12 events were processed through the GEANT detector simulation code [GEA93] including the effects of beam dispersion, combination of spectator nucleons produced by VENUS into small fragments (d, t, and ^{3}He), and Fermi motion of the spectators. The iron collimator and a simple representation of the zero-degree calorimeter as a single readout-plane were added to the NA49 geometry. Deposited energy was calculated assuming 100 percent shower containment. Because of the configuration of the calorimeter readout, the response is not uniform across the calorimeter face. Since the locations that particles strike the calorimeter face are not measured, no correction for this effect is possible. This leads to a small non-linear relationship between true E_0 and measured E_0 as the composition of spectator particles varies with collision centrality. This calorimeter non-uniformity was also incorporated in the simulation. The energy de-

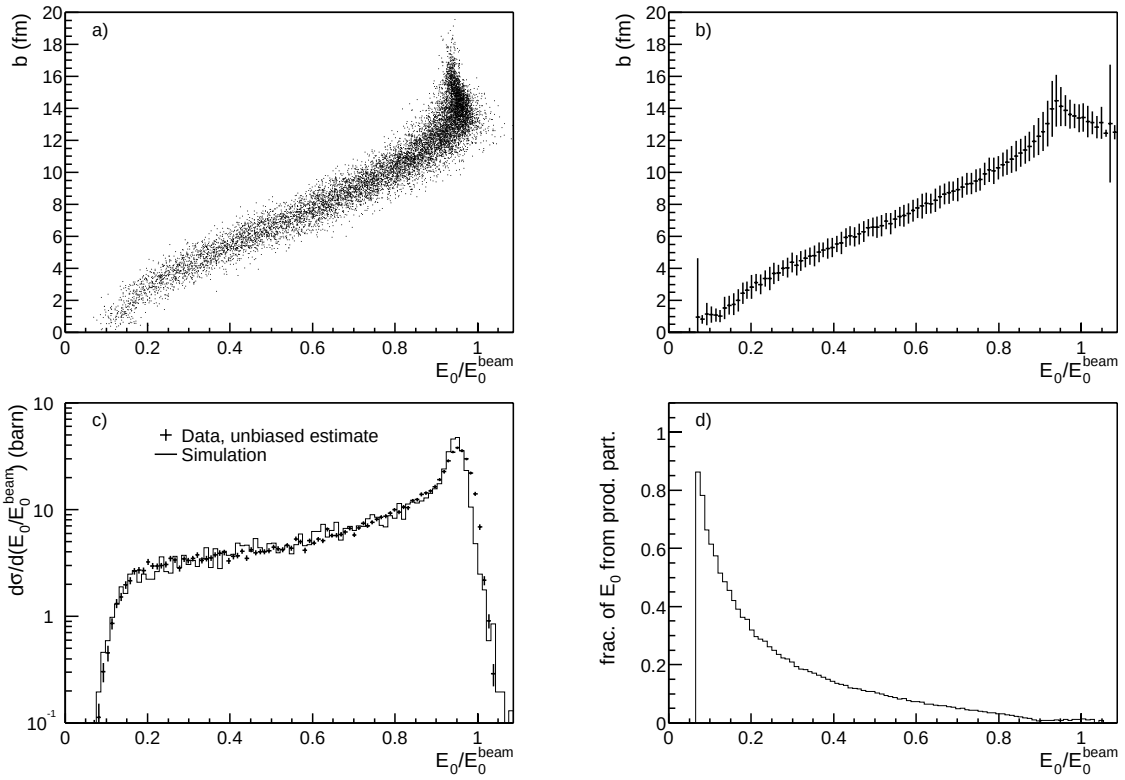

Figure C.3: Simulated E_0 spectrum and comparison to data. Panel a) shows the correlation between b and E_0 from the simulation. Panel b) shows the same result as a profile histogram. Error bars indicate the root mean square deviation in b at fixed E_0. Panel c) shows the comparison between the simulated (histogram) and unbiased data (points) E_0 distributions. Panel d) shows the fraction of the simulated E_0 which comes from non-spectator particles as a function of E_0.

posited in the veto calorimeter includes energy from spectators, some high momentum participating nucleons, produced particles, and leakage from showering in the collimator, whose fractions depend on centrality.[4]

Figure C.3a shows the correlation between b and E_0 obtained from the simulation. The excursion to large E_0 at moderately large impact parameters arises because of the changing composition of the projectile spectator fragments and the non-uniformity of the zero-degree calorimeter response. Figure C.3b shows the same correlation as a profile histogram, where the error bars indicate the root mean square deviation in b at fixed E_0. Figure C.3c shows a comparison between the simulated E_0 distribution and the estimate of the unbiased E_0 from Section C.2.1. These distributions agree well. Figure C.3d shows the fraction of the simulated E_0 which comes from non-spectator particles as a function of E_0. This fraction is largest for the most central events, where the number of spectator nucleons is smallest and the multiplicity of produced particles is largest.

[4] The simulation was adapted from [Hua97].

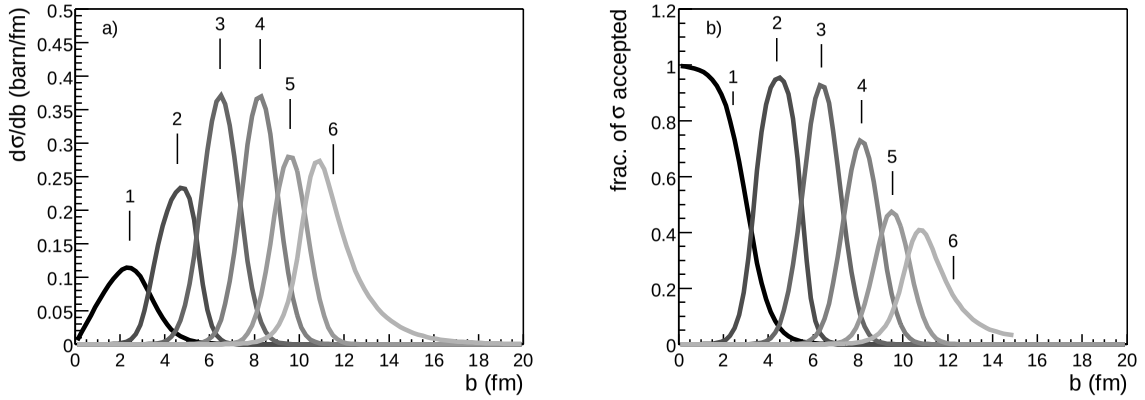

Figure C.4: Estimate of the b distribution for each centrality sample. Panel a) shows the distribution in b for each centrality sample, as estimated by the simulation. Panel b) are the same results normalized by the unbiased distribution so that each curve shows the fraction of events at fixed b accepted into each centrality bin by the NA49 trigger and off-line event selection.

C.3 Methods

C.3.1 Estimate of b by Fraction of Cross Section

A simple, model independent estimate of $\langle b \rangle$ in each centrality sample is made assuming $\langle \mathrm{E}_0 \rangle$ for an event sample increases monotonically with increasing b,[5] so that

$$\int_0^{\mathrm{E}_0} \frac{d\sigma}{d\mathrm{E}_0'} d\mathrm{E}_0' = \int_0^b \frac{d\sigma}{db'} db'$$

where $d\sigma/d\mathrm{E}_0$ is the measured E_0 spectrum corrected for the trigger bias and $d\sigma/db$ is closely given by the geometrical cross-section $2\pi b$ since the probability of at least one nucleon-nucleon interaction is large, up to very peripheral collisions. Because of the finite dispersion in b at fixed E_0, this equation can be solved for b only to obtain an approximate estimate of

$$\langle b(\mathrm{E}_0) \rangle \simeq \left[\frac{1}{\pi} \int_0^{\mathrm{E}_0} \frac{d\sigma}{d\mathrm{E}_0'} d\mathrm{E}_0' \right]^{1/2}.$$

C.3.2 Estimate of b from Simulation

Centrality samples are selected from the data with windows placed on the E_0 measurement. Since the simulated E_0 distribution and the estimate of the real, unbiased E_0 distribution agree well, the simulation can be used to obtain an estimate of the distribution in b, $f_i(b)$, represented by each centrality sample, $i = 1, \ldots, 6$. These distributions are shown in Figure C.4a. Figure C.4b shows the fraction of events at fixed b which fall into each centrality sample, after the trigger and off-line event cut biases have been taken into account. These distributions can be used to estimate the mean number of spectators or participants in each centrality sample from any model which gives, for instance, $\mathrm{N_W}(b)$ by

$$\langle \mathrm{N_W} \rangle_i = \frac{\int \mathrm{N_W}(b') f_i(b') db'}{\int f_i(b') db'}.$$

[5] This assumption can be violated at large b due to the non-uniformity of the zero-degree calorimeter response (see Figure C.3a).

This calculation has been performed using a Glauber model calculation of $N_W(b)$ using a Woods-Saxon parameterization of the nucleon distribution in the Pb nucleus.

C.3.3 Estimate of N_{spec} from E_0

The mean energy deposited by projectile spectator nucleons is the beam kinetic energy per nucleon (T_{beam}/A). An estimate of the number of spectators in an event is obtained from the measured E_0 and the simulated estimate of the E_0 contamination by produced particles ($E_{0,contam.}$) by

$$N_{spec} = (1 - \epsilon(E_0)) \frac{E_0 - E_{0,contam.}}{T_{beam}/A}.$$

where $\epsilon(E_0)$ is the correction estimated from the simulation for the non-uniformity of the zero-degree calorimeter response. $\epsilon(E_0)$ ranges from about 15% for central events to about 5% for the most peripheral events.

C.3.4 Estimate of N_{part} from Spectra

Within each centrality sample, an estimate of N_{part} can be obtained from the measurements of the $p - \overline{p}$ and $K^+ - K^-$ distributions along with model estimates of the yield of net neutrons ($n - \overline{n}$) and net hyperons ($Y - \overline{Y}$) outside of the projectile and target nucleus fragmentation regions. In appendix E, the ratio of $n - \overline{n}$ to $p - \overline{p}$ is studied using the VENUS and RQMD models. Except near projectile and target rapidities, both models indicate only a slight ($\alpha \approx 2 - 9\%$) excess of $n - \overline{n}$ over $p - \overline{p}$. The results from the two models were averaged to obtain an extrapolation factor as a function of y for each centrality bin. These distributions are nearly independent of centrality and except close to beam and target y, are nearly independent of y.

The $K^+ - K^-$ distributions are used to estimate the total strangeness carried by the mesons. By strangeness conservation, this total should be compensated by the net strangeness carried by $Y - \overline{Y}$. It is assumed that $K^+ - K^-$ is equal to $K^0 - \overline{K^0}$ so that the net strangeness carried by the mesons is twice $K^+ - K^-$. Since Ξ and Ω^- carry more than one strange quark, the net strangeness carried by the hyperons is given by

$$(Y - \overline{Y}) \left[1 + \frac{\Xi - \overline{\Xi}}{Y - \overline{Y}} + 2 \frac{\Omega^- - \overline{\Omega}^+}{Y - \overline{Y}} \right] = (Y - \overline{Y}) [1 + \beta] .$$

From measurements of hyperon production in $Pb + Pb$ at the SPS[Ap+98d, An+99], β is 0.1 ± 0.02 and assumed independent of centrality. Then, in terms of measured quantities,

$$N_{part} \simeq (2 + \alpha)(p - \overline{p}) + 2(1 - \beta)(K^+ - K^-).$$

C.4 Results

Table C.1 shows the windows placed on E_0 for selecting the centrality bins, numbered 1 (most central) through 6 (most peripheral), the fraction of the unbiased cross section which each bin covers, and the estimates of b from the methods described in Sections C.3.1 and C.3.2. The b range limits from Section C.3.2 were determined as those values of b for which the bin above and the bin below the limit have equal numbers of events. These limits are compatible with the $\langle b \rangle$ and b_{rms} determined from the distributions in Figure C.4a. The b estimates determined by the cross section fraction and by the simulation agree well.

Table C.2 shows the estimates of N_{spec}, N_W, and N_{part} from the methods described in Sections C.3.2, C.3.3, and C.3.4. In all centrality bins, the estimate of N_W from a Glauber model calculation for the estimated b distribution is less than the estimate of N_{part} from either of the

Bin	E_0 Range (GeV)	Fraction of Cross Section	C.3.1	C.3.2		
			b Range (fm)	b Range (fm)	$\langle b \rangle$ (fm)	$b_{\rm rms}$ (fm)
1	0-9250	0.050	0-3.4	0-3.4	2.4	1.0
2	9250-14670	0.075	3.4-5.3	3.4-5.4	4.6	0.8
3	14670-21190	0.11	5.3-7.3	5.4-7.4	6.5	0.8
4	21190-26080	0.10	7.3-8.7	7.4-9.1	8.3	0.8
5	26080-29340	0.10	8.7-9.9	9.1-10.2	9.6	0.8
6	29340-40000	0.57	9.9-	10.2-	11.5	1.5

Table C.1: Centrality bins and results of estimates of b from Sections C.3.1 and C.3.2.

Bin	C.3.2	C.3.3		C.3.4
	N_W	$N_{\rm spec}$	$N_{\rm part}$	$N_{\rm part}$
1	352	43	373	358
2	281	97	319	299
3	204	164	252	232
4	134	228	188	169
5	88	275	141	122
6	42	328	88	82

Table C.2: Results of estimates of $N_{\rm spec}$, $N_{\rm part}$, and N_W from Sections C.3.2, C.3.3 and C.3.4.

other two methods. This difference is largest for the most peripheral bin. Because the Glauber model calculation does not count in N_W those nucleons which may interact only through cascading within their original nucleus, N_W should be less than $N_{\rm part}$ and the difference should be largest for peripheral collisions in which the spectator portions of the nuclei are the largest.

Also in all centrality bins, $N_{\rm part}$ estimated using the produced particle spectra (Section C.3.4) is less than that estimated from the E_0 measurement (Section C.3.3). Part of this difference is due to the acceptance limit of the measured spectra, which extend only up to $y = 2.5$ and, therefore, slightly underestimate the total number of nucleons which have been transported away from the beam momentum. In addition, the distribution of momenta for spectator nucleons has not been measured. It may be that a fraction of the spectators are not accepted by the collimator and do not deposit their energy in the ZDC. For these reasons, the $N_{\rm part}$ values determined by these two methods are considered reasonable bounds on the true mean $N_{\rm part}$ for each centrality sample.

Appendix D

Simulation of Time Projection Chamber Response

The NA49 experiment is based on four Time Projection Chambers (TPC's). A detailed simulation of the response of these detectors is required to evaluate the detector and reconstruction software performance. These evaluations include determining the detector acceptance, the tracking efficiency, and the resolution with which particle momentum is determined. In addition, simulated particle tracks are used to estimate physics backgrounds. In NA49 analyses prior to this thesis, particle tracking data from each of the detectors were treated independently and separate simulation programs were carried out for the VTPC's and the MTPC's. For use in this thesis and other analyses which utilize the global reconstruction of data from all TPC's, the separate TPC simulations were unified into a single, improved simulation procedure. This procedure has been used in this work to produce both (i) events with a few simulated tracks embedded in raw data and (ii) full Pb+Pb events produced by an event generator. Since tracking inefficiency and precision may depend upon the environment (surrounding track density and noise) in which a track is found, and embedding has the advantage over full event simulation that a realistic tracking environment is automatically provided, the embedding approach is used for determining most of the corrections to the measured results. This appendix describes the simulation procedures in Section D.1, a comparison of the properties of simulated clusters and tracks to those from actual data in Section D.2, and the simulation results used for physics analysis in Section D.3.

D.1 Simulation Procedure and Software

The simulation procedure is carried out using several computer programs that are run sequentially either manually or under control of a simulation script that fits into the standard NA49 data reconstruction framework. The computer programs are similar to those described in detail in [Toy99]. This discussion summarizes what was presented in [Toy99] and includes details where functionality was added to support the global TPC analysis and where enhancements to the simulation algorithms were made. The simulation procedure is displayed graphically in Figure D.1. The simulation input is generated first and saved to a temporary file. The TPC simulation is carried out by an input filter (`mtsim.plugin`) to the reconstruction chain, which, except as noted in section D.1.3, is identical to the one used in the standard reconstruction of raw data. After reconstruction, the reconstructed tracks are matched to the simulation input tracks and this information is used to calculate correction factors.

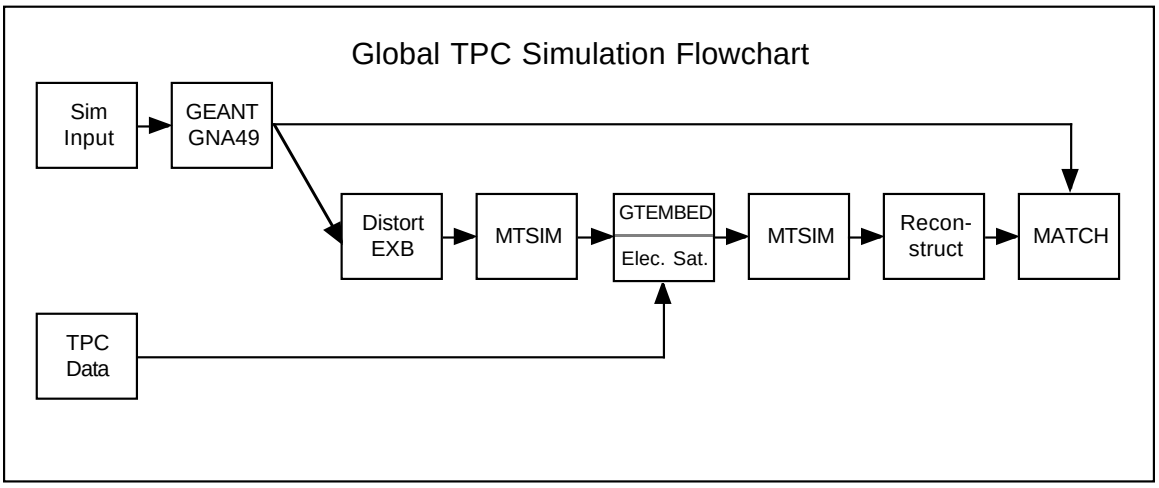

Figure D.1: Flowchart of the global tracking simulation procedure. The computer programs GEANT/GNA49, EXB, MTSIM, GTEMBED, and MATCH are described in the text.

D.1.1 Simulation Input

The simulation input is a list of events, each of which is a list of particles and their momenta at the Pb+Pb interaction point. This list may be generated by Monte Carlo event generators, which produce distributions of particle species and momenta that approximate the physical distributions, or by "hand" according to any other distribution. For embedding studies used in this thesis, events were generated by "hand" with equal numbers of particles and anti-particles of a single species and with a momentum distribution that is uniform in y and $p_\perp$. This has the advantage over using physical distributions that correction factors calculated from the embedding procedure have comparable statistical significance for all particles and all y-$p_\perp$ bins. In calculating correction factors using these flat distributions, input particles are given weights to simulate a calculation using a realistic distribution. For correction factors calculated in this thesis, there was little difference when they were calculated with or without the weight factors.

To achieve good statistical significance with reasonable computing time, up to 35 particles of each charge were embedded in each data event. In order to ensure that this number of embedded particles did not influence the calculation, a smaller number of events were reconstructed with half the number of embedded particles per event. No statistically significant difference was seen between the results of these two calculations.

D.1.2 Tracking Simulation

For tracking particles through the NA49 detector system, a code called GNA49 was constructed based on GEANT [GEA93], which utilizes a Monte Carlo approach for tracking particles through magnetic fields and materials. The tracking incorporates all relevant physical processes such as decay of unstable particles, multiple scattering of charged particles, and production of secondary particles by inelastic reactions with detector materials. GNA49 includes a detailed description of the geometry and materials of the detector system along with many utility routines, including routines for generating input particles with a variety of momentum distributions. GNA49 also includes several optimizations which are switchable and may be used to substantially increase the simulation speed depending upon the level of simulation detail required. For the analyses presented in this thesis, GNA49 was run in the "physics-on" mode, which includes all relevant physics processes and

the highest level of simulation detail. Tracks generated by GNA49 consist of a list of idealized space points at the track intersections with the vertical planes defined by the TPC readout pad rows. Each space point records the spatial coordinates at the point of intersection, the momentum components of the particle at that position, and the ionization energy loss the particle suffered within the pad row.

D.1.3 TPC Response Simulation

From the GNA49 space point information, the TPC response simulation generates raw data in the digitized format produced by the TPC readout electronics. Ideally this simulation should include all the effects of diffusion, distortions, and charge loss which the track ionization cloud suffers as it drifts to the readout plane, amplification by field wires, coupling of the amplification signal to the readout plane, and amplification, shaping, and digitization by the readout electronics. In addition, other known non-ideal behavior of the detector system, which includes cross-talk between channels and undershoot at long times after a signal pulse, should be simulated.[1] Instead of a detailed simulation of most of these effects, a parameterized response function is used. The parameters are fixed by as-built properties of the detector and electronics and by comparison of the simulation results to actual data. This approach has been used previously and is based on work by other TPC-based experiments [ALE97, EOS]. [Toy99] describes the use of the parameterized response function, including the technique for distributing the signal in the pad and time directions for those tracks which are not perpendicular the pad row, and documents the implementation in the computer program, MTSIM. For this thesis, MTSIM was modified to apply these algorithms to the VTPC's.

An additional feature was added to MTSIM to allow switching on and off of selected TPC sectors or individual pad rows within sectors. This was done because difficulties with tripping of one sector in MTPCL during data taking in the 1996 run required disconnecting one sense wire group (corresponding to three pad rows) in MTPCL sector 21. The switching off of sectors and pad rows is controlled by a newly defined data structure. If no instances of these structures are present when MTSIM is run, the default configuration that all sectors and pad rows are on is assumed.

Some effects are not included in the parameterized response and are simulated separately. These include simulation of the distortions and saturation of the readout electronics integrating amplifiers. The largest distortion which occurs in the TPC's is that due to $\boldsymbol{E}\times\boldsymbol{B}$ effects in the VTPC's. This distortion can result in displacements up to several centimeters at the corners of the VTPC's, has a significant effect on the detector acceptance, and, therefore, must be simulated. The other distortions are much smaller. For the simulations used in this thesis, these other distortions were not simulated. Instead, in the reconstruction of the simulations, the corrections for these distortions were turned off. While it would be more accurate to simulate these distortions and then correct for them in the reconstruction, it was judged that the small effect of the distortions on the produced particle distributions did not make this necessary.

The $\boldsymbol{E}\times\boldsymbol{B}$ distortions are simulated by iteratively tracking a test electron from the simulated track space point, through the magnetic field map and vertical electric field, and to the readout plane. After each iteration, the position of the space point along the track is adjusted so that the test electron is forced to arrive closer to the pad row mid-plane. In this way, the idealized space point position defined by the intersection of the particle trajectory with the vertical plane representing the pad row is translated to the position defined by the trajectory's intersection with the distorted surface along which ionization drifts. This calculation is accomplished by the computer program EXB. The originally generated ideal space point position, the true, distorted position, and the apparent position as viewed by the readout plane are recorded in the space point. Recording all of this information simplifies the matching of the reconstructed clusters to the original space points.

[1] Not all of these known detector effects are simulated. For reconstructing actual data, corrections for these effects are applied in the reconstruction [Rol99]. Corrections for those effects that are not simulated are turned off in the reconstruction chain when reconstructing simulated or embedded data.

A new model of saturation of the TPC readout electronics was implemented for this work. A channel can become saturated either when many tracks pass beneath that channel or when a δ-electron spirals tightly in the dipole magnetic field. For the highest multiplicity events, saturation occurs over a significant fraction of the readout channels in the regions of the TPC's with the highest density of tracks. The saturation effectively turns off channels at late drift times depending on the amount charge already integrated by the channel readout. The distribution in saturation charge was determined by studying the recorded data. Although the readout electronics were loaded on the chamber so that front-end cards having the largest as-built dynamic range were used in the highest density regions in the TPC's, the saturation model does not take this into account. Instead, the model randomly assigns a saturation charge value to each channel based on a normal distribution with a mean (4500 ADC counts) and a standard deviation (400 ADC counts), which were found when studying the response of all TPC channels together.

In order to optimize computing time, simulation of the electronics saturation is actually implemented in the computer program GTEMBED, which carries out the embedding step of the simulation procedure and which is described in section D.1.4. When embedding, a decision of whether or not a channel has become saturated depends on both the raw data and the simulated data that is being embedded. Both the embedding and the simulation of the channel saturation require unpacking and repacking of the digitized data on a channel-by-channel basis. By combining these two steps, the unpacking and repacking are done only once.

D.1.4 Embedding of Simulated Data into Raw Data

The computer program GTEMBED is based on the MTPC embedding program, MTEMBED, described in [Toy99]. Other than adding the capability for embedding VTPC digitized data, the only substantial addition is the simulation of the saturation of the TPC readout electronics, described in section D.1.3. For simulating full event generator events, GTEMBED can also be run in a mode which does no embedding but only implements the simulation of the electronics saturation.

D.1.5 Evaluation

Matching a reconstructed track to the simulated trajectory from which it originates involves first matching the reconstructed clusters to the simulated space points from which they originate. This is done by a correlation in position over a predefined search area in the pad row plane. The search area used is a square of 0.5×0.5cm, which is large enough to ensure matching even when relatively large cluster displacements occur due to cluster merging. This large search area can result in multiple matches between clusters and space points. All matches are recorded in linked lists and ambiguities are resolved at the track matching level.

Track matching is accomplished by finding GNA49 tracks whose space points are matched with a minimum number of reconstructed points on a reconstructed track. This analysis is done first on the track segments within each TPC and the results are then tabulated for the full length of the global track over several TPC's. For this thesis, loose track matching criteria were used (5 matched points in VTPC's and 10 matched points in MTPC's). While this was usually sufficient to resolve ambiguities between point matches, occasional spurious track matches were later rejected by ensuring that the majority of clusters on reconstructed TPC track segments were matched to original space points.

The computer program MATCH which implements this evaluation is based on MTEVAL, described in [Toy99]. MTEVAL was modified to perform the matching in the VTPC's and to utilize the NA49 data structures for global tracks.

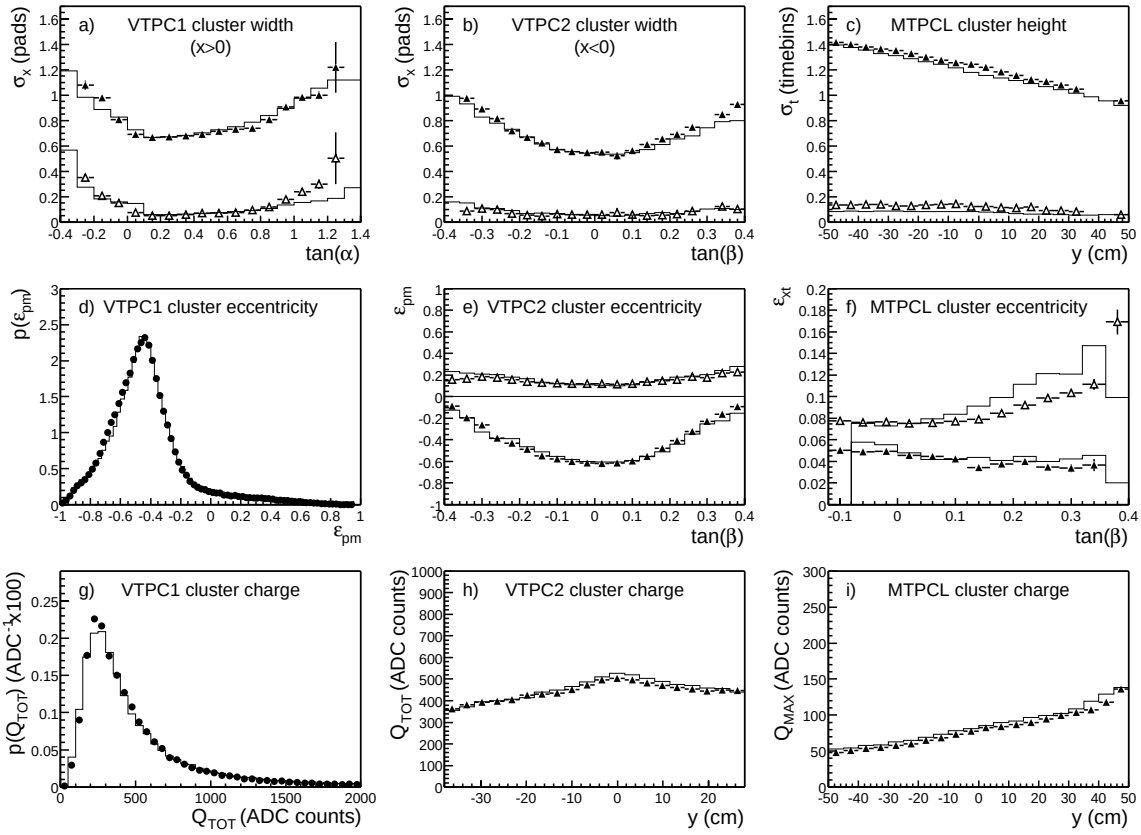

Figure D.2: Comparison of actual (−) and simulated (symbols) cluster characteristics. Characteristics studied are the spatial size (σ_x and σ_t), the cluster eccentricity (ϵ_{pm} and ϵ_{xt}) and the cluster charge (Q_{TOT} and Q_{MAX}). The probability distributions (•) and the variation of the mean (▲) and standard deviation (△) of these characteristics as functions of the cluster vertical position (y) and sense wire (α) and pad (β) crossing angles are shown.

D.2 Comparisons to Data

In order to validate the TPC response simulation and improve the agreement between the simulation and the data, measures of cluster and track properties were developed for comparing the simulation to the data. The properties measured were cluster spatial size, shape, and charge amplitude, cluster residuals relative to the reconstructed track, and the number of clusters per track. These properties were studied as a function of position in the TPC's and as a function of track geometry. The agreement between the simulation and data was improved by an iterative procedure where several of the tunable parameters in MTSIM were adjusted based only on the differences in the real and simulated cluster characteristics. The tunable parameters, which include diffusion coefficients, pad and time response widths, noise level, and TPC gains, are described in the comments contained in the MTSIM header file `mtsim_t.h`.

Sample distributions of cluster characteristics are shown in Figure D.2 (9 distributions out of 144 used are shown). The cluster sizes, shown in the first row of panels, are measured by the standard deviation (σ) of the cluster charge distribution in either the horizontal direction (x) or the vertical drift direction (y). Clusters broaden with decreasing height in the chamber due to

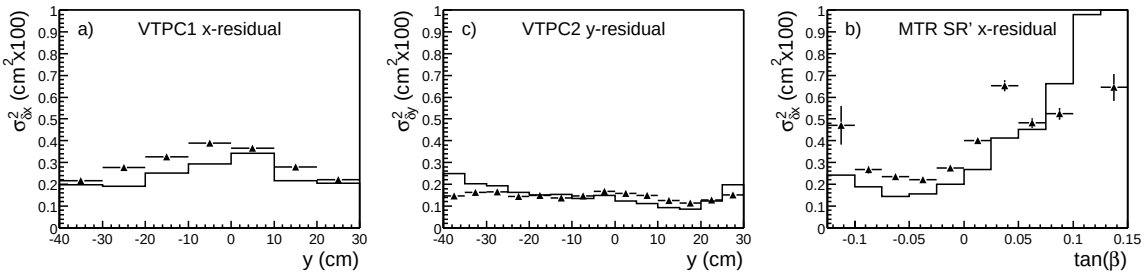

Figure D.3: Comparison of actual (−) and simulated (▲) cluster residuals. The plots show the variance of the horizontal or vertical residual distributions ($\sigma^2_{\delta x}$ or $\sigma^2_{\delta y}$) as a function of the vertical position of the clusters or of the pad crossing angle (β) of the track.

diffusion over increasing drift distance. Clusters are also broader when tracks cross at angles to the pad direction (β) simply due to geometry and also when they cross at angles not normal to the wire direction (α) due to the wire $\boldsymbol{E}\times\boldsymbol{B}$ effect [BR93]. These effects are included in the MTSIM parameterized response. The cluster normalized eccentricities (ϵ_{pm} and ϵ_{xt}) shown in the middle row of panels of Figure D.2 were first studied in NA49 in [Tra96]. They measure the correlation between the dimensions of a cluster in the pad and drift directions in units of time bin and pad width. The peak in the distribution of ϵ_{pm} at about -0.5, which is shown in panel d), arises because the time sampling of the readout electronics is nearly twice the horizontal sampling provided by the pad plane segmentation. This produces clusters that are on average longer in number of time bins than they are wide in number of pads. Variation in the eccentricities of clusters arises from non-zero track crossing angles in either or both of the horizontal or vertical directions. Good agreement between the simulation and the data in these measures indicates that the MTSIM charge distributions for tracks with non-zero crossing angles are adequate. The bottom row of panels in Figure D.2 shows the total cluster charge (Q_{TOT}) and the cluster maximum ADC value in any single time bin (Q_{MAX}). The total cluster charge varies due to several effects, including the distribution in particle species and momentum, track crossing angles, and charge loss during drift. The variation in Q_{MAX} with drift distance is also due to diffusion. Good agreement between the simulation and the data, especially when studied differentially as a function of momentum, angles, and drift distance, indicate that the initial ionization (from GEANT/GNA49) and the charge loss and diffusion (from MTSIM) are adequately simulated.

Sample distributions of the comparisons between the cluster residuals are shown in Figure D.3. For the cluster residuals, the agreement between the simulation and the data is not as good as it was for the other cluster characteristics. This is most likely due to the fact that the uncertainties in the several distortion corrections applied to the data are not taken into account in the simulation. This would be an area for future possible improvement. However, it is not believed that these residuals have a large impact on the efficiency of finding tracks since the actual widths of the cluster residual distributions are significantly smaller than the tolerances in the tracking algorithms for associating clusters with tracks. Improving the simulation of the cluster residuals would improve the measure of the momentum resolution (see section D.3).

The comparisons between the distributions in the number of clusters on tracks, for each TPC separately, are shown in Figure D.4. The agreement between the simulation and data for the VTPC's is good. Features in these distributions are mostly due to the geometry of the detector.[2]

[2] VTPC1 and VTPC2 are divided into sectors with 24 pad rows each. The gaps between sectors are larger than the gaps between pad rows within a single sector. As a result, more tracks can leave the detector in the inter-sector gaps than can leave the detector in the nearby pad row gaps. If all potential clusters on tracks were found, peaks should occur at 24 and 48 clusters, followed by dips at just above 24 and 48 clusters since an extra one or two clusters

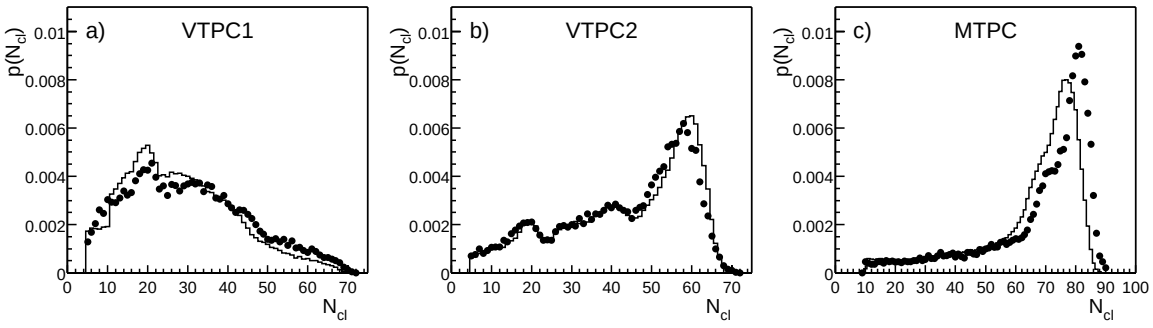

Figure D.4: Comparison of the actual (−) and simulated (•) number of clusters on tracks.

For the MTPC's, simulated tracks with a high number of points have several more points than tracks from real data. Since track quality cuts are placed at a number of points which is below where this deviation is seen, and the integral of both curves above such a cut is the same, this deviation is not expected to degrade the tracking efficiency calculations. Recent study of the difference indicates that this is probably not due to a problem with the simulation, but rather to a difference between the reconstruction chains used for simulated and actual data. The main differences, as discussed in section D.1.3, are in the application of distortion corrections and in the correction for non-ideal detector and electronics behavior. Identifying the actual source of this difference and correcting it requires further work.

Overall, the agreement between the simulation and the data is sufficient for the simulation to be used for determining correction factors to be applied to measured results. Care must be exercised, however, as there may be specific spatial or phase space regions which are not significantly weighted in the comparison distributions studied and which may still have significant deviations. In this work, an attempt was made to identify those regions by looking for corrected momentum distributions which are not smooth. One such location occurs just above mid-rapidity for pions and at low $p_\perp$ where tracks pass through VTPC1, miss VTPC2, and leave a short segment in the MTPC. This problem region was addressed by studying the corrected distributions as the track quality cuts are relaxed. While the corrected distributions remained stable over the remainder of the TPC acceptances, there was substantial variation in this problem region, and here a larger systematic error was assigned to the corrected result.

D.3 Results

The simulations are used to estimate the acceptance and tracking efficiency for primary vertex tracks, and the backgrounds from strange particle decays. For all of these estimates, the results from the reconstruction of embedded events were accumulated in small bins in $\log(p)$ or y, $p_\perp$, and ϕ. The acceptance is defined in each bin by comparing both the number of space points which come from each GNA49 track and which are matched to reconstructed clusters ($N_{cl,matched}$) with the number of those same clusters that are actually used on the reconstructed tracks ($N_{cl,used}$). If any GNA49 tracks which fall into that bin produced no reconstructed clusters ($N_{cl,matched} = 0$), the entire bin is defined to be outside the acceptance. While this definition causes loss of some actual acceptance at the edge of the TPC's, it minimizes the edge effects caused by the finite bin sizes. For bins which pass this acceptance definition, the number of potential points for tracks in that bin is defined by the maximum of the $N_{cl,used}$ distribution. Tracks of high quality will have a

in the adjacent sector are often lost. Since some loss of clusters occurs for other reasons, these peaks and dips shift to slightly lower numbers of clusters.

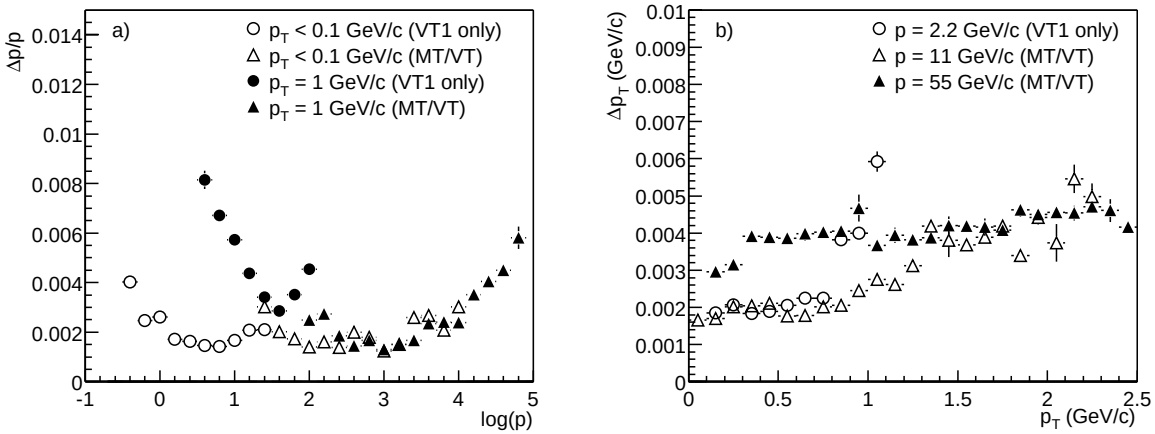

Figure D.5: NA49 momentum resolution. Panel a) shows the relative resolution in total momentum for several tracks classes. Panel b) shows the absolute resolution in $p_\perp$.

large fraction of this number of potential points.

Both the efficiency and background corrections are calculated by counting in each bin the GNA49 input tracks and the number of reconstructed tracks that both pass all imposed track quality cuts and are matched to the input tracks. In making this count, phase space weights are used to transform the simulation input distribution which is flat in y and $p_\perp$ to the estimate of the actual distribution. The corrections are the ratio of these two values. The statistical error on the corrections is estimated by dividing the input sample into three separate samples, calculating the corrections for each third, and calculating the standard deviation of the three results.

The simulation is also used to estimate the resolution of the charged particle momentum determination. This resolution is obtained by comparing the particle momentum from the simulation input to the momentum of the track to which it is matched. Figure D.5 shows results for the relative resolution in total momentum ($\Delta p/p$) and the absolute resolution in $p_\perp$. The results shown are for tracks with $|\phi| < 20°$ and for $\Delta p/p$ (left panel), at fixed values of $p_\perp$, or for $p_\perp$ (right panel), at fixed values of p. In addition, VTPC1 only tracks are considered separately from those tracks that have track segments in at least two TPC's. At low momentum, the momentum resolution is limited by multiple scattering. At high momentum, the resolution is limited by the position resolution and the resulting uncertainty in measuring track curvature. The measured resolution in p is essentially negligible in comparison to the size of the $\log(p)$ or y bins (0.2, which corresponds to $\Delta p/p \approx 20\%$) used in this thesis. The measured resolution in $p_\perp$ ($\lesssim 5\,\mathrm{MeV}/c$) is also negligible in comparison to the size of the $p_\perp$ bins ($100\,\mathrm{MeV}/c$).

Appendix E

Model Predictions of Particle Distributions

In several places in this thesis, model calculations are used to make corrections to measured particle distributions and for comparing to physics results. This appendix describes some of the details concerning the methods and validity of the calculations. Section E.1 describes the use of RQMD 2.3 to estimate the $p-\overline{p}$ and $B-\overline{B}$ distributions which would be produced in the hypothetical nucleon-nucleon collision system ($N_{Pb}+N_{Pb}$) which contains the same isospin content at Pb + Pb. Section E.2 describes the use of RQMD 2.3 and VENUS 4.12 to extrapolate the $p-\overline{p}$ rapidity distributions to $B-\overline{B}$. Section E.3 describes the Glauber calculations of the number of participants and the distribution in number of collisions that the participants suffer in a Pb + Pb collision at fixed b.

E.1 Estimate of $N_{Pb}+N_{Pb}$ using RQMD

The $p-\overline{p}$ distributions measured in p + p collisions are not directly comparable to $p-\overline{p}$ distributions from A + A collisions, and cannot be used compare the baryon stopping. This is because neutrons in A + A collisions may undergo a charge exchange and produce a proton in the final state. As shown by data on neutron production in p + p collisions at the ISR [En+75], the rapidity distribution of nucleons which have undergone charge exchange is different from those that have not. In addition, since only a fraction of nucleons actually undergo charge exchange, the total yield of $p-\overline{p}$, when normalized by the number of participating nucleons, is reduced relative to p+p collisions. The result is that the N + N collision system that is comparable to an A + A collision has both a reduction in the yield and a change in the shape of the $p-\overline{p}$ rapidity distribution, when compared to p + p.

A N+N collision system appropriate for comparison to A+A collisions can be constructed by taking a weighted average of p+p, p+n, n+p, and n+n collisions, with weights chosen according to the p/n content of the nucleus. This averaging is further simplified by noting the isospin symmetry of

$$n+n \rightarrow (p-\overline{p})+X \iff p+p \rightarrow (n-\overline{n})+X$$

and of the summed reactions

$$\left.\begin{array}{c} p+n\rightarrow(p-\overline{p})+X \\ + \\ n+p\rightarrow(p-\overline{p})+X \end{array}\right\} \iff \left\{\begin{array}{c} p+p\rightarrow(p-\overline{p})+X \\ + \\ n+n\rightarrow(p-\overline{p})+X. \end{array}\right.$$

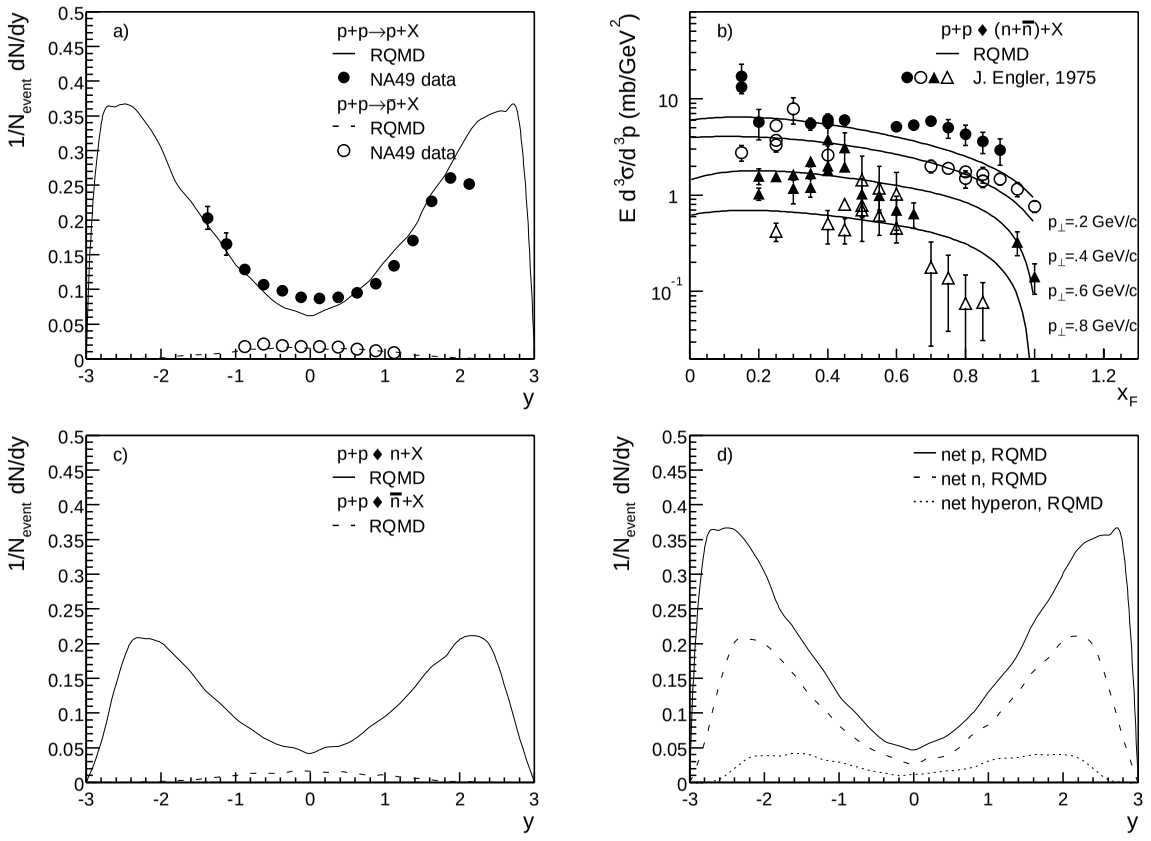

Figure E.1: RQMD calculation of $\mathrm{p}+\mathrm{p}$ collisions. Panels a) and b) compare RQMD calculations to measured data on p and $\overline{\mathrm{p}}$ production [Sik99] and on neutron production [En$^+$75]. Panels c) and d) show the rapidity distributions calculated by RQMD for n, $\overline{\mathrm{n}}$, and net baryons.

As a result, the appropriate $\mathrm{N}+\mathrm{N}$ reaction can be calculated by

$$[\mathrm{N}+\mathrm{N} \rightarrow (\mathrm{p}-\overline{\mathrm{p}})+\mathrm{X}] = \left\{ \begin{array}{c} \frac{Z}{A}\,[\mathrm{p}+\mathrm{p} \rightarrow (\mathrm{p}-\overline{\mathrm{p}})+\mathrm{X}] \\ + \\ (1-\frac{Z}{A})\,[\mathrm{p}+\mathrm{p} \rightarrow (\mathrm{n}-\overline{\mathrm{n}})+\mathrm{X}] \end{array} \right.$$

and, in the case of $\mathrm{Pb}+\mathrm{Pb}$ collisions,

$$[\mathrm{N_{Pb}}+\mathrm{N_{Pb}} \rightarrow (\mathrm{p}-\overline{\mathrm{p}})+\mathrm{X}] = \left\{ \begin{array}{c} 0.394\,[\mathrm{p}+\mathrm{p} \rightarrow (\mathrm{p}-\overline{\mathrm{p}})+\mathrm{X}] \\ + \\ 0.606\,[\mathrm{p}+\mathrm{p} \rightarrow (\mathrm{n}-\overline{\mathrm{n}})+\mathrm{X}]\,. \end{array} \right. \tag{E.1}$$

Unfortunately, available data on neutron production in $\mathrm{p}+\mathrm{p}$ collisions does not cover phase space well. Instead, this procedure is applied to results from model calculations.

As shown in panel a) of Figure E.1, the RQMD 2.3 model well describes data on proton and $\overline{\mathrm{p}}$ production in $\mathrm{p}+\mathrm{p}$ collisions at 158 GeV. These unpublished data were measured by the NA49 collaboration and were presented in [Sik99]. To check the validity of the RQMD predictions of the charge exchange reaction, data from $\mathrm{p}+\mathrm{p} \rightarrow (\mathrm{n}+\overline{\mathrm{n}})+\mathrm{X}$ over the range of ISR energies [En$^+$75] are plotted in panel b) as a function of x_F at fixed $p_\perp$. These data were measured at several

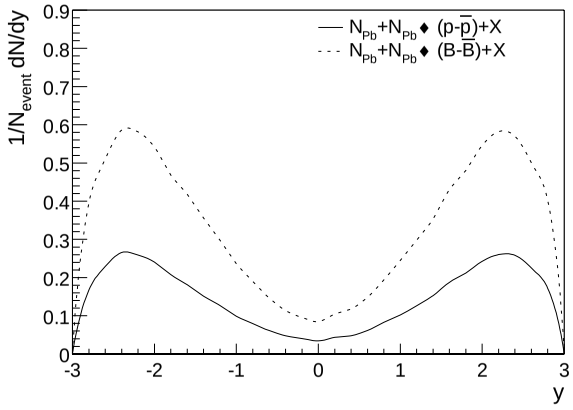

Figure E.2: RQMD calculation of $N_{Pb} + N_{Pb}$ collisions. The $p - \overline{p}$ and $B - \overline{B}$ rapidity distributions are shown.

fixed production angles and interpolated in $p_\perp$ using an exponential fit ($Ed^3\sigma/d^3p \propto \exp(-bp_\perp)$ with $b = 4.8 \pm 0.3$) found to describe the data over almost the full measured range in x_F. Given the significant scatter among the data points, RQMD reasonably describes the data, except at large x_F, where the data seems to show a softer $p_\perp$ distribution. However, this high x_F region transforms to rapidities near beam rapidity and largely outside of the NA49 acceptance. Since RQMD does reasonably describe $p + p \rightarrow (n + \overline{n}) + X$, it can be used to estimate the charge exchange reaction, $n + n \rightarrow (p - \overline{p}) + X$. The rapidity distributions of neutron and $\overline{n}$ from RQMD are shown in panel c) and $p - \overline{p}$ and $n - \overline{n}$ are shown in panel d). These distributions show both the lower yield of charge exchanged nucleons and the reduction in yield at forward rapidities relative to that at mid-rapidity. Also shown is the distribution of net hyperons, which shows these effects to an even larger degree.

Now $N_{Pb} + N_{Pb} \rightarrow (p - \overline{p}) + X$ can be estimated using RQMD, either directly by simulating $p + p$, $p + n$, and $n + n$ reactions, or by using the prescription described above. Figure E.2 shows the result for $p - \overline{p}$ from the $N_{Pb} + N_{Pb}$ collisions, which was calculated using Equation E.1. Also shown is the $B - \overline{B}$ rapidity distribution from $N_{Pb} + N_{Pb}$ collisions, which is the same as that from $p + p$ collisions, since when summed over all baryons, the distributions from $p + p$, $p + n$, and $n + n$ are the same.

E.2 Extrapolation of $p - \overline{p}$ to $B - \overline{B}$

For this thesis, model calculations are used to correct the measured proton and $\overline{p}$ distributions for feed-down from hyperons (Y) and anti-hyperons ($\overline{Y}$) and also to extrapolate the corrected $p - \overline{p}$ distributions to $B - \overline{B}$.[1] In order to asses the uncertainty of this correction and extrapolation, two models, RQMD 2.3 and VENUS 4.12, are used. This uncertainty directly affects the estimated uncertainty in the corrected proton, $\overline{p}$, and $p - \overline{p}$ distributions. Since the model calculations are also used in the extrapolation to $B - \overline{B}$, additional uncertainty should be expected. However, since the hyperon distributions are partially subtracted in the feed-down correction and then added back in the extrapolation to $B - \overline{B}$, it turns out that the relative uncertainties in these two distributions due to the uncertainty in the hyperon distribution are comparable.

As discussed in chapter 3, the net strangeness carried by mesons, which is estimated by twice the yield of $K^+ - K^-$ (the factor of two accounts for the neutral kaons), is approximately

[1] Although the hyperon distributions can be measured over a large fraction of phase space using the NA49 experiment, only a preliminary result for central collisions has yet been obtained and this result has a large uncertainty.

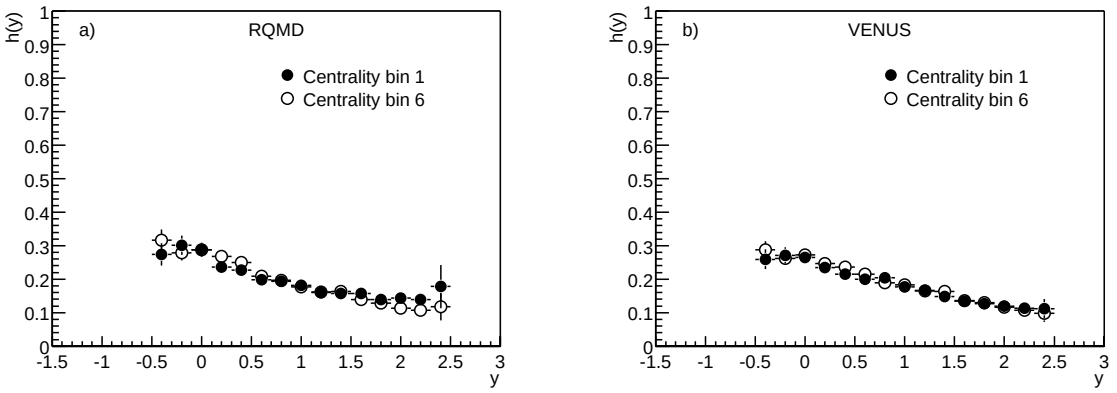

Figure E.3: Transfer function $h(y)$ for estimating proton feed-down. $h(y)$ is the fraction of hyperons produced at a given y which result in a decay proton with a trajectory that is consistent with one from a proton directly produced in the collision. The small differences between the two models result from differences in their hyperon $p_\perp$ distributions.

proportional to the total yield of $\mathrm{Y}-\overline{\mathrm{Y}}$. This fact is used to scale the model predictions of the hyperon distributions to obtain a more realistic input for the feed-down correction and $\mathrm{B}-\overline{\mathrm{B}}$ extrapolation. This input is given by

$$\frac{dN^{\mathrm{input}}_{\mathrm{Y},\overline{\mathrm{Y}}}}{dy} = \gamma \frac{dN^{\mathrm{model}}_{\mathrm{Y},\overline{\mathrm{Y}}}}{dy},$$

where

$$\gamma = \frac{N^{\mathrm{actual}}_{\mathrm{K^+-K^-}}}{N^{\mathrm{model}}_{\mathrm{K^+-K^-}}}.$$

While the actual corrections for proton and $\overline{\mathrm{p}}$ feed-down account for the rapidity shift between the parent hyperon and decay proton or $\overline{\mathrm{p}}$, in practice the rapidity shift is nearly always small and the correction can be approximately expressed as a transfer function $h(y)$ depending only on y by

$$\frac{dN^{\mathrm{feed-down}}_{\mathrm{p},\overline{\mathrm{p}}}}{dy} = h(y)\frac{dN^{\mathrm{input}}_{\mathrm{Y},\overline{\mathrm{Y}}}}{dy}.$$

Figure E.3 shows $h(y)$ for the most central and most peripheral bins for RQMD (left panel) and VENUS (right panel).[2] In terms of the uncorrected proton or $\overline{\mathrm{p}}$ measurement and the input Y or $\overline{\mathrm{Y}}$ distributions, the corrected distributions are

$$\frac{dN^{\mathrm{actual}}_{\mathrm{p},\overline{\mathrm{p}}}}{dy} = \frac{dN^{\mathrm{uncorr.}}_{\mathrm{p},\overline{\mathrm{p}}}}{dy} - h(y)\frac{dN^{\mathrm{input}}_{\mathrm{Y},\overline{\mathrm{Y}}}}{dy}. \tag{E.2}$$

When added in quadrature with the other uncertainties in the uncorrected proton and $\overline{\mathrm{p}}$ distributions, the estimated uncertainty in the hyperon distribution is scaled by the square of $h(y)$.

The extrapolation to $\mathrm{B}-\overline{\mathrm{B}}$ is given by Equation 4.1, which when rewritten in this notation is

$$\frac{dN^{\mathrm{actual}}_{\mathrm{B}-\overline{\mathrm{B}}}}{dy} = (2+\alpha(y))\frac{dN^{\mathrm{actual}}_{\mathrm{p}-\overline{\mathrm{p}}}}{dy} + \frac{dN^{\mathrm{input}}_{\mathrm{Y}-\overline{\mathrm{Y}}}}{dy}. \tag{E.3}$$

[2] The function $h(y)$ depends on the quality cuts imposed on the reconstructed tracks. In particular, cuts on how close tracks project back to the Pb + Pb interaction point reject a larger fraction of tracks from decays than tracks coming directly from the collision. These plots show $h(y)$ for the nominal cuts employed, as discussed in Chapter 3.

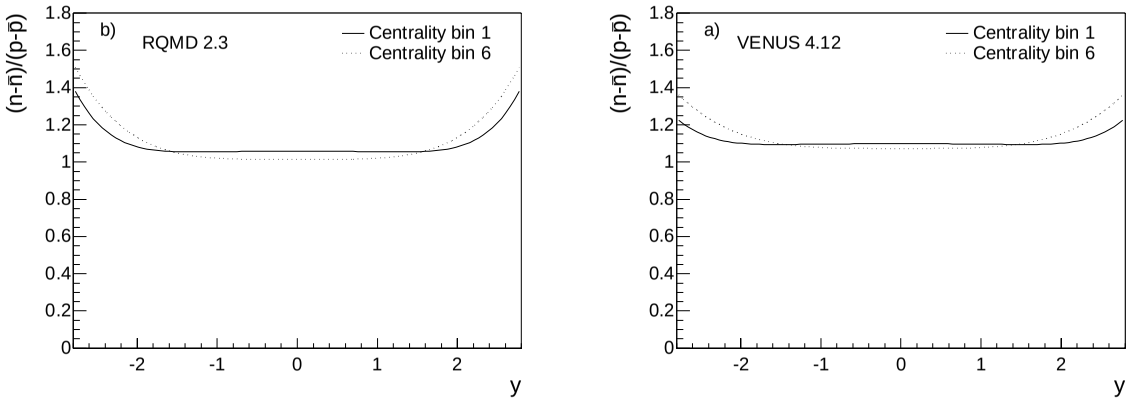

Figure E.4: Ratio of $\mathrm{n}-\overline{\mathrm{n}}$ to $\mathrm{p}-\overline{\mathrm{p}}$ from RQMD (left panel) and VENUS (right panel). Calculations for both the most central and most peripheral centrality bins are shown.

The first factor scales $dN^{\mathrm{actual}}_{\mathrm{p}-\overline{\mathrm{p}}}/dy$ to account for $\mathrm{n}-\overline{\mathrm{n}}$. The $\mathrm{n}-\overline{\mathrm{n}}$ to $\mathrm{p}-\overline{\mathrm{p}}$ ratio is determined using RQMD and VENUS. Figure E.4 shows the ratio of $\mathrm{n}-\overline{\mathrm{n}}$ to $\mathrm{p}-\overline{\mathrm{p}}$ obtained from the RQMD and VENUS models for both the most central and most peripheral centrality bins. Except near projectile and target rapidities, both models indicate only a slight ($\alpha \approx 2-9\%$) excess of $\mathrm{n}-\overline{\mathrm{n}}$ over $\mathrm{p}-\overline{\mathrm{p}}$. The results from the two models were averaged to obtain the extrapolation function $(2+\alpha(y))$ for each centrality bin. These functions are nearly independent of centrality and except close to beam and target y, are nearly independent of y.

Substituting Equation E.2 into Equation E.3 yields

$$\frac{dN^{\mathrm{actual}}_{\mathrm{B}-\overline{\mathrm{B}}}}{dy} = (2+\alpha(y))\frac{dN^{\mathrm{uncorr.}}_{\mathrm{p}-\overline{\mathrm{p}}}}{dy} + \{1-[2+\alpha(y)]\,h(y)\}\,\frac{dN^{\mathrm{input}}_{\mathrm{Y}-\overline{\mathrm{Y}}}}{dy}.$$

To obtain the estimated uncertainty in $\mathrm{B}-\overline{\mathrm{B}}$, the estimated uncertainties in $\mathrm{p}-\overline{\mathrm{p}}$ are now scaled by $2+\alpha(y)$ and the estimated uncertainty in the hyperon distribution is scaled by $1-[2+\alpha(y)]\,h(y)$. The latter factor shows the partial cancellation between the direct contribution of $\mathrm{Y}-\overline{\mathrm{Y}}$ to $\mathrm{B}-\overline{\mathrm{B}}$ and the feed-down correction.

E.3 Glauber Calculations

This section presents the formalism used for making the Glauber [GM70] calculations used in this thesis. Additional applications using this formalism were presented in [JC99]. These calculations assume straight line trajectories of nucleons in the overlap region of the two colliding nuclei. Interaction probabilities are calculated assuming a fixed cross section. For this thesis, the inelastic nucleon-nucleon at the CERN SPS energy ($\sigma_{NN} = 30\,\mathrm{mbarn}$) was used.

The coordinate system and geometry for a collision between projectile nucleus A and target nucleus B is defined in Figure E.5. The nuclei are separated by impact parameter $\boldsymbol{b}$ and calculations are done in a tube $d^2\boldsymbol{s}$ located at position

$$\boldsymbol{s} = \boldsymbol{r}_A + \frac{\boldsymbol{b}}{2} = \boldsymbol{r}_B - \frac{\boldsymbol{b}}{2}.$$

The number density of nucleons in the nucleus is given by the Woods-Saxon distribution,

$$\rho(r) = \rho_0 \cdot \frac{1}{1+e^{(r-R_A)/a}},$$

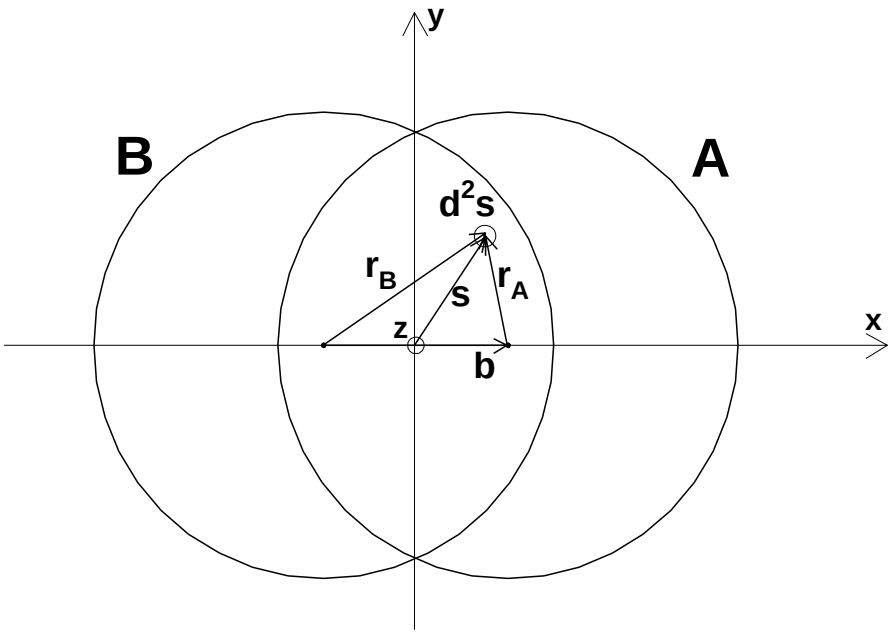

Figure E.5: Geometry used for Glauber calculations. The projectile nucleus A and the target nucleus B are separated by impact parameter $\boldsymbol{b}$.

where $r = \sqrt{s^2 + z^2}$, $R_A = 1.12A^{1/3}$, $a = 0.547$, and $\rho_0 = 0.159\,\mathrm{fm}^{-3}$ for ^{208}Pb.

The area density of nucleons in one nucleus in the plane perpendicular to the z direction is given by the nuclear thickness function,

$$T_A(r_A) = \int dz\, \rho_A(r_A)$$

with the normalization

$$\int d^2\boldsymbol{r}_A\, T_A(r_A) = A.$$

The probability for a nucleon in A at position $\boldsymbol{s}$ to interact with at least one nucleon in B is given by

$$1 - e^{-T_B(r_B)\sigma_{NN}}$$

so that the density of wounded nucleons at $\boldsymbol{s}$, counting nucleons from both the projectile and target, is

$$\frac{d^2N_{WN}}{d^2\boldsymbol{s}}(b,\boldsymbol{s}) = T_A(r_A)\cdot\left(1 - e^{-T_B(r_B)\sigma_{NN}}\right) + T_B(r_B)\cdot\left(1 - e^{-T_A(r_A)\sigma_{NN}}\right).$$

The total number of wounded nucleons at fixed b is calculated by integrating this expression over $\boldsymbol{s}$.

In order to calculate the distribution in number of collisions which nucleons suffer, consider the tube at $\boldsymbol{s}$ with area σ_{NN}. The probability of finding a given nucleon from B in this tube is

$$\frac{1}{B}T_B(r_B)\sigma_{NN}$$

and the probability of finding n nucleons from B in this tube is then[3]

$$\left(\begin{array}{c} B \\ n \end{array} \right) \left(\frac{1}{B} T_B(r_B) \sigma_{NN} \right)^n \left(1 - \frac{1}{B} T_B(r_B) \sigma_{NN} \right)^{B-n}.$$

Likewise, the probability of finding a given nucleon in A in $d^2\boldsymbol{s}$ is

$$\frac{1}{A} T_A(r_A)\, d^2\boldsymbol{s},$$

so that the total probability for a given nucleon in A colliding with n nucleons in B is

$$P_n(b) = \int d^2\boldsymbol{s} \frac{1}{A} T_A(r_A) \left(\begin{array}{c} B \\ n \end{array} \right) \left(\frac{1}{B} T_B(r_B) \sigma_{NN} \right)^n \left(1 - \frac{1}{B} T_B(r_B) \sigma_{NN} \right)^{B-n}.$$

Finally, the probability of m nucleons in A colliding with n nucleons in B is

$$P_{m,n}(b) = \left(\begin{array}{c} A \\ m \end{array} \right) (P_n)^m \, (1 - P_n)^{A-m}.$$

At fixed b, the mean number of nucleons from A which suffer n collisions is

$$\overline{m}_n(b) = \sum_m m P_{m,n}(b)$$

and the mean number of collisions for all wounded nucleons is

$$\overline{n}(b) = \frac{\sum_n n \sum_m m P_{m,n}(b)}{\sum_{n>0} \sum_m m P_{m,n}(b)}.$$

Results from these calculations, averaged over the estimated b distributions of the six centrality bins, are shown in Figure 4.12 and Table 4.1.

[3] This calculation ignores the correlations between nucleon positions within the nucleus. In particular, nucleons are allowed to overlap and the probability of finding large numbers of nucleons within this tube is overestimated, which also results in a slight distortion of $P_{m,n}$ toward higher collision numbers.

Appendix F

Data Tables

This appendix records the $\pi^{\pm}$, $\mathrm{K}^{\pm}$, proton and $\overline{\mathrm{p}}$ spectra as $1/m_{\perp}d^2N/dy\,dm_{\perp}$ and dN/dy. Appendix B describes how to transform these distributions to other kinematic variables. The results for one particle species and one centrality bin are shown on each data page. For space considerations, individual $1/m_{\perp}d^2N/dy\,dm_{\perp}$ are not tabulated but only shown graphically. They can be obtained at `http://na49info.cern.ch`. Data points at $y = 0$ are absolutely normalized and shown as open symbols. Data points away from $y = 0$ are scaled by successive factors of 10 for display purposes and shown as filled symbols. Each $m_{\perp}$ distribution which has a sufficient number of data points is parameterized using the plotted function. dN/dy and the other parameters used are tabulated in the first table on each page. Where there are an insufficient number of data points for determining the yield or parameterization, these spaces are left blank. Both dN/dy and the $m_{\perp}$ distribution parameters are further parameterized as functions of y, and these parameters are tabulated in the second table. The dN/dy distribution and its parameterization are shown in the inset to the figure. In the graphical display of the $m_{\perp}$-distributions, only statistical and particle identification fit errors are displayed. In the dN/dy distributions, all errors, including the systematic error estimated for the feed-down correction, are displayed. The following sections describe the parameterizations employed for each particle species.

F.1 Pions

The transverse distributions of $\pi^{\pm}$ are characterized by an exponential behavior at large $p_{\perp}$ and an excess over this exponential at small $p_{\perp}$. A sum of two exponentials in $m_{\perp}$,

$$\frac{1}{m_{\perp}}\frac{d^2N}{dy\,dm_{\perp}} = \frac{dN}{dy}\left\{\frac{1-\xi_2}{T_1(m_0+T_1)}e^{-(m_{\perp}-m_0)/T_1} + \frac{\xi_2}{T_2(m_0+T_2)}e^{-(m_{\perp}-m_0)/T_2}\right\},$$

with T_1 describing the large $p_{\perp}$ behavior and T_2 describing the low $p_{\perp}$ enhancement, is found to parameterize the distributions well. The parameter ξ_2 is the fraction of the total yield which is contained in the low $p_{\perp}$ enhancement. The parameter T_1 was obtained by fitting the distributions for $m_{\perp} - m_0 > 0.3\,\mathrm{GeV}/c$, which corresponds to $p_{\perp} > 0.4\,\mathrm{GeV}/c$.

The $\pi^{\pm}$ dN/dy distributions are well parameterized with a single Gaussian distribution centered at $y = 0$,

$$\frac{dN}{dy} = \frac{A}{\sqrt{2\pi\sigma_y^2}}e^{-\frac{1}{2}\left(\frac{y}{\sigma_y}\right)^2},$$

with standard deviation σ_y and total yield A. The $m_{\perp}$ distribution parameter T_1 is reasonably well described with the y dependence

$$T_1(y) = \frac{T_{1,0}}{\cosh y/y_{T_1}},$$

while T_2 and ξ_2, given by

$$T_2(y) = T_{2,0}$$

and

$$\xi_2(y) = \xi_{2,0},$$

are nearly independent of y.

F.2 Kaons

The $m_\perp$ distributions of $K^\pm$ are well described by a single exponential,

$$\frac{1}{m_\perp}\frac{d^2N}{dy\,dm_\perp} = \frac{dN/dy}{T(m_0+T)}e^{-(m_\perp - m_0)/T}.$$

The $K^\pm$ dN/dy distributions are reasonably well parameterized by two Gaussian distributions positioned symmetrically around $y = 0$,

$$\frac{dN}{dy} = \frac{A}{\sqrt{8\pi\sigma_y^2}}\left\{e^{-\frac{1}{2}\left(\frac{y+\mu_y}{\sigma_y}\right)^2} + e^{-\frac{1}{2}\left(\frac{y-\mu_y}{\sigma_y}\right)^2}\right\},$$

where $\pm\mu_y$ are the offsets from $y = 0$, σ_y is the common standard deviation, and A is the total yield. The y dependence of the $m_\perp$ distribution parameter T is given by

$$T(y) = \frac{T_0}{\cosh y/y_T}.$$

F.3 Protons

The transverse distributions of protons are characterized by an exponential behavior at large $p_\perp$ and a deficit from this exponential at small $p_\perp$. A difference between two exponentials in $m_\perp$,

$$\frac{1}{m_\perp}\frac{d^2N}{dy\,dm_\perp} = \frac{dN}{dy}\left\{\frac{1+\xi_2}{T_1(m_0+T_1)}e^{-(m_\perp - m_0)/T_1} + \frac{-\xi_2}{T_2(m_0+T_2)}e^{-(m_\perp - m_0)/T_2}\right\},$$

with T_1 describing the large $p_\perp$ behavior and T_2 describing the low $p_\perp$ deficit, is found to parameterize the distributions well. The parameter ξ_2 is the fraction of the total yield which the low $p_\perp$ deficit represents. The parameter T_1 was obtained by fitting the distributions for $m_\perp - m_0 > 0.3\,\mathrm{GeV}/c$, which corresponds to $p_\perp > 0.8\,\mathrm{GeV}/c$.

The proton dN/dy distributions are reasonably well parameterized by two Gaussian distributions positioned symmetrically around $y = 0$,

$$\frac{dN}{dy} = \frac{A}{\sqrt{8\pi\sigma_y^2}}\left\{e^{-\frac{1}{2}\left(\frac{y+\mu_y}{\sigma_y}\right)^2} + e^{-\frac{1}{2}\left(\frac{y-\mu_y}{\sigma_y}\right)^2}\right\},$$

where $\pm\mu_y$ are the offsets from $y = 0$ and σ_y is the common standard deviation. The parameter A gives the total area under the distributions if extended to $\pm\infty$. However, these distributions and parameterizations only extend to $y = 2.5$. The y dependence of the $m_\perp$ distribution parameters are given by

$$T_1(y) = \frac{T_{1,0}}{\cosh y/y_{T_1}},$$

$$\xi_2(y) = \frac{\xi_{2,0}}{\cosh y/y_{\xi_2}},$$

and

$$T_2(y) = \frac{T_{2,0}}{\cosh y/y_{T_2}}.$$

F.4 Anti–protons

The $m_\perp$ distributions of $\overline{\mathrm{p}}$ are well described by a single exponential,

$$\frac{1}{m_\perp}\frac{d^2N}{dy\,dm_\perp} = \frac{dN/dy}{T(m_0+T)}e^{-(m_\perp - m_0)/T}.$$

The $\overline{\mathrm{p}}$ dN/dy distributions are reasonably well parameterized with a single Gaussian distribution centered at $y = 0$,

$$\frac{dN}{dy} = \frac{A}{\sqrt{2\pi\sigma_y^2}}e^{-\frac{1}{2}\left(\frac{y}{\sigma_y}\right)^2},$$

with standard deviation σ_y and total yield A. The y dependence of the $m_\perp$ distribution parameter T is given by

$$T(y) = \frac{T_0}{\cosh y/y_T}.$$

π^+ Centrality Bin 1

$m_\perp$ Distributions

y	dN/dy	T_1 (GeV/c)	ξ_2	T_2 (GeV/c)
-1.2		0.174±0.006		
-1.0	105±6	0.195±0.004		
-0.8	120.8±1.5	0.195±0.004	0.22±0.03	0.103±0.009
-0.6	131.2±1.5	0.199±0.004	0.21±0.03	0.093±0.008
-0.4	140.3±1.5	0.207±0.004	0.20±0.02	0.079±0.007
-0.2	147.0±1.9	0.210±0.004	0.27±0.02	0.086±0.005
0.0	152.9±2.4	0.203±0.004	0.23±0.02	0.084±0.006
0.2	151.4±1.7	0.208±0.004	0.25±0.02	0.084±0.006
0.4	144.6±2.3	0.213±0.004	0.27±0.02	0.088±0.006
0.6	137.5±1.7	0.210±0.004	0.24±0.02	0.090±0.007
0.8	132.2±1.5	0.207±0.003	0.22±0.02	0.095±0.007
1.0	125.5±1.4	0.206±0.004	0.24±0.02	0.092±0.006
1.2	117.4±1.3	0.202±0.004	0.25±0.02	0.089±0.006
1.4	104.4±1.2	0.202±0.004	0.30±0.02	0.095±0.005
1.6	94.0±1.1	0.197±0.005	0.28±0.03	0.092±0.006
1.8	80.6±1.0	0.193±0.006	0.29±0.03	0.088±0.006
2.0	65.7±1.1	0.181±0.008	0.25±0.04	0.081±0.009
2.2	53.5±1.0	0.174±0.010	0.26±0.05	0.080±0.010
2.4	41.7±1.0	0.166±0.015	0.28±0.07	0.080±0.013
2.6	30.4±0.8	0.141±0.025	0.15±0.07	0.061±0.022
2.8	22.3±0.7			
3.0	15.6±1.2			
3.2	9.7±0.6			
3.4	5.0±0.5			

Rapidity Distributions

A	563.7±1.8
σ_y	1.47±0.00
$T_{1,0}$	0.208±0.001 GeV/c
y_{T_1}	3.99±0.34
$T_{2,0}$	0.089±0.002 GeV/c
$\xi_{2,0}$	0.246±0.006

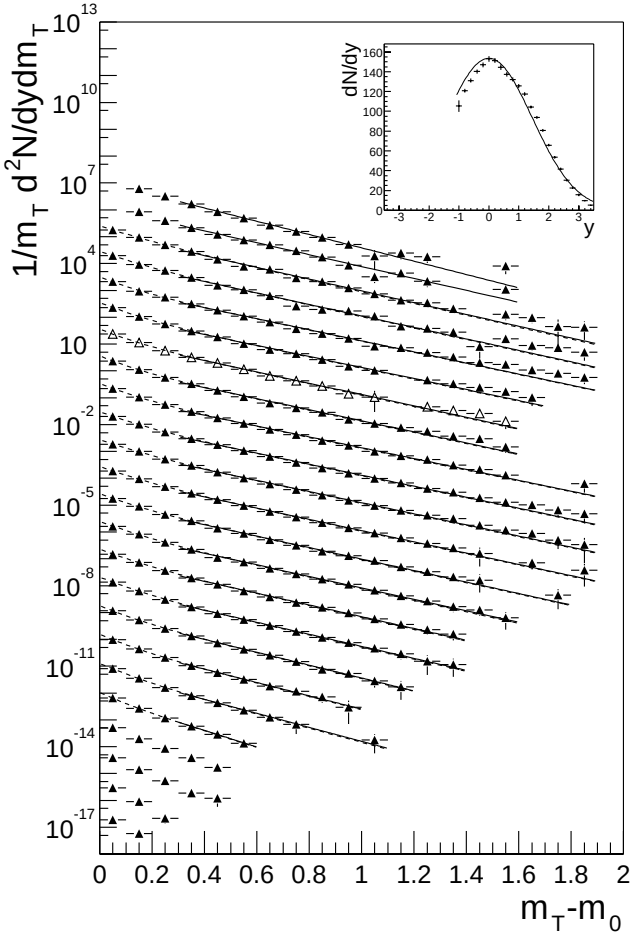

$m_\perp$ Distributions

y	dN/dy	T_1 (GeV/c)	ξ_2	T_2 (GeV/c)
-1.2		0.168±0.006		
-1.0	87±5	0.191±0.004		
-0.8	100.1±0.9	0.200±0.004	0.29±0.02	0.107±0.006
-0.6	105.7±1.0	0.202±0.003	0.25±0.02	0.095±0.006
-0.4	113.7±1.0	0.205±0.003	0.19±0.01	0.072±0.006
-0.2	121.6±1.1	0.212±0.003	0.27±0.02	0.085±0.004
0.0	124.1±1.1	0.211±0.004	0.29±0.02	0.089±0.004
0.2	123.5±1.1	0.216±0.004	0.29±0.02	0.087±0.004
0.4	117.6±1.2	0.214±0.004	0.29±0.02	0.088±0.005
0.6	112.6±1.1	0.208±0.003	0.26±0.02	0.091±0.005
0.8	107.9±2.8	0.208±0.003	0.26±0.02	0.093±0.005
1.0	102.0±0.8	0.206±0.003	0.26±0.02	0.089±0.004
1.2	94.1±0.8	0.201±0.003	0.26±0.02	0.088±0.004
1.4	84.5±0.8	0.200±0.004	0.30±0.02	0.094±0.004
1.6	76.5±0.7	0.194±0.004	0.27±0.02	0.090±0.005
1.8	65.9±0.7	0.188±0.005	0.27±0.02	0.084±0.005
2.0	55.1±0.7	0.183±0.007	0.26±0.03	0.080±0.006
2.2	44.5±0.8	0.170±0.009	0.22±0.04	0.074±0.009
2.4	34.5±0.7	0.160±0.014	0.24±0.07	0.078±0.013
2.6	26.5±0.6	0.147±0.018	0.22±0.07	0.071±0.016
2.8	18.4±0.7	0.100±0.026	0.3±0.4	0.15±0.07
3.0	12.5±1.8			
3.2	8.0±0.4			
3.4	4.2±0.5			

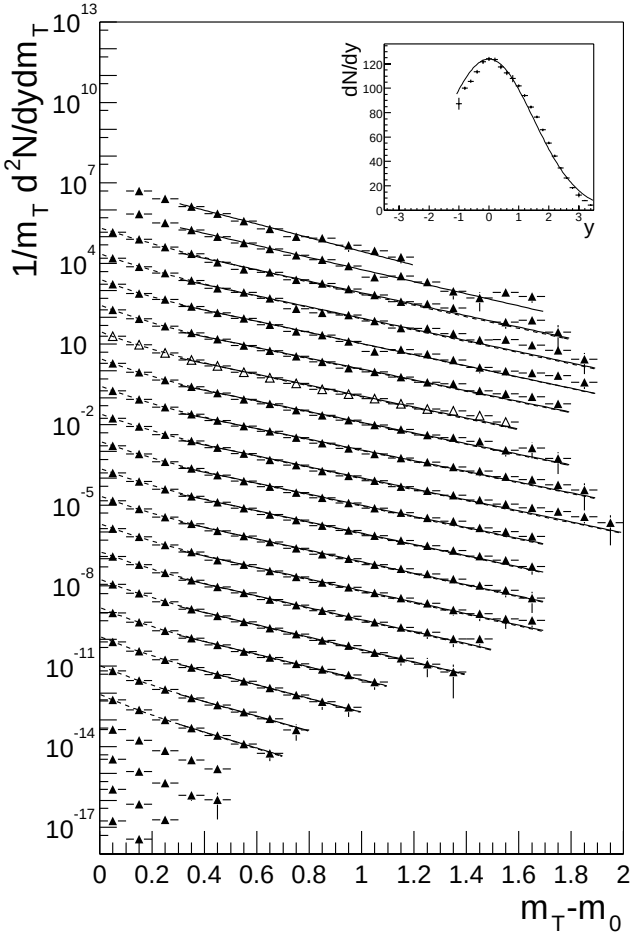

Rapidity Distributions

A	466.1±1.3
σ_y	1.51±0.00
$T_{1,0}$	0.211±0.001 GeV/c
y_{T_1}	3.38±0.19
$T_{2,0}$	0.089±0.001 GeV/c
$\xi_{2,0}$	0.262±0.005

π^+ Centrality Bin 3

$m_\perp$ Distributions

y	dN/dy	T_1 (GeV/c)	ξ_2	T_2 (GeV/c)
-1.2		0.180±0.005		
-1.0	66±4	0.200±0.004		
-0.8	74.2±0.6	0.196±0.003	0.27±0.02	0.102±0.005
-0.6	77.9±0.6	0.199±0.003	0.24±0.02	0.090±0.005
-0.4	83.6±0.6	0.207±0.003	0.20±0.01	0.070±0.005
-0.2	88.6±0.6	0.211±0.003	0.26±0.01	0.082±0.003
0.0	91.0±0.6	0.205±0.003	0.25±0.01	0.083±0.004
0.2	90.5±0.7	0.205±0.003	0.24±0.01	0.078±0.004
0.4	86.5±0.7	0.207±0.003	0.26±0.01	0.082±0.004
0.6	82.6±0.7	0.204±0.003	0.26±0.02	0.087±0.004
0.8	78.7±0.6	0.205±0.003	0.28±0.01	0.091±0.004
1.0	74.6±0.6	0.204±0.003	0.27±0.01	0.087±0.004
1.2	69.8±2.9	0.202±0.003	0.26±0.01	0.085±0.004
1.4	62.8±1.0	0.201±0.004	0.31±0.02	0.091±0.004
1.6	56.5±0.5	0.191±0.004	0.26±0.02	0.086±0.005
1.8	49.2±0.5	0.188±0.005	0.27±0.02	0.081±0.005
2.0	41.4±0.5	0.182±0.006	0.27±0.02	0.079±0.005
2.2	33.9±0.4	0.171±0.008	0.26±0.03	0.079±0.007
2.4	26.3±0.5	0.161±0.012	0.28±0.05	0.078±0.009
2.6	20.0±0.4	0.138±0.020	0.15±0.05	0.055±0.015
2.8	14.3±0.6			
3.0	10.1±0.4			
3.2	6.2±0.4			
3.4	3.1±0.6			

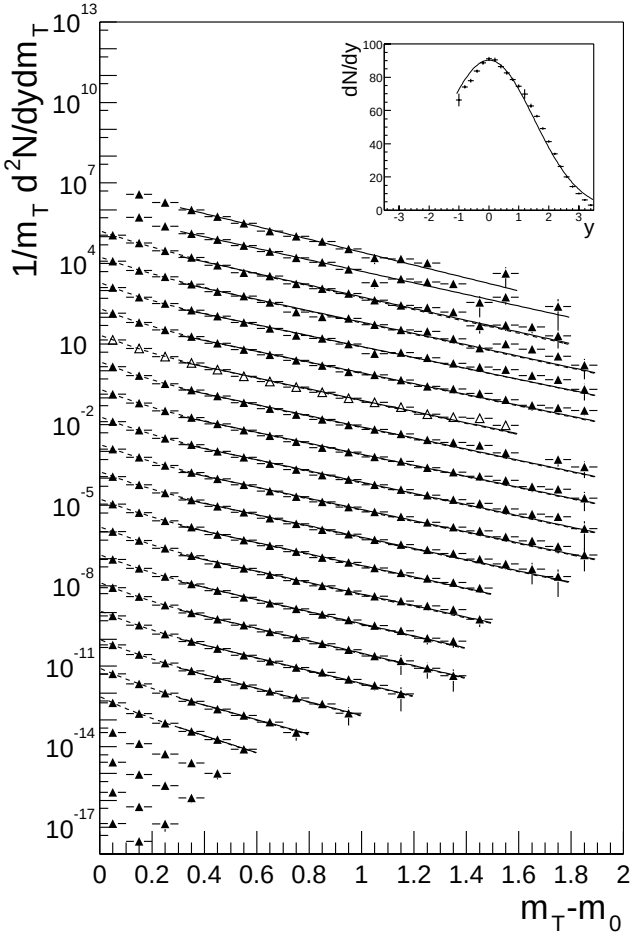

Rapidity Distributions

A	345.6±0.9
σ_y	1.54±0.00
$T_{1,0}$	0.207±0.001 GeV/c
y_{T_1}	3.83±0.23
$T_{2,0}$	0.084±0.001 GeV/c
$\xi_{2,0}$	0.255±0.004

$m_\perp$ Distributions

y	dN/dy	T_1 (GeV/c)	ξ_2	T_2 (GeV/c)
-1.2		0.181±0.005		
-1.0	45.9±2.6	0.195±0.004		
-0.8	51.8±0.4	0.202±0.003	0.31±0.02	0.099±0.004
-0.6	53.8±0.4	0.198±0.003	0.24±0.02	0.085±0.005
-0.4	56.8±0.4	0.204±0.003	0.20±0.01	0.068±0.005
-0.2	60.2±0.9	0.208±0.003	0.26±0.01	0.078±0.004
0.0	62.2±0.4	0.209±0.003	0.29±0.01	0.085±0.003
0.2	62.1±0.4	0.208±0.003	0.29±0.01	0.086±0.003
0.4	59.5±0.5	0.205±0.003	0.28±0.01	0.084±0.004
0.6	56.8±0.5	0.203±0.003	0.27±0.01	0.084±0.004
0.8	54.5±3.1	0.201±0.003	0.27±0.02	0.085±0.004
1.0	52±8	0.199±0.003	0.26±0.01	0.083±0.004
1.2	47.9±0.5	0.198±0.003	0.26±0.02	0.085±0.004
1.4	43.5±0.4	0.198±0.004	0.32±0.02	0.092±0.004
1.6	39.3±0.4	0.188±0.005	0.28±0.02	0.087±0.005
1.8	34.72±0.33	0.187±0.005	0.29±0.02	0.083±0.005
2.0	29.20±0.34	0.177±0.006	0.26±0.03	0.076±0.006
2.2	23.84±0.33	0.167±0.009	0.26±0.04	0.076±0.007
2.4	18.94±0.31	0.150±0.012	0.20±0.05	0.070±0.011
2.6	14.44±0.31	0.132±0.022	0.12±0.05	0.055±0.020
2.8	10.5±0.6			
3.0	7.4±0.6			
3.2	4.4±0.4			
3.4	3.07±0.34			

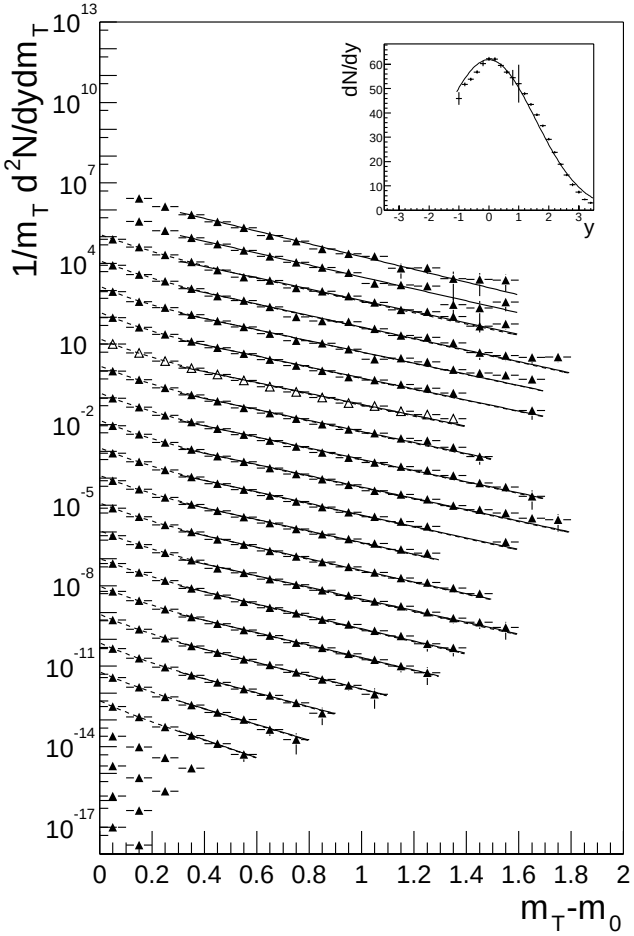

Rapidity Distributions

A	243.2±0.7
σ_y	1.58±0.00
$T_{1,0}$	0.207±0.001 GeV/c
y_{T_1}	3.46±0.20
$T_{2,0}$	0.084±0.001 GeV/c
$\xi_{2,0}$	0.266±0.004

π^+ Centrality Bin 5

$m_\perp$ Distributions

y	dN/dy	T_1 (GeV/c)	ξ_2	T_2 (GeV/c)
-1.2		0.179±0.007		
-1.0	31.1±1.8	0.199±0.004		
-0.8	35.15±0.32	0.206±0.004	0.33±0.02	0.100±0.004
-0.6	36.24±0.33	0.197±0.004	0.23±0.02	0.080±0.005
-0.4	38.42±0.33	0.203±0.003	0.18±0.01	0.060±0.006
-0.2	40.77±0.34	0.213±0.003	0.29±0.01	0.082±0.004
0.0	42.31±0.34	0.208±0.004	0.29±0.01	0.083±0.004
0.2	41.9±0.4	0.209±0.004	0.30±0.02	0.085±0.004
0.4	40.38±0.35	0.206±0.004	0.29±0.02	0.082±0.004
0.6	38.39±0.33	0.197±0.003	0.26±0.02	0.081±0.004
0.8	36.60±0.32	0.200±0.003	0.28±0.02	0.084±0.004
1.0	35.07±0.31	0.198±0.004	0.26±0.02	0.082±0.004
1.2	32.96±0.30	0.196±0.004	0.27±0.02	0.083±0.004
1.4	29.83±0.28	0.195±0.005	0.31±0.02	0.091±0.005
1.6	27.24±0.28	0.186±0.005	0.27±0.02	0.084±0.006
1.8	23.92±0.29	0.183±0.006	0.28±0.03	0.083±0.006
2.0	20.39±0.28	0.172±0.009	0.25±0.03	0.077±0.007
2.2	16.85±0.27	0.164±0.012	0.24±0.05	0.076±0.010
2.4	13.2±0.4			
2.6	10.30±0.33			
2.8	7.7±0.4			
3.0	5.4±0.5			
3.2	3.35±0.33			
3.4	2.48±0.32			

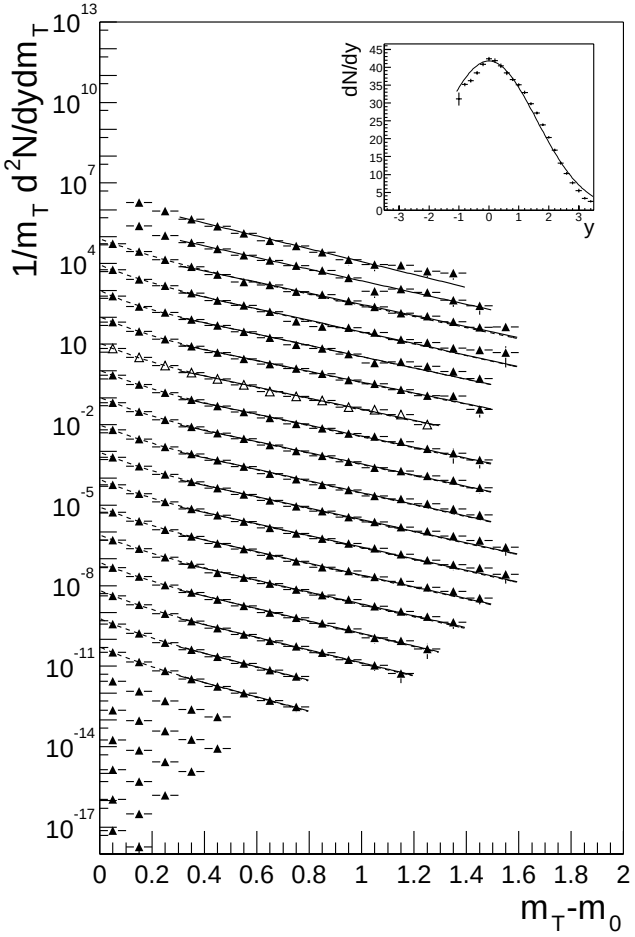

Rapidity Distributions

A	168.6±0.6
σ_y	1.62±0.01
$T_{1,0}$	0.207±0.001 GeV/c
y_{T_1}	3.33±0.23
$T_{2,0}$	0.083±0.001 GeV/c
$\xi_{2,0}$	0.265±0.004

$m_\perp$ Distributions

y	dN/dy	T_1 (GeV/c)	ξ_2	T_2 (GeV/c)
-1.2		0.190±0.007		
-1.0	19.2±1.1	0.200±0.005		
-0.8	21.77±0.21	0.196±0.004	0.29±0.02	0.094±0.005
-0.6	22.45±0.20	0.195±0.004	0.21±0.02	0.072±0.005
-0.4	23.72±0.21	0.197±0.003	0.18±0.01	0.056±0.005
-0.2	25.06±0.21	0.202±0.004	0.26±0.01	0.076±0.004
0.0	25.81±0.21	0.193±0.004	0.23±0.02	0.077±0.004
0.2	25.88±0.21	0.193±0.004	0.25±0.02	0.080±0.004
0.4	25.00±0.22	0.194±0.004	0.26±0.02	0.081±0.004
0.6	23.99±0.21	0.192±0.004	0.26±0.02	0.081±0.005
0.8	22.84±0.20	0.198±0.004	0.30±0.02	0.087±0.004
1.0	21.74±0.19	0.196±0.004	0.28±0.02	0.085±0.004
1.2	20.28±0.18	0.188±0.004	0.25±0.02	0.083±0.005
1.4	18.52±0.18	0.190±0.005	0.32±0.03	0.090±0.005
1.6	17.21±0.17	0.184±0.005	0.28±0.03	0.086±0.006
1.8	15.35±0.18	0.176±0.006	0.25±0.03	0.081±0.007
2.0	13.13±0.17	0.165±0.009	0.22±0.03	0.073±0.008
2.2	10.81±0.18	0.157±0.014	0.24±0.05	0.076±0.011
2.4	8.67±0.24			
2.6	6.8±0.6			
2.8	5.2±0.5			
3.0	3.8±0.4			
3.2	2.7±0.4			
3.4				

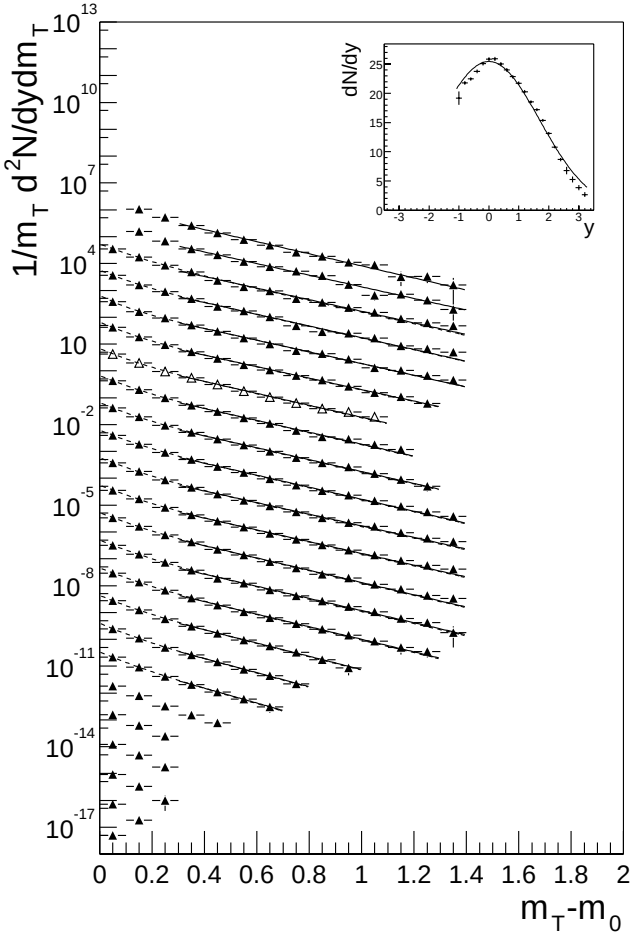

Rapidity Distributions

A	109.1±0.5
σ_y	1.72±0.01
$T_{1,0}$	0.198±0.001 GeV/c
y_{T_1}	-4.0±0.4
$T_{2,0}$	0.081±0.001 GeV/c
$\xi_{2,0}$	0.244±0.005

π^- Centrality Bin 1

$m_\perp$ Distributions

y	dN/dy	T_1 (GeV/c)	ξ_2	T_2 (GeV/c)
-1.2		0.194±0.003		
-1.0	112±7	0.201±0.002		
-0.8	136±8	0.203±0.002	0.24±0.01	0.082±0.005
-0.6	147.2±1.4	0.208±0.002	0.27±0.01	0.083±0.003
-0.4	158.9±1.4	0.211±0.002	0.26±0.01	0.084±0.003
-0.2	162.7±1.5	0.209±0.002	0.24±0.01	0.085±0.004
0.0	163.5±1.6	0.210±0.003	0.26±0.01	0.086±0.004
0.2	162.7±1.4	0.209±0.002	0.25±0.01	0.080±0.004
0.4	154.6±1.4	0.213±0.002	0.28±0.01	0.089±0.004
0.6	149.4±1.5	0.208±0.002	0.28±0.01	0.091±0.004
0.8	144.8±1.4	0.203±0.002	0.27±0.01	0.089±0.004
1.0	136.8±1.2	0.200±0.002	0.26±0.01	0.082±0.004
1.2	126.8±1.1	0.193±0.003	0.24±0.01	0.077±0.004
1.4	113.5±0.9	0.188±0.002	0.26±0.01	0.079±0.003
1.6	99.7±0.8	0.184±0.002	0.27±0.01	0.075±0.003
1.8	84.0±0.7	0.174±0.002	0.26±0.01	0.072±0.003
2.0	67.7±0.6	0.160±0.003	0.23±0.02	0.070±0.005
2.2	53.2±0.6	0.153±0.004	0.28±0.02	0.073±0.005
2.4	40.3±0.5	0.152±0.008	0.40±0.03	0.076±0.005
2.6	29.7±0.5			
2.8	19.8±1.0			
3.0	13.3±0.6			
3.2	8.37±0.31			
3.4	5.19±0.32			

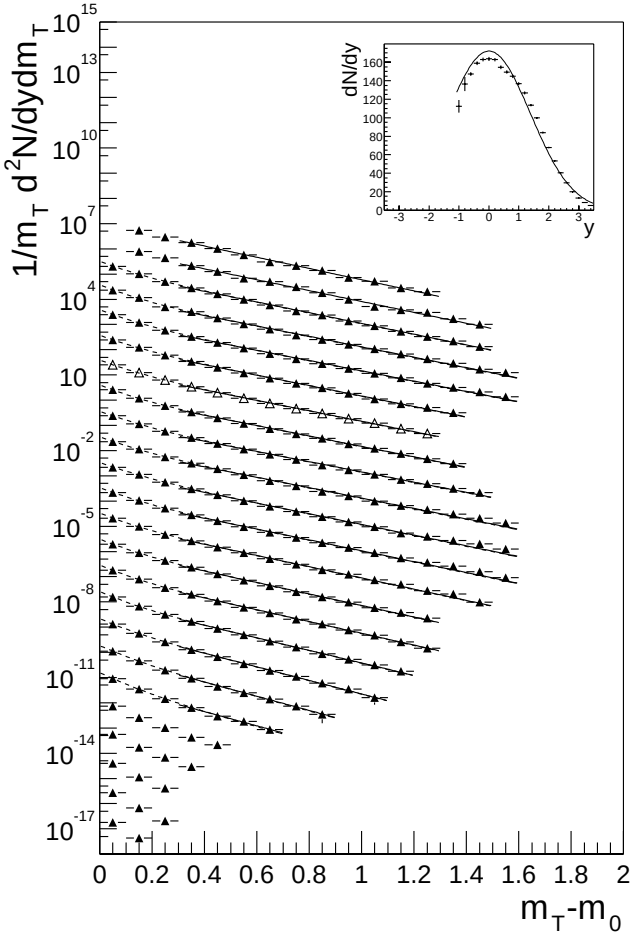

Rapidity Distributions

A	606.6±1.4
σ_y	1.41±0.00
$T_{1,0}$	0.213±0.001 GeV/c
y_{T_1}	2.73±0.06
$T_{2,0}$	0.081±0.001 GeV/c
$\xi_{2,0}$	0.261±0.003

$m_\perp$ Distributions

y	dN/dy	T_1 (GeV/c)	ξ_2	T_2 (GeV/c)
-1.2		0.195±0.002		
-1.0	91±5	0.204±0.002		
-0.8	107.6±0.8	0.207±0.002	0.27±0.01	0.085±0.003
-0.6	119.3±0.9	0.205±0.002	0.25±0.01	0.075±0.003
-0.4	128.3±0.9	0.208±0.002	0.26±0.01	0.080±0.003
-0.2	130.7±0.9	0.212±0.002	0.27±0.01	0.085±0.003
0.0	132.2±0.9	0.209±0.002	0.27±0.01	0.085±0.003
0.2	131.9±0.9	0.210±0.002	0.28±0.01	0.084±0.003
0.4	126.1±1.0	0.210±0.002	0.27±0.01	0.086±0.003
0.6	121.6±0.9	0.207±0.002	0.28±0.01	0.085±0.003
0.8	116.5±0.8	0.205±0.002	0.28±0.01	0.084±0.003
1.0	110.0±0.8	0.201±0.002	0.27±0.01	0.080±0.003
1.2	101.9±0.8	0.196±0.002	0.26±0.01	0.078±0.003
1.4	92.0±0.6	0.192±0.002	0.28±0.01	0.080±0.003
1.6	81.2±0.6	0.186±0.002	0.29±0.01	0.078±0.003
1.8	69.5±0.5	0.177±0.002	0.28±0.01	0.075±0.003
2.0	57.3±0.5	0.168±0.003	0.29±0.01	0.072±0.003
2.2	45.4±0.4	0.154±0.004	0.31±0.02	0.071±0.004
2.4	34.9±0.4	0.147±0.007	0.40±0.03	0.072±0.004
2.6	26.2±0.4			
2.8	18.4±0.4			
3.0	12.5±0.5			
3.2	7.98±0.25			
3.4				

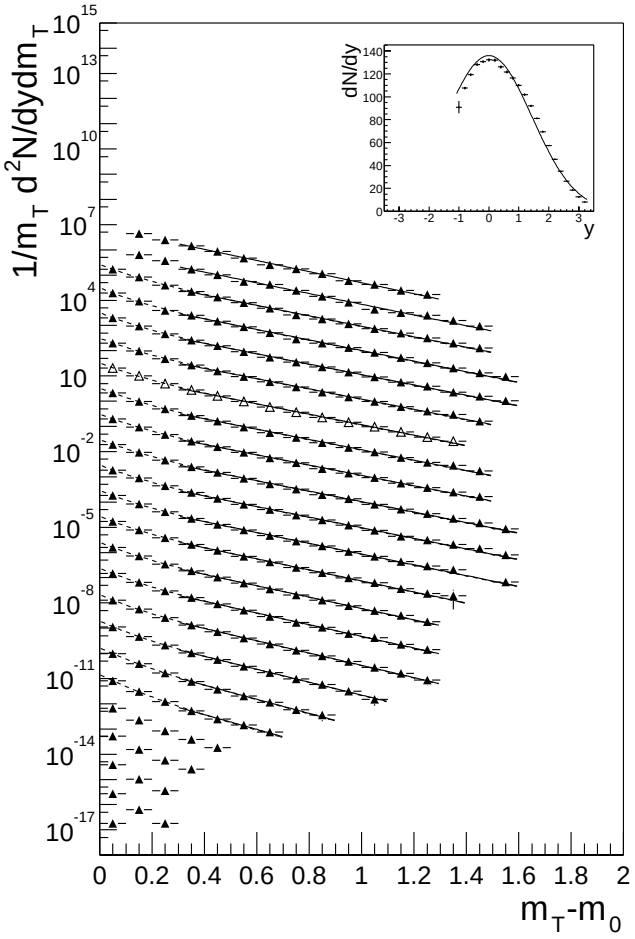

Rapidity Distributions

A	495.8±0.9
σ_y	1.46±0.00
$T_{1,0}$	0.212±0.001 GeV/c
y_{T_1}	2.92±0.06
$T_{2,0}$	0.080±0.001 GeV/c
$\xi_{2,0}$	0.274±0.002

π^- Centrality Bin 3

$m_\perp$ Distributions

y	dN/dy	T_1 (GeV/c)	ξ_2	T_2 (GeV/c)
-1.2		0.195±0.002		
-1.0	68±4	0.203±0.002		
-0.8	80.1±0.5	0.203±0.001	0.24±0.01	0.080±0.003
-0.6	87.8±0.6	0.204±0.001	0.27±0.01	0.079±0.002
-0.4	94.1±0.6	0.208±0.001	0.28±0.01	0.079±0.002
-0.2	95.8±0.6	0.210±0.002	0.28±0.01	0.083±0.002
0.0	96.8±0.6	0.207±0.002	0.27±0.01	0.082±0.003
0.2	96.3±0.6	0.211±0.002	0.30±0.01	0.084±0.002
0.4	92.5±0.6	0.211±0.002	0.30±0.01	0.088±0.002
0.6	88.9±0.6	0.205±0.002	0.29±0.01	0.086±0.003
0.8	85.2±0.5	0.203±0.002	0.28±0.01	0.082±0.002
1.0	80.7±0.5	0.202±0.002	0.28±0.01	0.081±0.002
1.2	75.0±0.5	0.194±0.002	0.25±0.01	0.075±0.003
1.4	67.9±0.4	0.188±0.002	0.26±0.01	0.077±0.003
1.6	60.3±0.4	0.183±0.002	0.28±0.01	0.077±0.003
1.8	51.98±0.34	0.176±0.002	0.27±0.01	0.072±0.003
2.0	43.09±0.30	0.166±0.002	0.29±0.01	0.070±0.003
2.2	35.07±0.26	0.158±0.003	0.34±0.01	0.071±0.003
2.4	27.56±0.22	0.158±0.004	0.45±0.02	0.071±0.002
2.6	21.42±0.20	0.146±0.007	0.43±0.02	0.060±0.002
2.8	15.82±0.16	0.137±0.009	0.5±0.4	0.058±0.002
3.0	11.13±0.20			
3.2	6.72±0.35			
3.4	4.20±0.17			

Rapidity Distributions

A	370.0±0.6
σ_y	1.49±0.00
$T_{1,0}$	0.211±0.001 GeV/c
y_{T_1}	2.88±0.05
$T_{2,0}$	0.075±0.001 GeV/c
$\xi_{2,0}$	0.282±0.002

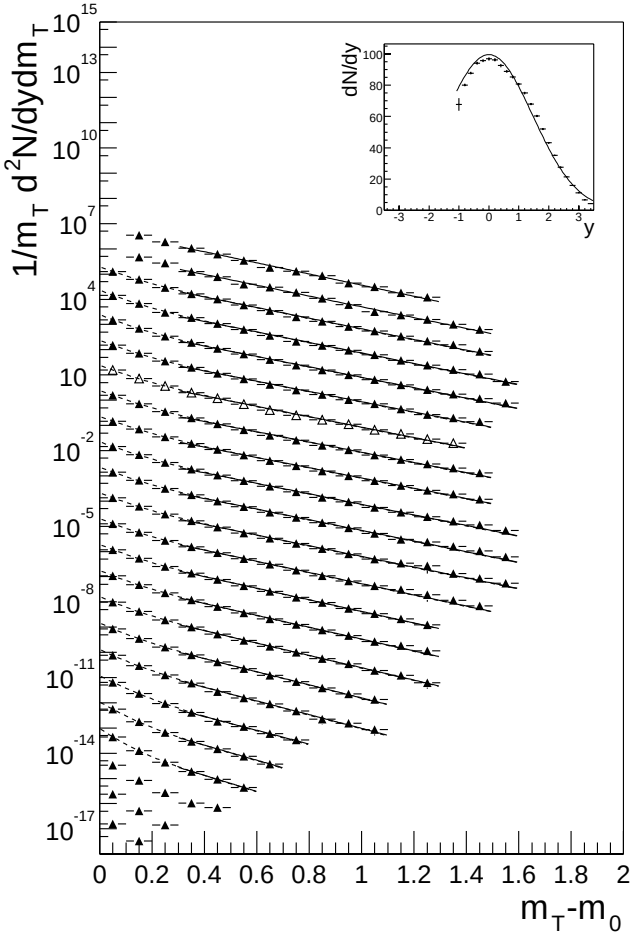

$m_\perp$ Distributions

y	dN/dy	T_1 (GeV/c)	ξ_2	T_2 (GeV/c)
-1.2		0.198±0.003		
-1.0	46.8±2.8	0.206±0.002		
-0.8	55.2±0.4	0.201±0.002	0.25±0.01	0.078±0.003
-0.6	60.6±0.4	0.204±0.002	0.28±0.01	0.078±0.002
-0.4	63.6±0.4	0.206±0.002	0.28±0.01	0.079±0.002
-0.2	64.9±0.4	0.206±0.002	0.28±0.01	0.083±0.002
0.0	65.8±0.4	0.206±0.002	0.29±0.01	0.083±0.002
0.2	66.1±0.4	0.206±0.002	0.28±0.01	0.082±0.002
0.4	63.7±0.4	0.204±0.002	0.28±0.01	0.086±0.003
0.6	61.1±0.4	0.201±0.002	0.28±0.01	0.083±0.002
0.8	58.6±0.4	0.202±0.002	0.30±0.01	0.081±0.002
1.0	55.14±0.33	0.202±0.002	0.29±0.01	0.078±0.002
1.2	51.28±0.31	0.196±0.002	0.27±0.01	0.076±0.003
1.4	46.74±0.28	0.187±0.002	0.26±0.01	0.078±0.003
1.6	41.88±0.26	0.181±0.002	0.27±0.01	0.075±0.003
1.8	36.67±0.26	0.173±0.002	0.27±0.01	0.072±0.003
2.0	30.85±0.24	0.163±0.003	0.29±0.01	0.069±0.003
2.2	25.54±0.21	0.154±0.003	0.31±0.01	0.067±0.003
2.4	20.46±0.18	0.144±0.006	0.5±0.4	0.079±0.001
2.6	16.01±0.17			
2.8	12.09±0.14			
3.0	8.31±0.12			
3.2	5.30±0.10			
3.4	3.18±0.12			

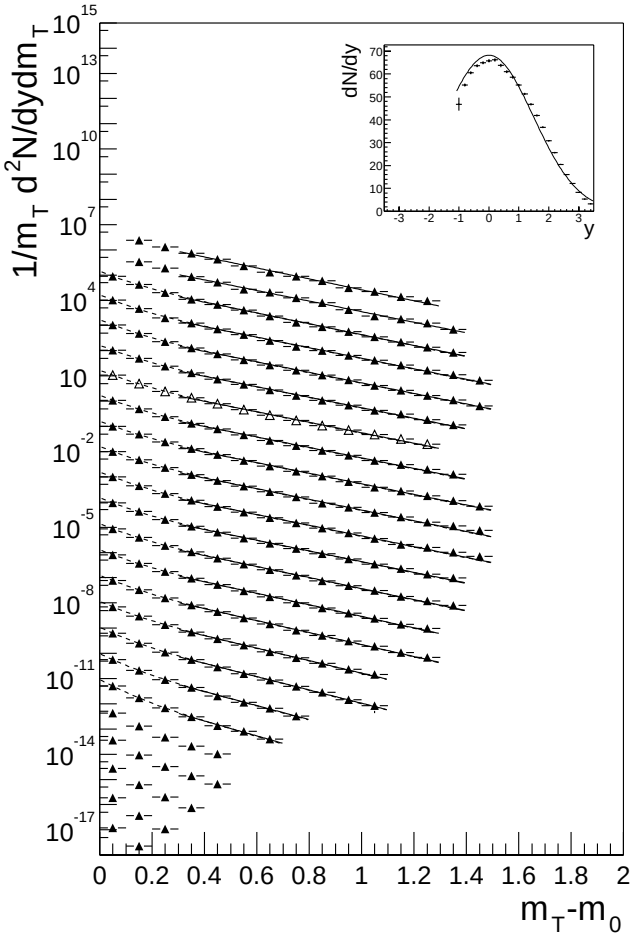

Rapidity Distributions

A	256.5±0.4
σ_y	1.51±0.00
$T_{1,0}$	0.209±0.001 GeV/c
y_{T_1}	2.93±0.06
$T_{2,0}$	0.079±0.001 GeV/c
$\xi_{2,0}$	0.279±0.002

π^- Centrality Bin 5

$m_\perp$ Distributions

y	dN/dy	T_1 (GeV/c)	ξ_2	T_2 (GeV/c)
-1.2		0.189±0.003		
-1.0	32.2±2.0	0.202±0.003		
-0.8	38.2±2.3	0.200±0.002	0.27±0.01	0.079±0.003
-0.6	40.75±0.30	0.200±0.002	0.27±0.01	0.074±0.003
-0.4	43.30±0.30	0.202±0.002	0.28±0.01	0.078±0.003
-0.2	43.84±0.30	0.202±0.002	0.27±0.01	0.081±0.003
0.0	44.35±0.32	0.199±0.003	0.26±0.01	0.079±0.003
0.2	44.63±0.31	0.200±0.002	0.27±0.01	0.078±0.003
0.4	43.03±0.31	0.199±0.002	0.27±0.01	0.083±0.003
0.6	41.43±0.29	0.198±0.002	0.27±0.01	0.081±0.003
0.8	39.44±0.28	0.199±0.002	0.29±0.01	0.079±0.003
1.0	37.56±0.26	0.196±0.002	0.27±0.01	0.077±0.003
1.2	35.12±0.26	0.190±0.003	0.26±0.01	0.075±0.003
1.4	32.26±0.24	0.187±0.003	0.27±0.01	0.078±0.003
1.6	29.18±0.24	0.183±0.003	0.30±0.01	0.079±0.003
1.8	25.80±0.21	0.172±0.003	0.27±0.01	0.071±0.004
2.0	22.14±0.20	0.162±0.003	0.27±0.01	0.067±0.004
2.2	18.56±0.17	0.149±0.004	0.27±0.02	0.062±0.004
2.4	14.84±0.15	0.142±0.007	0.5±0.4	0.081±0.002
2.6	11.75±0.15			
2.8	8.50±0.23			
3.0	6.14±0.13			
3.2	4.00±0.10			
3.4				

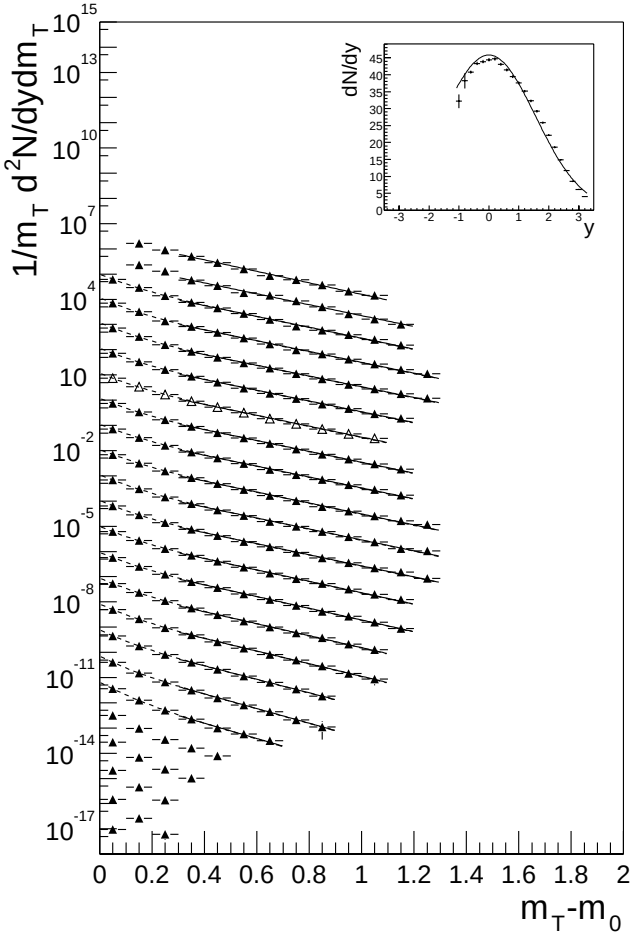

Rapidity Distributions

A	179.8±0.4
σ_y	1.58±0.00
$T_{1,0}$	0.204±0.001 GeV/c
y_{T_1}	3.03±0.09
$T_{2,0}$	0.078±0.001 GeV/c
$\xi_{2,0}$	0.272±0.003

$m_\perp$ Distributions

y	dN/dy	T_1 (GeV/c)	ξ_2	T_2 (GeV/c)
-1.2		0.187±0.004		
-1.0	19.9±1.3	0.200±0.003		
-0.8	23.6±1.4	0.200±0.003	0.28±0.01	0.082±0.003
-0.6	24.8±1.4	0.195±0.002	0.26±0.01	0.074±0.003
-0.4	26.74±0.18	0.198±0.002	0.27±0.01	0.076±0.003
-0.2	26.96±0.20	0.196±0.003	0.25±0.01	0.079±0.003
0.0	27.18±0.22	0.191±0.003	0.23±0.01	0.076±0.003
0.2	27.39±0.22	0.189±0.003	0.23±0.01	0.075±0.003
0.4	26.50±0.19	0.195±0.003	0.28±0.01	0.085±0.003
0.6	25.83±0.18	0.195±0.002	0.28±0.01	0.082±0.003
0.8	24.58±0.17	0.191±0.002	0.28±0.01	0.080±0.003
1.0	23.42±0.16	0.191±0.002	0.26±0.01	0.078±0.003
1.2	22.01±0.16	0.188±0.003	0.26±0.01	0.079±0.003
1.4	20.33±0.15	0.181±0.003	0.25±0.01	0.080±0.004
1.6	18.40±0.15	0.176±0.003	0.28±0.01	0.078±0.004
1.8	16.38±0.15	0.163±0.003	0.23±0.02	0.067±0.005
2.0	14.30±0.16	0.155±0.004	0.24±0.02	0.064±0.005
2.2	12.27±0.12	0.146±0.005	0.28±0.02	0.064±0.004
2.4	10.08±0.11	0.145±0.009	0.5±0.4	0.075±0.002
2.6	8.27±0.10			
2.8	6.14±0.15			
3.0	4.48±0.09			
3.2				
3.4				

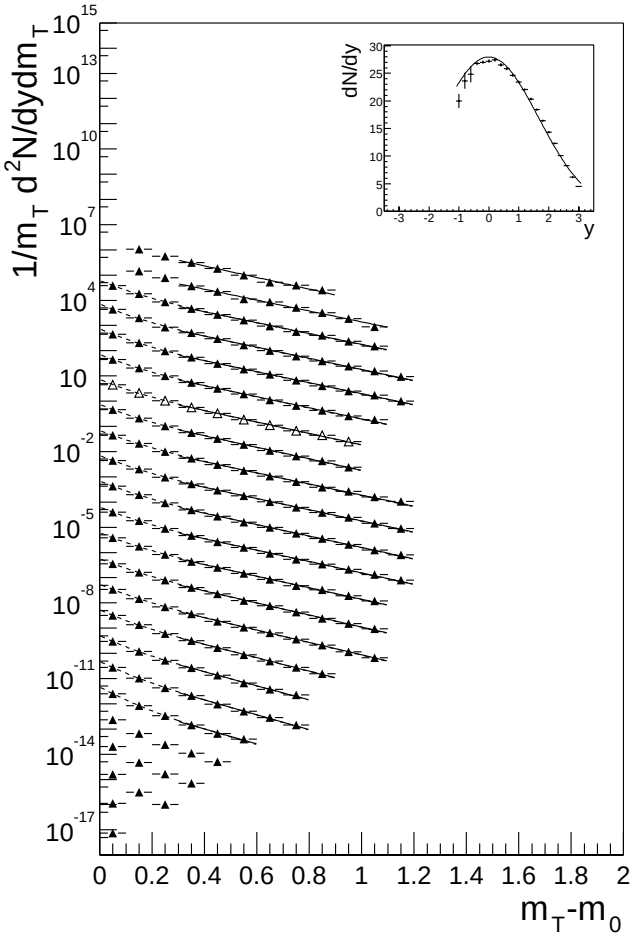

Rapidity Distributions

A	116.67±0.27
σ_y	1.67±0.00
$T_{1,0}$	0.199±0.001 GeV/c
y_{T_1}	3.03±0.10
$T_{2,0}$	0.077±0.001 GeV/c
$\xi_{2,0}$	0.260±0.003

K$^+$ Centrality Bin 1

$m_\perp$ Distributions

y	dN/dy	T (GeV/c)
-0.2		0.247±0.008
0.0	32.9±0.7	0.250±0.004
0.2	32.2±0.6	0.246±0.003
0.4	30.9±0.4	0.243±0.003
0.6	29.5±0.4	0.246±0.003
0.8	28.1±0.4	0.242±0.003
1.0	25.5±0.4	0.234±0.003
1.2	21.9±0.4	0.222±0.004
1.4	19.6±0.4	0.221±0.004
1.6	16.4±0.4	0.198±0.005
1.8	12.5±0.5	0.185±0.007
2.0	8.2±0.4	0.163±0.011
2.2	5.4±0.6	0.170±0.027
2.4	3.1±1.1	
2.6	1.3±0.4	
2.8	1.3±1.1	

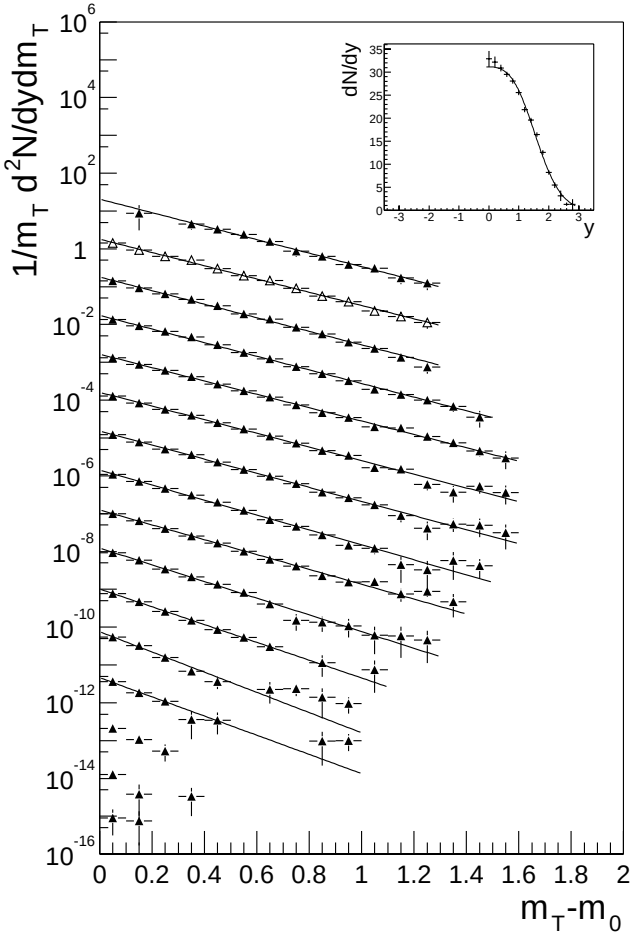

Rapidity Distributions

A	102.1±0.7
μ_y	0.77±0.01
σ_y	0.85±0.02
T_0	0.251±0.002 GeV/c
y_T	2.37±0.09

K^+ Centrality Bin 2

$m_\perp$ Distributions

y	dN/dy	T (GeV/c)
-0.2		0.225±0.006
0.0	25.2±0.5	0.240±0.004
0.2	24.4±0.4	0.245±0.003
0.4	24.13±0.31	0.242±0.002
0.6	22.95±0.28	0.243±0.003
0.8	21.95±0.29	0.245±0.003
1.0	20.24±0.30	0.234±0.003
1.2	17.71±0.31	0.231±0.004
1.4	15.62±0.30	0.225±0.004
1.6	13.01±0.30	0.203±0.005
1.8	9.97±0.32	0.188±0.007
2.0	6.68±0.33	0.184±0.012
2.2	4.8±0.5	0.195±0.024
2.4	3.2±0.6	
2.6	2.3±0.5	
2.8		

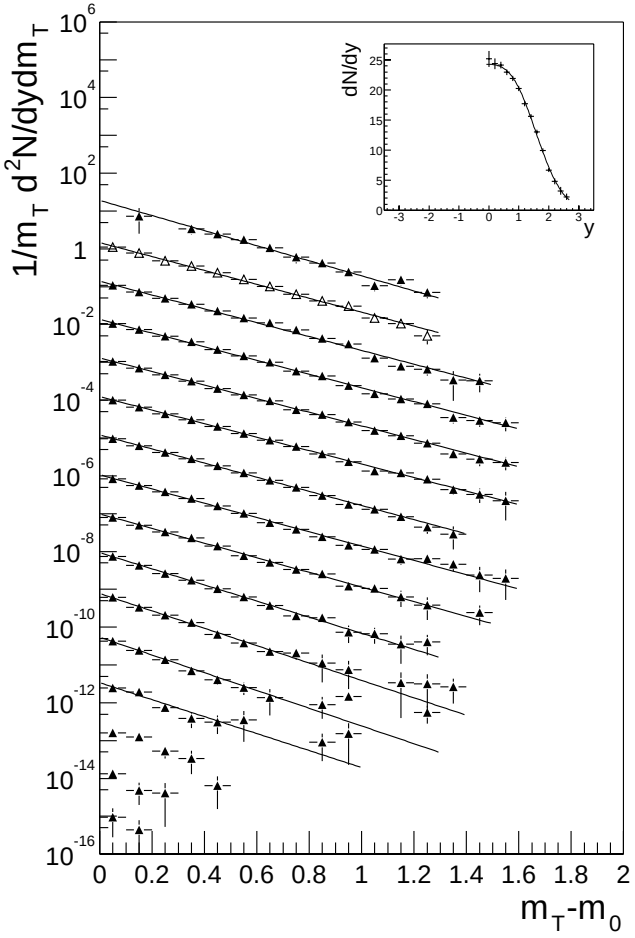

Rapidity Distributions

A	81.1±0.6
μ_y	0.79±0.01
σ_y	0.87±0.02
T_0	0.246±0.001 GeV/c
y_T	2.85±0.14

K^+ Centrality Bin 3

$m_\perp$ Distributions

y	dN/dy	T (GeV/c)
-0.2		0.247±0.007
0.0	18.0±0.4	0.242±0.004
0.2	17.45±0.27	0.236±0.003
0.4	17.17±0.21	0.235±0.002
0.6	16.29±0.20	0.239±0.002
0.8	15.74±0.20	0.239±0.003
1.0	14.50±0.21	0.225±0.003
1.2	12.77±0.21	0.221±0.003
1.4	11.42±0.22	0.212±0.004
1.6	9.57±0.23	0.198±0.005
1.8	7.19±0.21	0.183±0.006
2.0	5.12±0.21	0.186±0.011
2.2	3.08±0.28	0.175±0.022
2.4	2.8±0.6	
2.6	2.1±0.7	
2.8	1.6±0.4	
3.0		

Rapidity Distributions

A	58.4±0.4
μ_y	0.80±0.01
σ_y	0.88±0.02
T_0	0.243±0.001 GeV/c
y_T	2.59±0.11

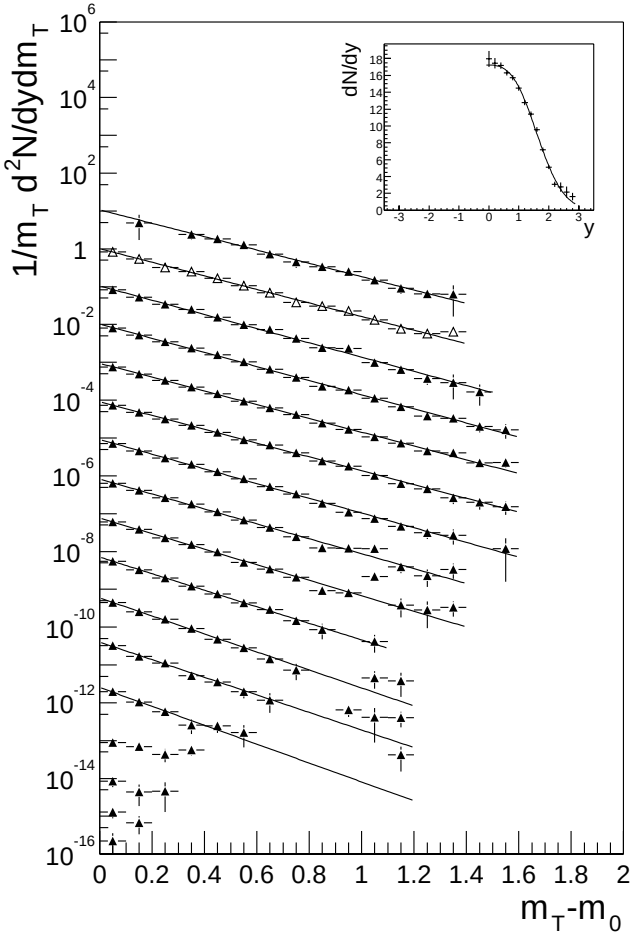

K^+ Centrality Bin 4

$m_\perp$ Distributions

y	dN/dy	T (GeV/c)
-0.2		0.223±0.007
0.0	11.84±0.27	0.232±0.004
0.2	11.33±0.20	0.228±0.003
0.4	11.28±0.16	0.235±0.003
0.6	10.78±0.15	0.234±0.003
0.8	10.34±0.15	0.230±0.003
1.0	9.56±0.16	0.225±0.003
1.2	8.32±0.16	0.215±0.004
1.4	7.38±0.17	0.205±0.005
1.6	6.31±0.19	0.188±0.006
1.8	4.66±0.16	0.171±0.007
2.0	3.31±0.21	0.169±0.012
2.2	2.21±0.21	0.182±0.028
2.4	1.73±0.34	
2.6		

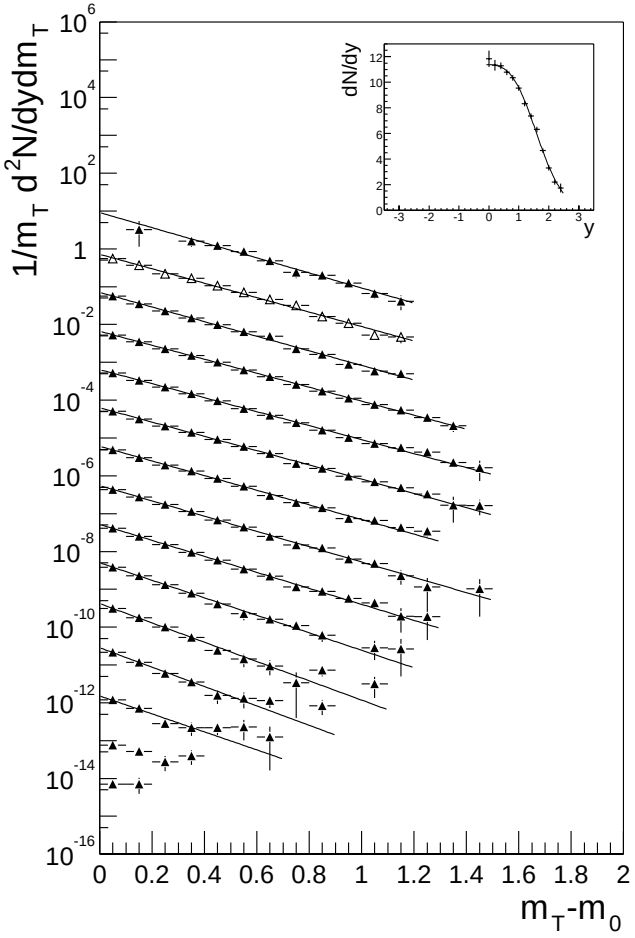

Rapidity Distributions

A	38.25±0.31
μ_y	0.80±0.01
σ_y	0.88±0.02
T_0	0.237±0.002 GeV/c
y_T	2.48±0.11

K$^+$ Centrality Bin 5

$m_\perp$ Distributions

y	dN/dy	T (GeV/c)
-0.2		0.244±0.019
0.0	7.80±0.23	0.218±0.005
0.2	7.22±0.15	0.212±0.004
0.4	7.02±0.12	0.216±0.003
0.6	6.74±0.12	0.219±0.003
0.8	6.47±0.11	0.219±0.004
1.0	6.08±0.12	0.210±0.004
1.2	5.52±0.13	0.207±0.005
1.4	5.01±0.13	0.206±0.006
1.6	4.32±0.14	0.202±0.007
1.8	3.06±0.17	0.184±0.011
2.0	1.99±0.16	0.167±0.019
2.2	1.0±0.4	
2.4	1.07±0.27	
2.6		
2.8		

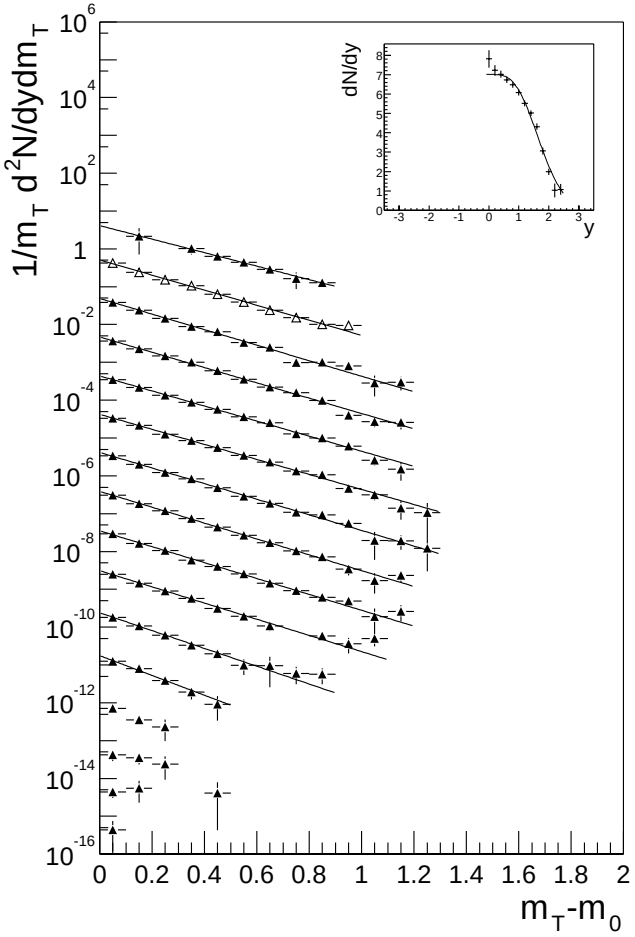

Rapidity Distributions

A	24.71±0.28
μ_y	0.83±0.01
σ_y	0.88±0.03
T_0	0.219±0.002 GeV/c
y_T	3.6±0.4

K^+ Centrality Bin 6

$m_\perp$ Distributions

y	dN/dy	T (GeV/c)
-0.2		0.235±0.025
0.0	4.09±0.16	0.206±0.007
0.2	4.11±0.12	0.214±0.006
0.4	3.98±0.08	0.210±0.004
0.6	3.85±0.08	0.209±0.004
0.8	3.70±0.07	0.207±0.004
1.0	3.51±0.08	0.213±0.005
1.2	3.27±0.08	0.205±0.005
1.4	2.93±0.09	0.191±0.006
1.6	2.50±0.08	0.188±0.008
1.8	1.84±0.10	0.158±0.010
2.0	1.16±0.15	
2.2	0.81±0.25	
2.4	3.3±1.5	

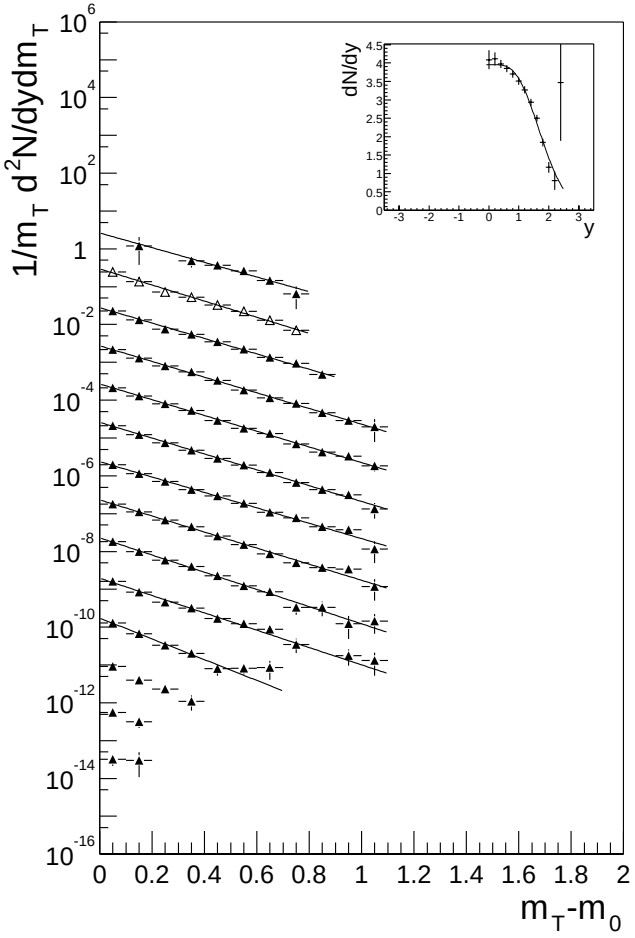

Rapidity Distributions

A	14.38±0.21
μ_y	0.87±0.01
σ_y	0.88±0.03
T_0	0.214±0.002 GeV/c
y_T	3.01±0.31

K^- Centrality Bin 1

$m_\perp$ Distributions

y	dN/dy	T (GeV/c)
-0.2		0.231±0.011
0.0	15.3±0.6	0.233±0.006
0.2	15.6±0.4	0.229±0.004
0.4	14.97±0.28	0.229±0.003
0.6	13.83±0.22	0.224±0.003
0.8	13.21±0.21	0.220±0.003
1.0	11.90±0.22	0.210±0.004
1.2	9.70±0.23	0.213±0.005
1.4	8.10±0.21	0.201±0.005
1.6	7.01±0.20	0.178±0.005
1.8	5.20±0.18	0.168±0.006
2.0	3.50±0.28	0.161±0.009
2.2	1.75±0.15	
2.4	0.9±0.4	
2.6	0.25±0.13	

Rapidity Distributions

A	45.68±0.35
μ_y	0.72±0.01
σ_y	0.80±0.01
T_0	0.233±0.002 GeV/c
y_T	2.25±0.09

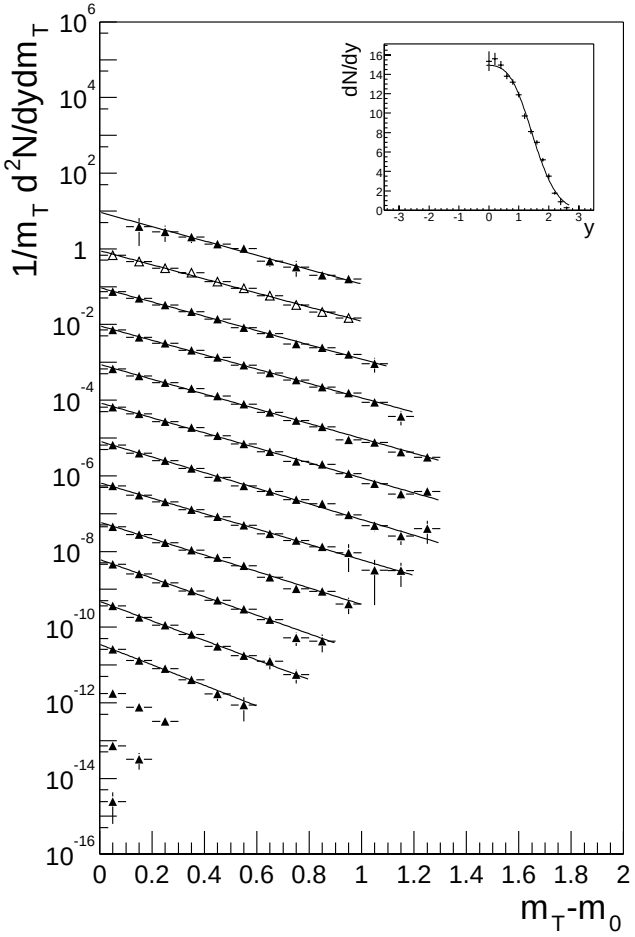

K^- Centrality Bin 2

$m_\perp$ Distributions

y	dN/dy	T (GeV/c)
-0.2		0.216±0.010
0.0	12.2±0.4	0.234±0.005
0.2	12.12±0.26	0.225±0.004
0.4	11.93±0.21	0.222±0.003
0.6	11.06±0.17	0.228±0.003
0.8	10.46±0.16	0.224±0.003
1.0	9.40±0.16	0.210±0.003
1.2	7.70±0.16	0.211±0.004
1.4	6.34±0.15	0.205±0.004
1.6	5.45±0.14	0.173±0.005
1.8	3.80±0.14	0.161±0.006
2.0	2.64±0.13	0.159±0.009
2.2	1.75±0.18	
2.4	0.72±0.23	
2.6	0.29±0.26	

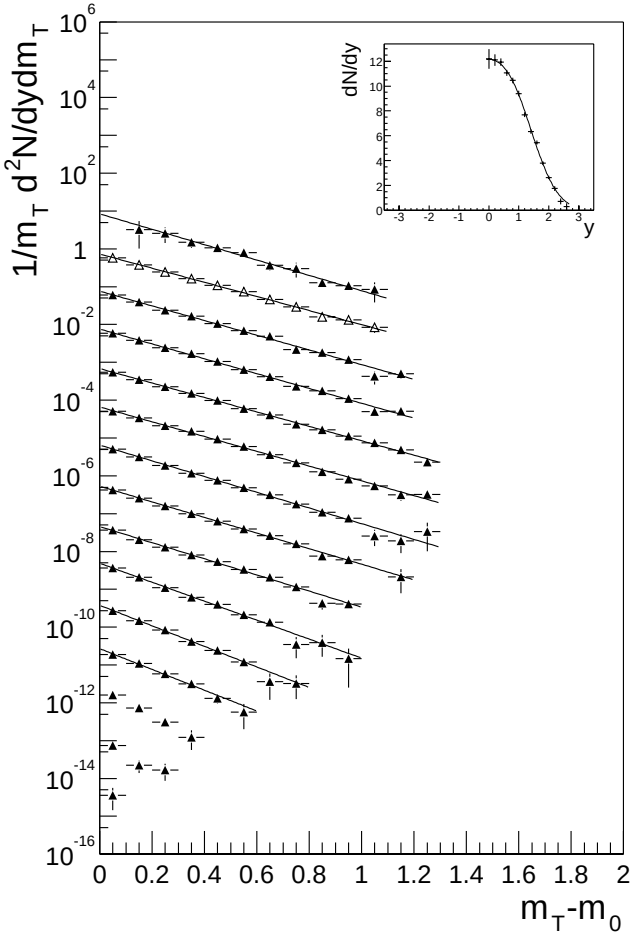

Rapidity Distributions

A	36.46±0.27
μ_y	0.71±0.01
σ_y	0.83±0.02
T_0	0.232±0.002 GeV/c
y_T	2.25±0.08

K^- Centrality Bin 3

$m_\perp$ Distributions

y	dN/dy	T (GeV/c)
-0.2		0.227±0.009
0.0	8.90±0.31	0.226±0.005
0.2	8.86±0.19	0.224±0.004
0.4	8.43±0.14	0.223±0.003
0.6	7.96±0.12	0.222±0.003
0.8	7.44±0.11	0.215±0.003
1.0	6.79±0.12	0.210±0.003
1.2	5.51±0.11	0.210±0.004
1.4	4.82±0.12	0.205±0.004
1.6	4.16±0.10	0.177±0.004
1.8	2.92±0.09	0.163±0.005
2.0	2.02±0.08	0.166±0.007
2.2	1.17±0.07	0.123±0.009
2.4	0.57±0.10	
2.6	0.28±0.07	

Rapidity Distributions

A	26.33±0.17
μ_y	0.73±0.01
σ_y	0.81±0.01
T_0	0.229±0.002 GeV/c
y_T	2.28±0.08

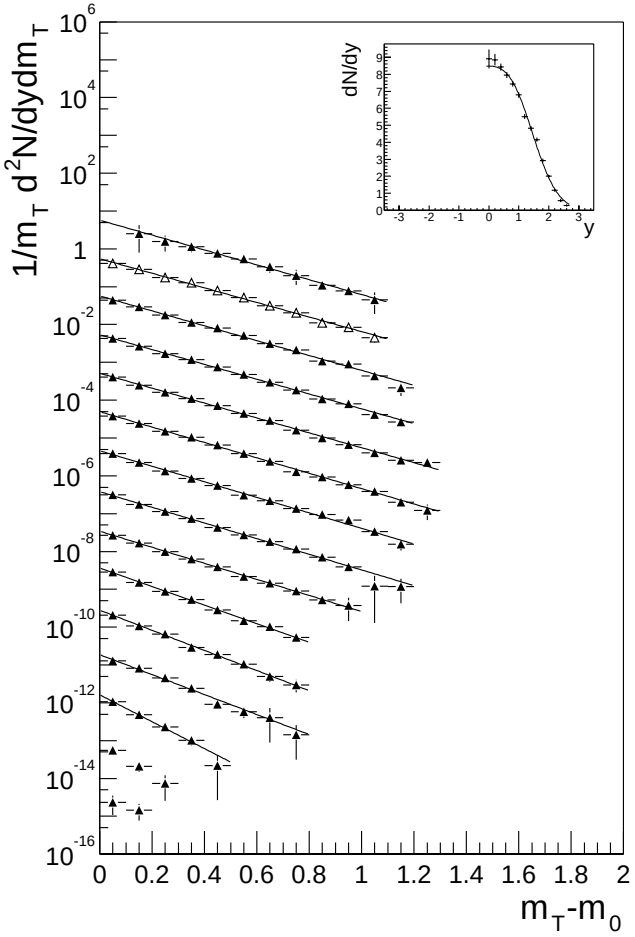

K^- Centrality Bin 4

$m_\perp$ Distributions

y	dN/dy	T (GeV/c)
-0.2		0.211±0.012
0.0	5.71±0.24	0.215±0.006
0.2	5.73±0.14	0.213±0.004
0.4	5.58±0.10	0.218±0.003
0.6	5.14±0.09	0.214±0.003
0.8	4.80±0.08	0.206±0.003
1.0	4.41±0.09	0.198±0.004
1.2	3.60±0.08	0.201±0.004
1.4	3.02±0.08	0.196±0.005
1.6	2.67±0.08	0.170±0.005
1.8	2.00±0.07	0.169±0.007
2.0	1.25±0.07	0.156±0.010
2.2	0.78±0.09	
2.4	0.53±0.10	
2.6		

Rapidity Distributions

A	17.30±0.15
μ_y	0.71±0.02
σ_y	0.87±0.02
T_0	0.218±0.002 GeV/c
y_T	2.45±0.12

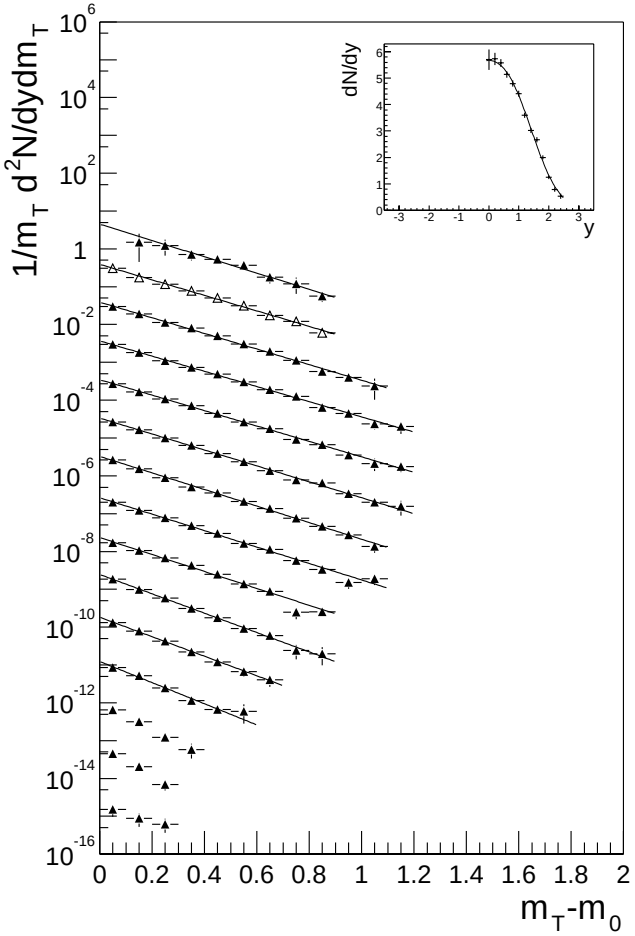

$m_\perp$ Distributions

y	dN/dy	T (GeV/c)
-0.2		0.249±0.034
0.0	3.68±0.19	0.211±0.009
0.2	3.76±0.12	0.210±0.006
0.4	3.69±0.10	0.212±0.005
0.6	3.38±0.08	0.208±0.004
0.8	3.11±0.07	0.197±0.004
1.0	2.90±0.08	0.196±0.005
1.2	2.36±0.07	0.197±0.006
1.4	2.03±0.07	0.192±0.006
1.6	1.67±0.06	0.162±0.006
1.8	1.19±0.06	0.158±0.009
2.0	0.83±0.09	0.150±0.014
2.2	0.56±0.06	
2.4	0.37±0.14	
2.6	0.43±0.14	

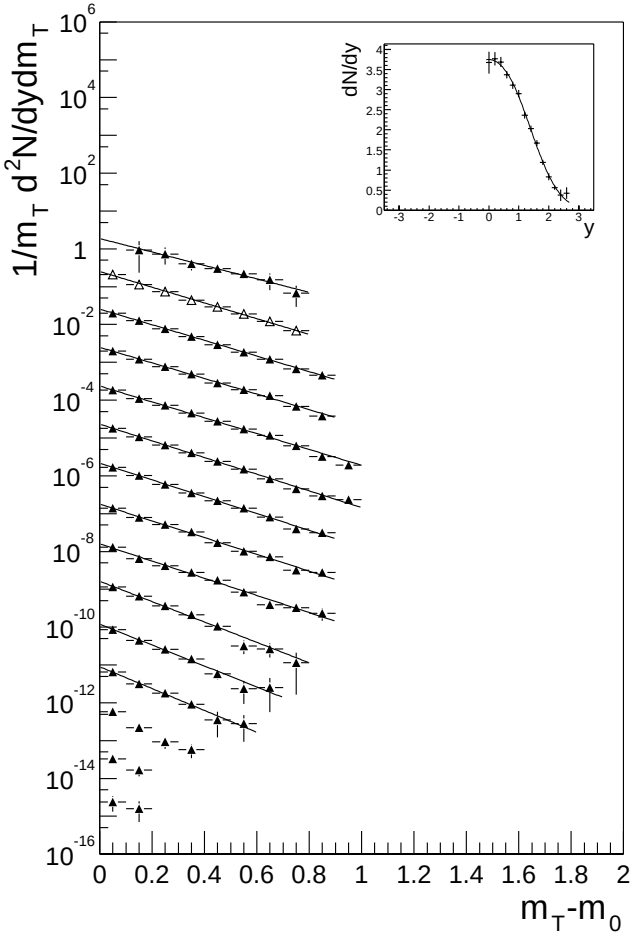

Rapidity Distributions

A	11.31±0.13
μ_y	0.70±0.03
σ_y	0.87±0.03
T_0	0.214±0.003 GeV/c
y_T	2.33±0.15

K^- Centrality Bin 6

$m_\perp$ Distributions

y	dN/dy	T (GeV/c)
-0.2		0.26±0.06
0.0	2.07±0.13	0.197±0.011
0.2	2.16±0.07	0.194±0.007
0.4	2.06±0.06	0.187±0.005
0.6	1.96±0.05	0.195±0.004
0.8	1.82±0.05	0.188±0.005
1.0	1.61±0.05	0.179±0.005
1.2	1.26±0.04	0.183±0.006
1.4	1.10±0.04	0.176±0.007
1.6	1.05±0.05	0.169±0.008
1.8	0.74±0.04	0.148±0.011
2.0	0.49±0.04	
2.2	0.26±0.06	
2.4	0.15±0.10	

Rapidity Distributions

A	6.48±0.09
μ_y	0.67±0.04
σ_y	0.91±0.05
T_0	0.195±0.003 GeV/c
y_T	2.77±0.32

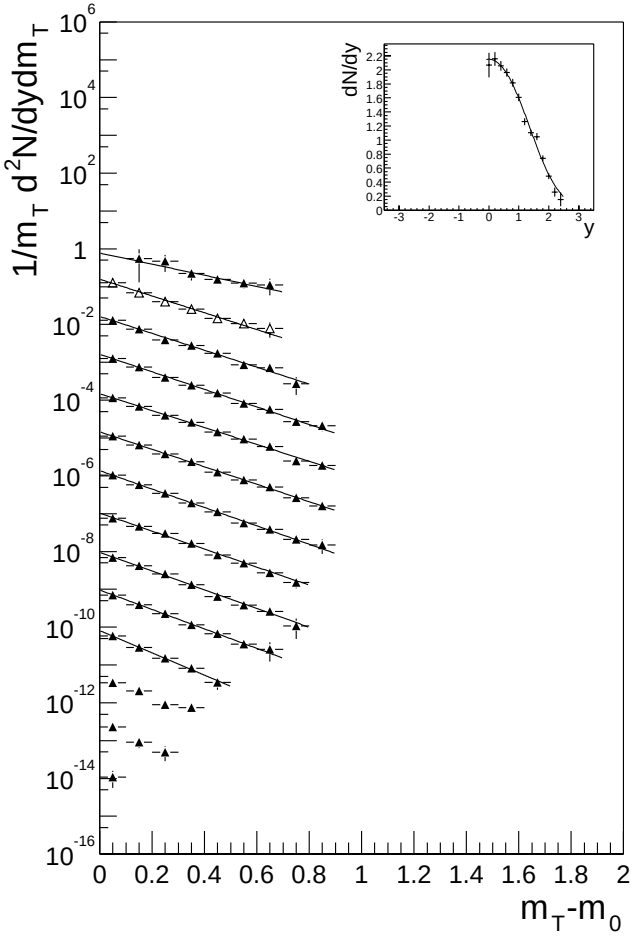

p Centrality Bin 1

$m_\perp$ Distributions

y	dN/dy	T_1 GeV/c	ξ_2	T_2 GeV/c
-0.6				
-0.4	17.1±1.3	0.33±0.04	0.03±0.02	0.047±0.028
-0.2	17.8±1.4	0.360±0.028	0.05±0.04	0.11±0.05
0.0	18.2±1.2	0.322±0.019	0.13±0.05	0.137±0.029
0.2	20.4±0.8	0.319±0.010	0.09±0.03	0.128±0.022
0.4	22.5±0.6	0.299±0.007	0.09±0.02	0.107±0.014
0.6	22.6±0.6	0.283±0.006	0.12±0.02	0.107±0.011
0.8	24.2±0.6	0.288±0.006	0.09±0.02	0.098±0.012
1.0	26.9±0.6	0.278±0.005	0.12±0.02	0.112±0.011
1.2	27.1±0.6	0.266±0.006	0.09±0.02	0.098±0.012
1.4	27.4±0.6	0.256±0.006	0.09±0.02	0.096±0.011
1.6	29.0±0.6	0.243±0.006	0.07±0.02	0.088±0.013
1.8	27.6±0.5	0.217±0.007	0.10±0.02	0.085±0.011
2.0	23.6±0.5	0.194±0.010	0.14±0.04	0.090±0.014
2.2	19.6±0.6	0.178±0.014	0.07±0.04	0.075±0.027

Rapidity Distributions

A	137.1±1.7
μ_y	1.435±0.015
σ_y	0.976±0.018
$T_{1,0}$	0.308±0.004 GeV/c
y_{T_1}	2.08±0.08
$\xi_{2,0}$	0.09±0.01
y_{ξ_2}	0±1200000
$T_{2,0}$	0.109±0.007 GeV/c
y_{T_2}	2.6±0.7

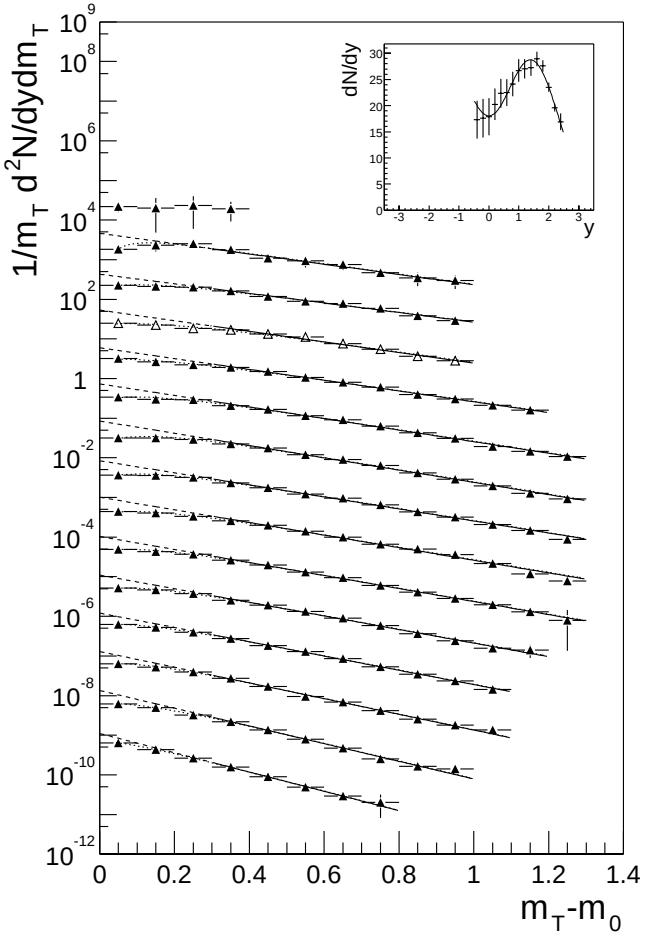

$m_\perp$ Distributions

y	dN/dy	T_1 GeV/c	ξ_2	T_2 GeV/c
-0.6				
-0.4	15.2±0.9	0.297±0.021	0.09±0.04	0.104±0.028
-0.2	15.1±0.7	0.277±0.014	0.17±0.06	0.130±0.022
0.0	14.8±0.8	0.320±0.020	0.06±0.03	0.100±0.028
0.2	16.1±0.6	0.309±0.010	0.10±0.04	0.138±0.025
0.4	17.9±0.4	0.289±0.006	0.09±0.02	0.116±0.016
0.6	18.3±0.4	0.279±0.005	0.12±0.02	0.110±0.011
0.8	19.8±0.4	0.278±0.005	0.10±0.02	0.104±0.011
1.0	21.9±0.4	0.279±0.005	0.08±0.02	0.103±0.013
1.2	22.3±0.4	0.260±0.005	0.08±0.02	0.091±0.010
1.4	23.6±0.4	0.252±0.005	0.07±0.02	0.091±0.012
1.6	24.5±0.4	0.239±0.005	0.08±0.02	0.094±0.013
1.8	24.5±0.4	0.224±0.005	0.07±0.02	0.085±0.015
2.0	21.8±0.4	0.197±0.006	0.09±0.03	0.081±0.014
2.2	19.6±0.4	0.191±0.009	0.03±0.03	0.08±0.05

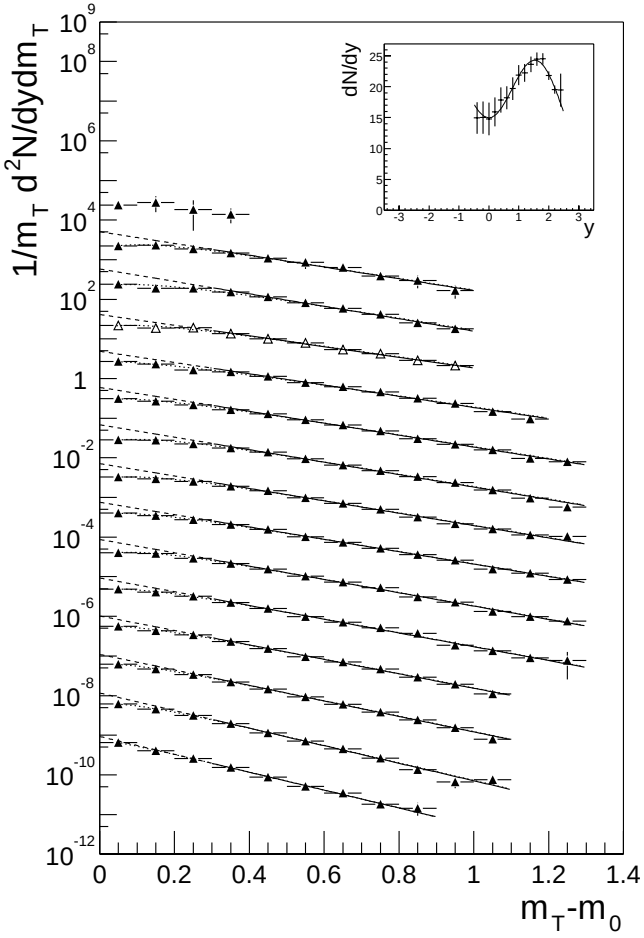

Rapidity Distributions

A	126.2±1.8
μ_y	1.581±0.020
σ_y	1.057±0.020
$T_{1,0}$	0.299±0.003 GeV/c
y_{T_1}	2.23±0.07
$\xi_{2,0}$	0.10±0.01
y_{ξ_2}	2.2±0.9
$T_{2,0}$	0.115±0.007 GeV/c
y_{T_2}	2.1±0.4

p Centrality Bin 3

$m_\perp$ Distributions

y	dN/dy	T_1 GeV/c	ξ_2	T_2 GeV/c
-0.6				
-0.4	10.7±0.5	0.284±0.020	0.05±0.03	0.072±0.026
-0.2	11.3±0.4	0.277±0.011	0.11±0.04	0.112±0.021
0.0	11.1±0.4	0.284±0.011	0.12±0.04	0.121±0.018
0.2	11.72±0.32	0.300±0.008	0.08±0.02	0.113±0.019
0.4	12.92±0.29	0.287±0.006	0.07±0.02	0.102±0.016
0.6	13.13±0.28	0.278±0.005	0.08±0.02	0.098±0.012
0.8	14.66±0.30	0.284±0.005	0.08±0.02	0.109±0.013
1.0	16.40±0.30	0.279±0.004	0.06±0.01	0.094±0.012
1.2	16.68±0.25	0.250±0.004	0.10±0.02	0.101±0.009
1.4	17.84±0.25	0.254±0.003	0.07±0.01	0.092±0.010
1.6	19.40±0.24	0.245±0.004	0.05±0.01	0.092±0.015
1.8	20.25±0.24	0.221±0.004	0.04±0.01	0.070±0.014
2.0	19.04±0.25	0.205±0.005	0.03±0.02	0.061±0.021
2.2	17.93±0.28	0.193±0.007	0.00±0.01	0.02±0.22

Rapidity Distributions

A	112.3±1.9
μ_y	1.825±0.026
σ_y	1.164±0.020
$T_{1,0}$	0.295±0.003 GeV/c
y_{T_1}	2.32±0.07
$\xi_{2,0}$	0.09±0.01
y_{ξ_2}	1.47±0.28
$T_{2,0}$	0.110±0.007 GeV/c
y_{T_2}	2.1±0.4

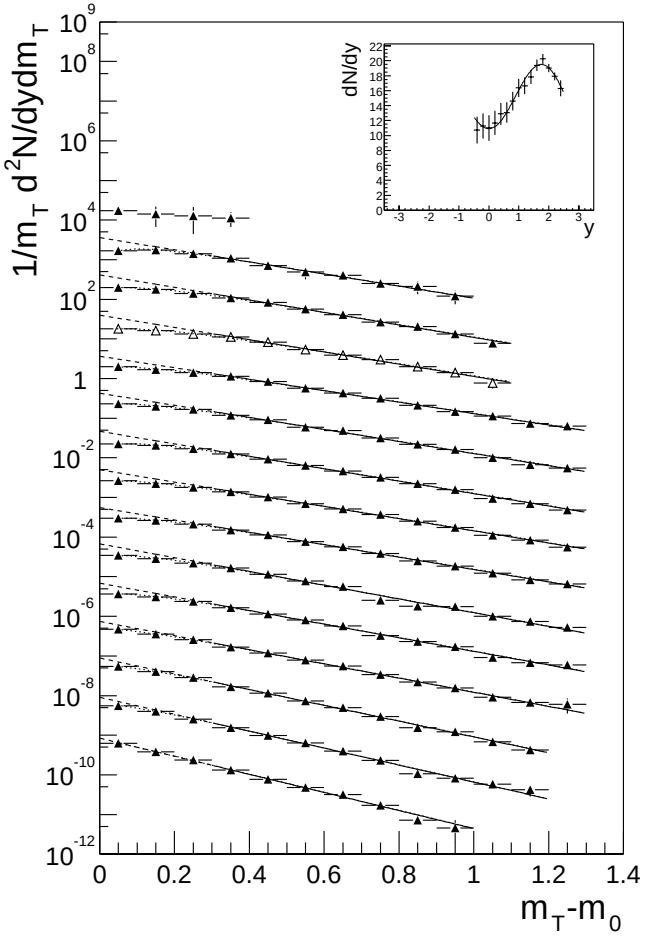

$m_\perp$ Distributions

y	dN/dy	T_1 GeV/c	ξ_2	T_2 GeV/c
-0.6				
-0.4	7.3±0.4	0.318±0.033	0.01±0.01	0.06±0.08
-0.2	7.5±0.4	0.310±0.021	0.03±0.04	0.12±0.07
0.0	7.7±0.4	0.291±0.018	0.11±0.06	0.14±0.04
0.2	7.82±0.25	0.294±0.012	0.04±0.03	0.11±0.04
0.4	8.70±0.23	0.276±0.008	0.05±0.02	0.101±0.024
0.6	9.11±0.19	0.259±0.005	0.09±0.02	0.102±0.013
0.8	10.25±0.23	0.284±0.008	0.03±0.02	0.086±0.026
1.0	11.27±0.21	0.264±0.006	0.03±0.01	0.069±0.017
1.2	12.17±0.20	0.253±0.006	0.05±0.01	0.088±0.015
1.4	13.48±0.23	0.243±0.005	0.04±0.01	0.084±0.016
1.6	14.67±0.21	0.231±0.005	0.03±0.01	0.080±0.020
1.8	15.47±0.22	0.218±0.004	0.02±0.01	0.052±0.018
2.0	15.33±0.20	0.207±0.005	0.01±0.07	0.011±0.017
2.2	15.66±0.23	0.205±0.009	0.00±0.00	0.12±0.20

Rapidity Distributions

A	98.5±2.8
μ_y	2.12±0.05
σ_y	1.264±0.029
$T_{1,0}$	0.283±0.004 GeV/c
y_{T_1}	2.44±0.09
$\xi_{2,0}$	0.04±0.01
y_{ξ_2}	-1.8±0.8
$T_{2,0}$	0.115±0.012 GeV/c
y_{T_2}	1.24±0.20

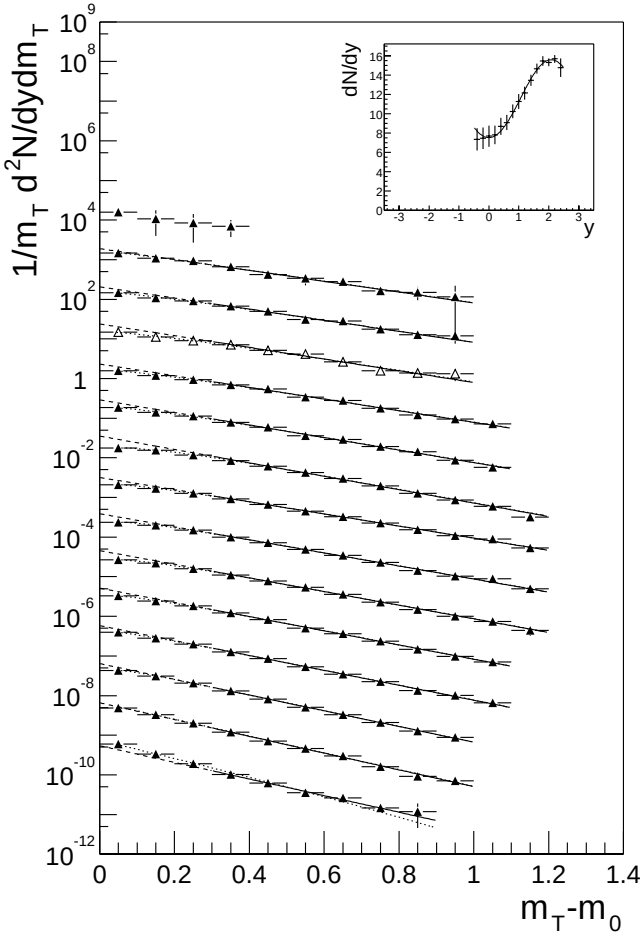

p Centrality Bin 5

$m_\perp$ Distributions

y	dN/dy	T_1 GeV/c	ξ_2	T_2 GeV/c
-0.6				
-0.4	4.4±0.4	0.28±0.06	0.04±0.03	0.07±0.04
-0.2	4.88±0.34	0.276±0.032	0.08±0.09	0.12±0.06
0.0	4.78±0.23	0.247±0.021	0.24±0.14	0.138±0.032
0.2	5.35±0.23	0.277±0.014	0.05±0.03	0.11±0.04
0.4	5.75±0.18	0.284±0.012	0.01±0.01	0.06±0.07
0.6	5.94±0.19	0.279±0.010	0.01±0.01	0.04±0.06
0.8	6.83±0.19	0.263±0.009	0.03±0.02	0.083±0.032
1.0	7.57±0.18	0.256±0.008	0.02±0.01	0.060±0.024
1.2	8.31±0.22	0.246±0.008	0.02±0.02	0.08±0.04
1.4	9.25±0.22	0.238±0.007	0.02±0.01	0.056±0.025
1.6	10.65±0.20	0.221±0.006	0.01±0.01	0.049±0.030
1.8	11.95±0.23	0.208±0.006	0.02±0.01	0.055±0.020
2.0	11.96±0.19	0.189±0.006	0.02±0.01	0.063±0.027
2.2	12.53±0.16	0.181±0.008	0.00±0.04	0.12±0.20

Rapidity Distributions

A	87±4
μ_y	2.46±0.08
σ_y	1.36±0.04
$T_{1,0}$	0.284±0.005 GeV/c
y_{T_1}	2.14±0.09
$\xi_{2,0}$	0.02±0.00
y_{ξ_2}	0±500000
$T_{2,0}$	0.097±0.018 GeV/c
y_{T_2}	-1.4±0.5

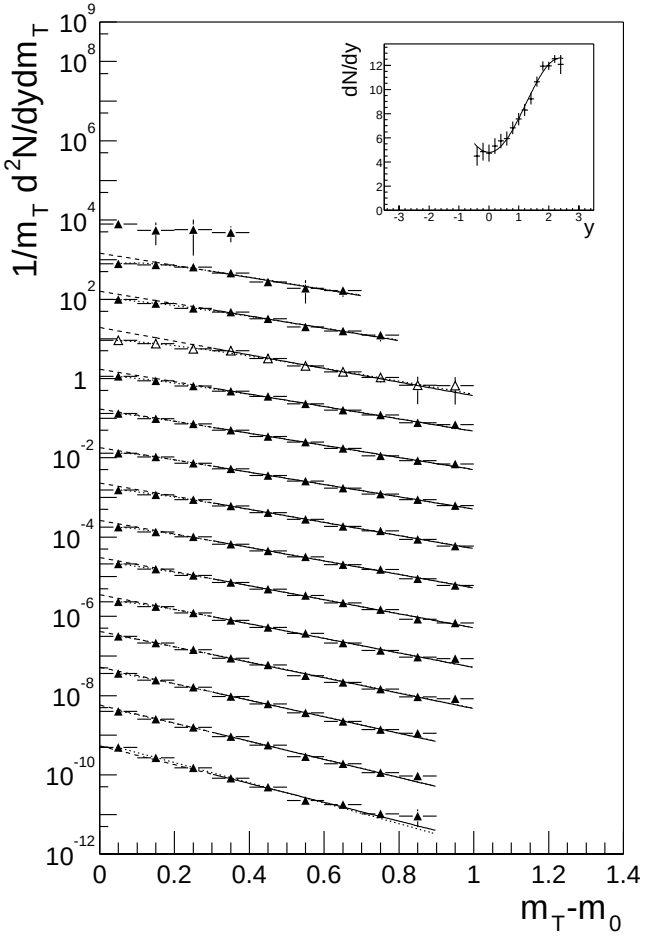

$m_\perp$ Distributions

y	dN/dy	T_1 GeV/c	ξ_2	T_2 GeV/c
-0.6				
-0.4	2.77±0.31	0.20±0.06		
-0.2	2.63±0.20	0.22±0.05		
0.0	2.71±0.18	0.24±0.04	0.05±0.06	0.09±0.06
0.2	3.05±0.17	0.257±0.022	0.03±0.07	0.10±0.11
0.4	3.43±0.14	0.282±0.019	0.00±0.01	0.11±0.21
0.6	3.53±0.12	0.264±0.015	0.00±0.07	0.01±0.16
0.8	3.92±0.12	0.259±0.013	0.01±0.17	0.01±0.05
1.0	4.54±0.15	0.244±0.011	0.01±0.01	0.03±0.06
1.2	5.07±0.15	0.235±0.010	0.01±0.02	0.06±0.05
1.4	5.62±0.15	0.240±0.010	0.00±0.01	0.11±0.21
1.6	6.94±0.14	0.215±0.007	0.01±0.09	0.012±0.031
1.8	8.14±0.13	0.200±0.006	0.01±0.10	0.012±0.028
2.0	8.87±0.14	0.178±0.006	0.01±0.11	0.01±0.04
2.2	9.64±0.12	0.166±0.008	0.00±0.06	0.12±0.20

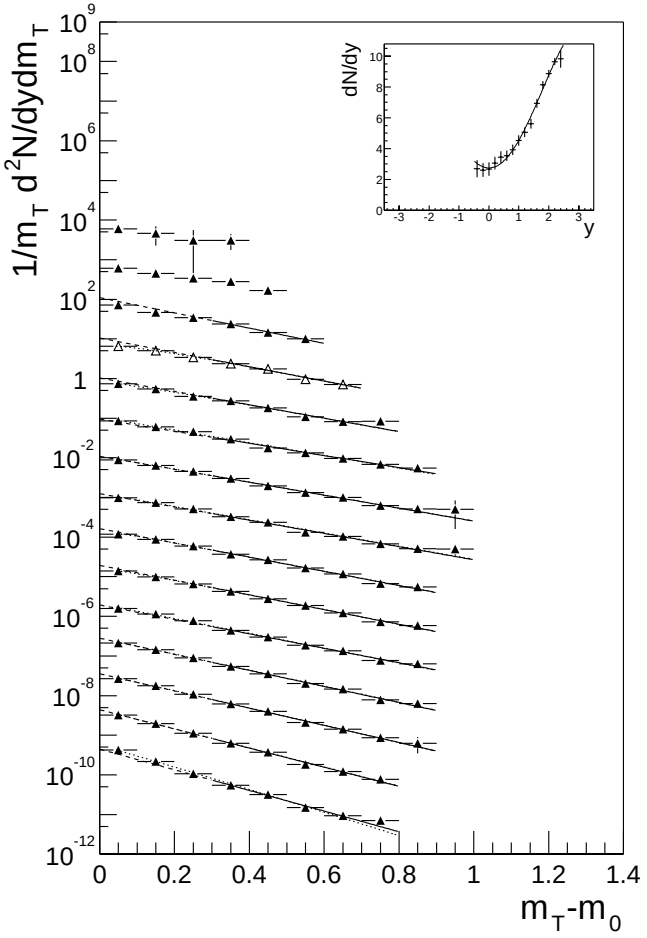

Rapidity Distributions

A	105±13
μ_y	3.43±0.21
σ_y	1.64±0.08
$T_{1,0}$	0.277±0.007 GeV/c
y_{T_1}	2.06±0.10
$\xi_{2,0}$	0.05±0.06
y_{ξ_2}	0.0±0.7
$T_{2,0}$	0.12±0.04 GeV/c
y_{T_2}	0.12±0.04

$\overline{\mathrm{p}}$ Centrality Bin 1

$m_\perp$ Distributions

y	dN/dy	T (GeV/c)
-0.2		
0.0		
0.2	0.83±0.14	0.42±0.10
0.4	1.11±0.13	0.33±0.04
0.6	1.17±0.12	0.324±0.031
0.8	1.03±0.11	0.36±0.04
1.0	1.21±0.15	0.41±0.07
1.2	1.09±0.11	0.297±0.035
1.4	0.96±0.09	0.29±0.04
1.6	0.83±0.07	0.240±0.031
1.8	0.77±0.08	0.26±0.04
2.0	0.53±0.06	
2.2	0.36±0.05	

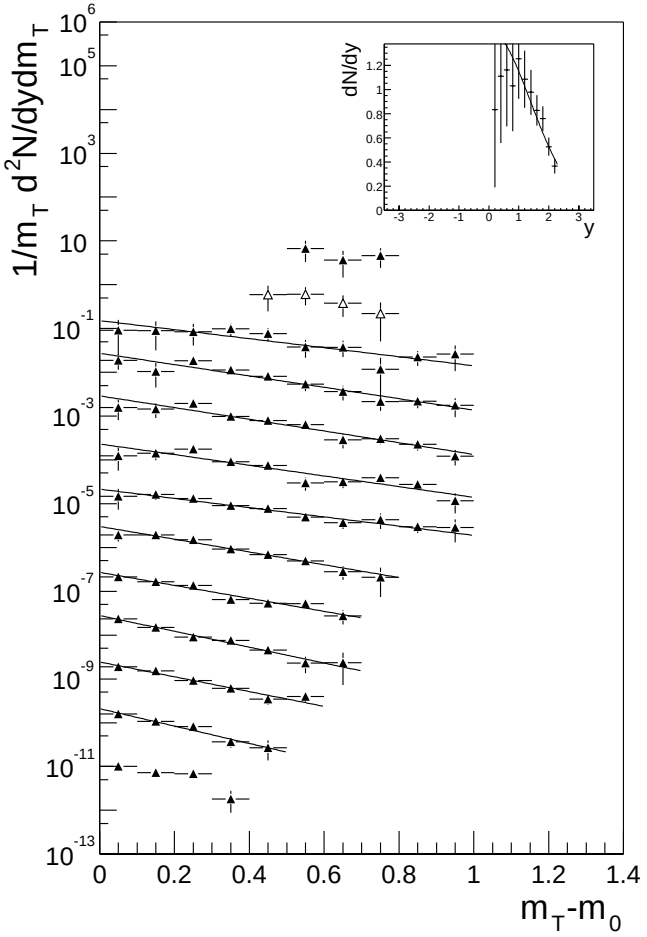

Rapidity Distributions

A	4.90±0.18
σ_y	1.60±0.08
T_0	0.360±0.025 GeV/c
y_T	1.9±0.4

$m_\perp$ Distributions

y	dN/dy	T (GeV/c)
-0.2	0.86±0.18	0.55±0.24
0.0	0.66±0.13	0.41±0.14
0.2	0.75±0.10	0.36±0.05
0.4	0.91±0.08	0.291±0.029
0.6	0.85±0.08	0.300±0.028
0.8	0.85±0.08	0.304±0.029
1.0	0.85±0.07	0.294±0.030
1.2	0.86±0.07	0.286±0.026
1.4	0.69±0.06	0.273±0.032
1.6	0.48±0.05	0.24±0.04
1.8	0.45±0.05	0.24±0.04
2.0	0.44±0.04	0.180±0.021
2.2	0.315±0.034	0.20±0.04

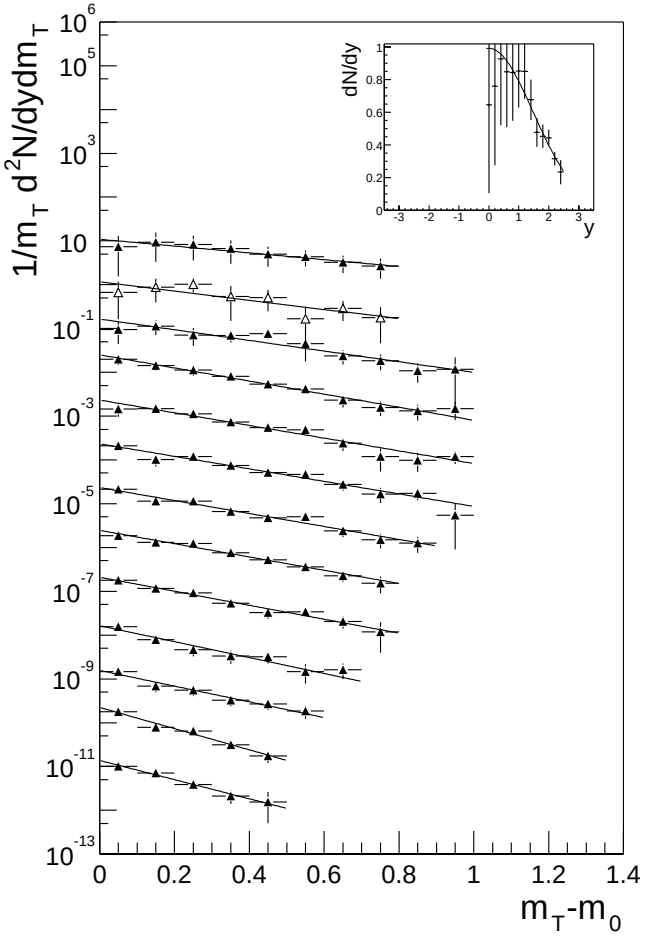

Rapidity Distributions

A	3.62±0.11
σ_y	1.55±0.06
T_0	0.328±0.017 GeV/c
y_T	1.88±0.22

$\overline{\mathrm{p}}$ Centrality Bin 3

$m_\perp$ Distributions

y	dN/dy	T (GeV/c)
-0.2	0.60±0.11	0.48±0.14
0.0	0.62±0.11	0.51±0.14
0.2	0.71±0.08	0.41±0.05
0.4	0.81±0.07	0.362±0.030
0.6	0.78±0.06	0.314±0.022
0.8	0.67±0.05	0.308±0.024
1.0	0.64±0.05	0.311±0.026
1.2	0.57±0.05	0.265±0.026
1.4	0.48±0.04	0.231±0.025
1.6	0.438±0.035	0.244±0.027
1.8	0.349±0.029	0.186±0.022
2.0	0.353±0.027	
2.2	0.236±0.034	

Rapidity Distributions

A	2.88±0.08
σ_y	1.52±0.06
T_0	0.369±0.018 GeV/c
y_T	1.42±0.14

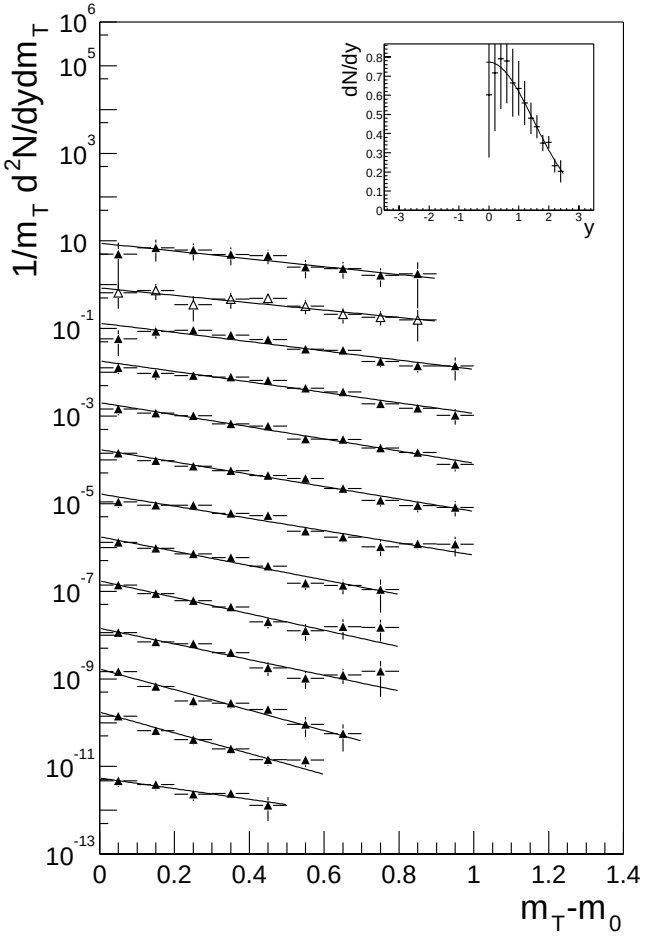

$\overline{\mathrm{p}}$ Centrality Bin 4

$m_\perp$ Distributions

y	dN/dy	T (GeV/c)
-0.2		0.9±0.8
0.0	0.37±0.07	0.44±0.15
0.2	0.43±0.06	0.32±0.05
0.4	0.55±0.05	0.317±0.033
0.6	0.54±0.04	0.285±0.024
0.8	0.45±0.04	0.284±0.029
1.0	0.42±0.04	0.31±0.04
1.2	0.430±0.034	0.260±0.027
1.4	0.358±0.029	0.217±0.025
1.6	0.309±0.026	
1.8	0.231±0.021	0.158±0.021
2.0	0.208±0.022	
2.2	0.168±0.019	0.19±0.05

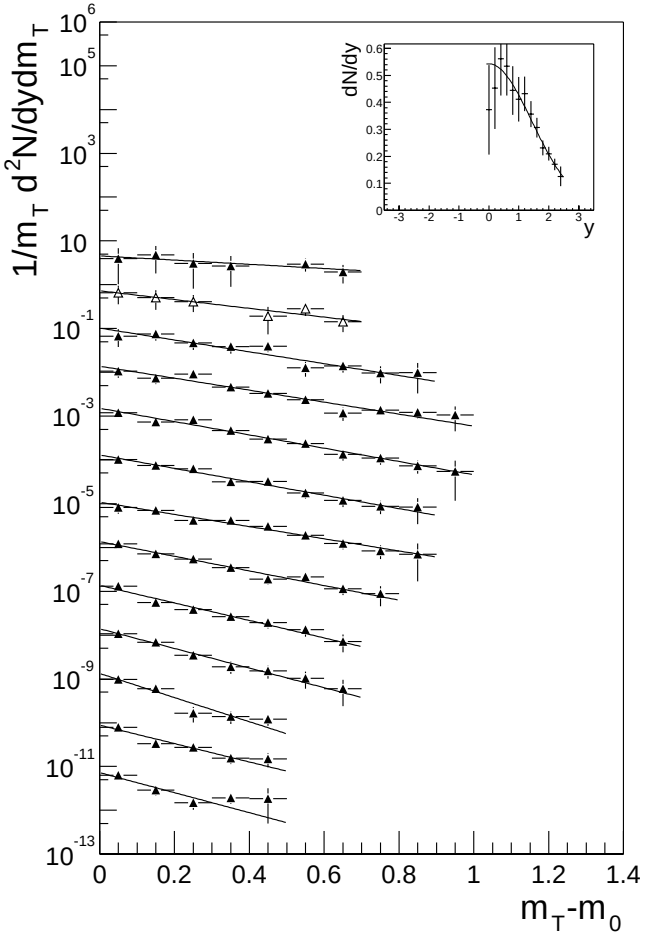

Rapidity Distributions

A	1.95±0.06
σ_y	1.47±0.06
T_0	0.329±0.019 GeV/c
y_T	1.47±0.17

$\overline{\mathrm{p}}$ Centrality Bin 5

$m_\perp$ Distributions

y	dN/dy	T (GeV/c)
-0.2		0.6±0.6
0.0	0.50±0.15	0.45±0.25
0.2	0.37±0.07	0.42±0.11
0.4	0.34±0.04	0.28±0.04
0.6	0.35±0.04	0.29±0.04
0.8	0.31±0.06	0.49±0.20
1.0	0.31±0.05	0.43±0.13
1.2	0.281±0.034	0.28±0.05
1.4	0.226±0.032	0.29±0.08
1.6	0.170±0.026	
1.8	0.159±0.028	
2.0	0.173±0.026	
2.2	0.120±0.021	

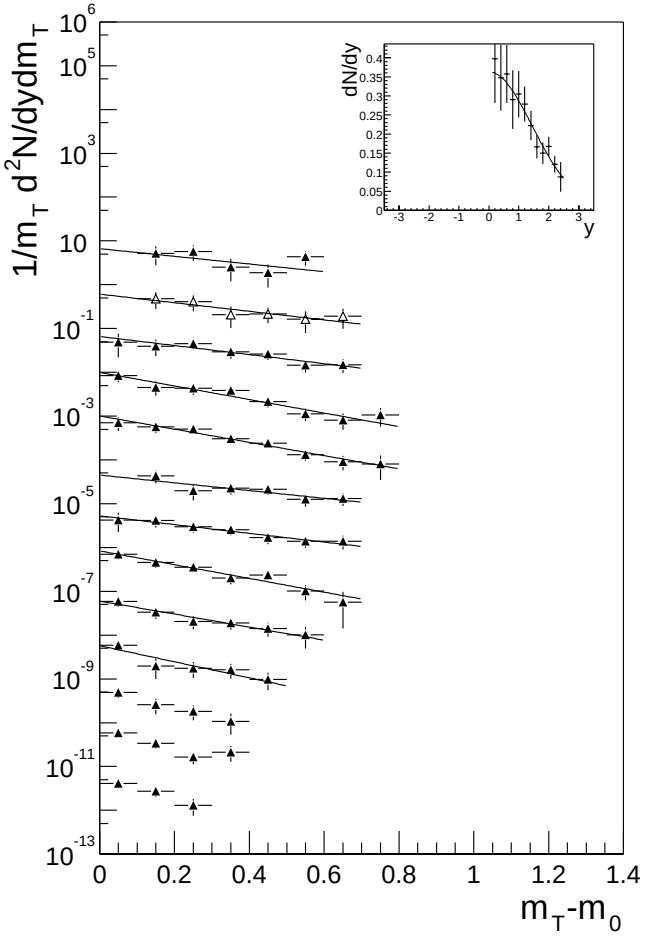

Rapidity Distributions

A	1.35±0.06
σ_y	1.44±0.09
T_0	0.302±0.033 GeV/c
y_T	4.3±0.9

$m_\perp$ Distributions

y	dN/dy	T (GeV/c)
-0.2	0.34±0.11	
0.0	0.29±0.08	
0.2	0.21±0.04	0.33±0.08
0.4	0.23±0.04	0.33±0.06
0.6	0.243±0.029	0.28±0.04
0.8	0.203±0.028	0.35±0.08
1.0	0.166±0.025	0.26±0.05
1.2	0.163±0.023	0.29±0.06
1.4	0.167±0.032	0.36±0.15
1.6	0.122±0.021	
1.8	0.115±0.018	
2.0	0.089±0.027	
2.2	0.059±0.022	

Rapidity Distributions

A	0.84±0.05
σ_y	1.40±0.10
T_0	0.31±0.04 GeV/c
y_T	2.8±0.6